Title
An Associated Particle Imaging System for the Determination of 3D Isotopic Distributions

Author
Ayllon Unzueta, Mauricio

Publication Date
2020

Peer reviewed|Thesis/dissertation

An Associated Particle Imaging System for the Determination of 3D Isotopic Distributions

by

Mauricio Ayllon Unzueta

A dissertation submitted in partial satisfaction of the

requirements for the degree of

Doctor of Philosophy

in

Engineering - Nuclear Engineering

in the

Graduate Division

of the

University of California, Berkeley

Committee in charge:

Professor Karl van Bibber, Chair
Professor Lee Bernstein
Professor Paul Renne

Spring 2020

An Associated Particle Imaging System
for the Determination of 3D Isotopic Distributions

Abstract

An Associated Particle Imaging System
for the Determination of 3D Isotopic Distributions

by

Mauricio Ayllon Unzueta

Doctor of Philosophy in Engineering - Nuclear Engineering

University of California, Berkeley

Professor Karl van Bibber, Chair

Associated Particle Imaging (API) is a nuclear technique that allows for the non-destructive determination of 3D isotopic distributions. The technique is based on the detection of the alpha particle associated with the neutron emitted in the deuterium-tritium (DT) fusion reaction, which provides information regarding the direction and time of emission of the 14 MeV neutron. Inelastic neutron scattering leads to characteristic gamma-ray emission from certain isotopes, which can be correlated with the neutron interaction location. An API system consisting of a sealed-type neutron generator, gamma detectors, and a position-sensitive alpha detector was designed, constructed, and tested at Lawrence Berkeley National Laboratory (LBNL) for the non-destructive quantification of ^{12}C distribution in soils. Additionally, the system is also sensitive to other elements present in the soil such as O, Si, Al, Fe, etc. It is capable of quantifying ^{12}C at the percent level with a resolution of 2 cm $\times$ 2 cm $\times$ 7 cm for an hour of measurement. The first half of the dissertation describes the design of the system (using the simulation packages MCNP6, SPICE, and COMSOL Multiphysics) and the characterization of its components including the neutron generator, the position-sensitive alpha detector (YAP), the lanthanum bromide (LaBr) and sodium iodide (NaI) gamma detectors, and the systems used to observe the alpha and gamma signal. The second half focuses on data analysis techniques and presents initial experimental data benchmarked against simulations.

To my family in Bolivia.

Nada de esto sería posible sin su amor, apoyo y dedicación.

Contents

List of Figures

List of Tables

Acknowledgments

First and foremost I would like to thank Dr. Arun Persaud from Lawrence Berkeley National Laboratory for going far beyond his role as a supervisor and becoming a mentor and role model to me. His patience, work ethics, and deep knowledge of the subject have given me a reference to strive for as a scientist and as a person. Most of the work presented in this thesis is the result of lengthy discussions and collaborative work with him. Arun is extremely approachable and a real pleasure to work with. Additionally, I would like to thank Dr. Bernhard Ludewigt who was indispensable for the success of this project and from whom I accentuated my knowledge on neutron generators and nuclear physics. Both Bernhard and Arun have drastically changed how I approach and solve scientific problems.

I would also like to thank Professor Karl van Bibber who gave me the opportunity to join his group at UC Berkeley and served as my advisor in every sense of the word; from academic development to personal growth. His constant positive attitude and friendly demeanor created an enjoyable and productive working environment. Additionally, I want to thank Professor Lee Bernstein who is the most passionate physicist I have had the honor to work with. His enthusiasm and insight made this work and my time in Berkeley more enjoyable. I am also grateful to Professor Paul Renne who trusted me with carrying forward part of his project on geochronology and offered support throughout my first two years.

I am also thankful to Dr. Thomas Schenkel with whom I initially discussed options to start working at LBNL, to Dr. Ka-Ngo Leung for interesting discussions about novel ideas in the field, Tim Becker and Takeshi Katayanagi for essential technical and mechanical support, and Cory Waltz for selflessly sharing much of his knowledge on neutron generators.

I could not have completed this dissertation and at the same time enjoyed my time in Berkeley without great friends such as Maria Simanovskaia, Sandra Bogetic, Laura Geulig, Justin Ellin, Emily Frame, Jose Marcial Contreras, Elizabeth Contreras, and Mario Ortega. They made this journey worth it. I am very grateful to Karen Bascon for being with me during the best and worst times of my PhD offering essential emotional support.

Finally, this work could not have been possible without the constant support of my brothers, Sergio and Samuel Ayllon who always encouraged me to move forward and pursue my dreams, and my parents Victor Hugo Ayllon and Myriam Unzueta who could not have done a better job guiding me in life. I am extremely grateful to have them with me in every step along the way.

Chapter 1

Introduction

Associated Particle Imaging (API) is a non-destructive technique that allows for determining the 3D location of certain isotopes in a given sample. The system described in this thesis consists of a sealed-type neutron generator, an alpha particle detector, and two gamma-ray detectors, i.e. lanthanum bromide ($LaBr_3$) and sodium iodide (NaI). The neutron generator works by accelerating a mixture of deuterium (D) and tritium (T) ions towards a titanium target where they accumulate forming a so called "self-loaded target". Subsequent ions can induce DT fusion reactions within a small well-defined surface of approximately 2 mm in diameter.

$$D + T \rightarrow \alpha\ (3.5\,\mathrm{MeV}) + n\ (14.1\,\mathrm{MeV}) \qquad 99.96\% \tag{1.1}$$

The nuclear reaction shown in Equation 1.1 results in a two-particle decay, and hence the products are emitted back-to-back in the center-of-mass reference frame. The detection of the alpha particle in a position-sensitive detector provides information about the direction and time the neutron was emitted. This high-energy neutron can leave the vacuum chamber and interact with a nucleus in the interrogated sample by non-elastic scattering, which can leave the resulting nucleus in an excited state. The de-excitation, which typically happens in 10^{-8} - 10^{-12} s is accompanied by the emission of one or more gamma rays with energies unique to the isotope. The gamma ray can then be detected with a fast scintillator and its time and energy recorded. Based on that time difference, the depth of interaction Z can be calculated allowing for a 3D density profile of the object to be reconstructed by measuring many of these events. This process is exemplified in Figure 1.1, which shows a particular case where the inelastic scattering in a ^{12}C nucleus leads to the production of a gamma ray.

^{12}C is well-suited for this technique because of its relatively high inelastic scattering cross-section of approximately 187 ± 7.5 mb averaged over all incident angles [25] at 14.1 MeV and because it emits (for all practical purposes) a single gamma ray of 4.4 MeV from its first excited state to the ground state. Additionally, this high-energy gamma ray is not easily attenuated by low and medium density objects, which allows for interrogation of deeper layers.

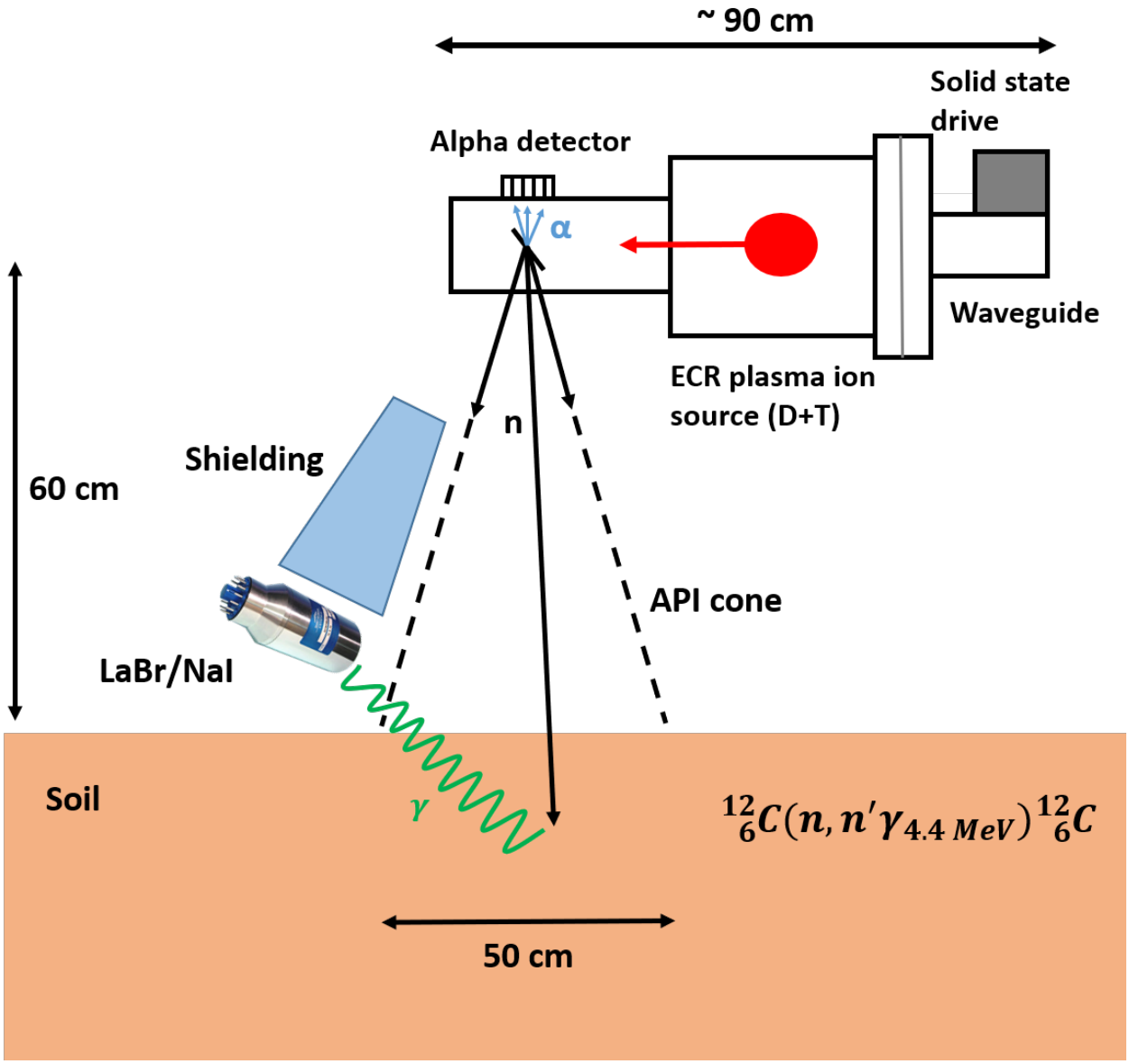

Figure 1.1: Schematic illustration of the API technique. A 14.1 MeV neutron and an alpha particle are created back-to-back in a known volume. The neutron undergoes inelastic scattering off an isotope in the target, for example a ^{12}C nucleus, which emits a 4.4 MeV gamma ray. The location of interaction can be determined in 3D from the time difference between the detection of the alpha particle and the gamma ray and from the X-Y measurement of the position of the alpha particle in the detector.

The neutron generator used in this project is designed and built by Adelphi Inc. [1] while the alpha detector system was designed internally and it is discussed in detail in Chapter 2. Figure 1.2 shows some of its most relevant components together with a schematic of how it works. A future iteration of the API neutron generator design will be discussed in Chapter 6.

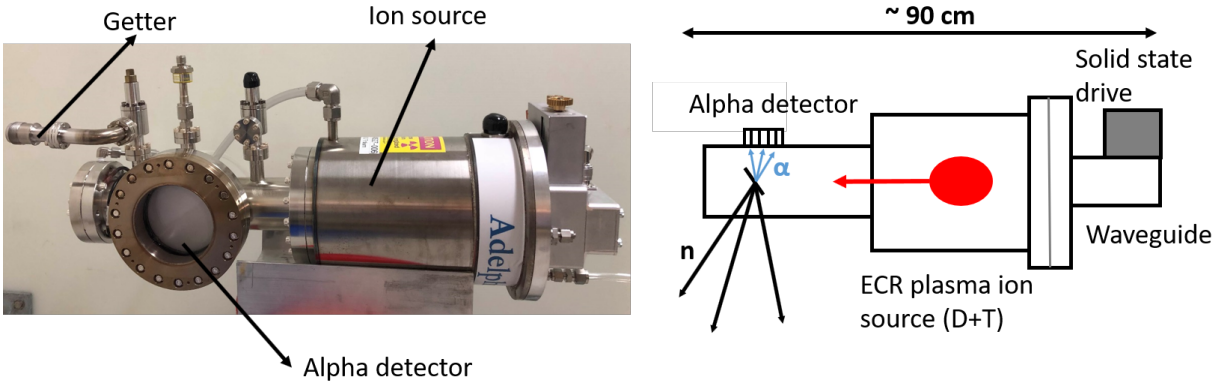

Figure 1.2: Sealed-type API neutron generator used for this project together with a simplified representation of how it works. The getter is heated during operation, which releases trapped deuterium and tritium into the vacuum chamber. The same gas mixture is therefore also present in the ion source where a plasma is ignited with a microwave generator. These ions are then accelerated through the drift region onto an angled target where the DT fusion reaction can take place.

1.1 Origins of the API Technique and Applications

The origins of API can be traced back to the 50's and 60's when the associated particle method (APM) was introduced with the main objective of reducing the induced gamma background (e.g. [36]) by recording gamma rays in coincidence with the associated particle in a DD or DT fusion reaction, i.e. ^{3}He and ^{4}He, respectively. Additionally, APM allowed for the possibility to measure the absolute neutron output (n/s) directly in a neutron generator by counting the associated alpha particles and taking into account the solid angle subtended by the alpha detector with respect to the neutron beam spot (see for example [13] and [60]). Fast scintillators, fast electronics, and high-resolution position-sensitive photomultiplier tubes have recently allowed for both nanosecond and sub-nanosecond time resolution and sub-millimeter position resolution. This combination allows for the possibility of imaging objects of several centimeters. An early proof-of-principle paper about API presented in [7] obtained 2D projections for different materials (water and table salt), hence showing some of the most important capabilities of this technique. Since then, API has found many uses in different areas of research and industry including detection of illicit drugs [17], explosives [8],

special nuclear material (SNM) [22], and diamonds [16] among many other applications. Recently, there has been interest in using API for applications in space exploration, such as in [30], where API is considered as an instrument to be mounted on planetary rovers or landers in order to analyze the elemental composition of the surface. In that particular application, API greatly reduces the gamma background from rover/lander structural materials and cosmic radiation.

At Lawrence Berkeley National Laboratory (LBNL), we have developed an API instrument for quantifying carbon distribution in soil. Non-destructive carbon-in-soil measurement methods are important for understanding and quantifying soil-based carbon sequestration techniques on a large scale since soil is the largest storage pool of terrestrial carbon [43]. Monitoring carbon in soil also supports improvements in soil health and crop yield [21]. The standard procedure to measure carbon concentration in soils today consists of taking core (point) samples and analyzing them in a chemistry lab using loss on ignition (LOI) techniques [53]. This destructive procedure takes from a few days to weeks before results are obtained, and the results are usually extrapolated to the entire field. The API instrument described in this thesis would be able to non-destructively analyze larger samples (50 $\times$ 50 $\times$ 30 cm^3) in a few minutes (for a commercial system) depending on carbon concentration. Additionally, it may provide information regarding other main constituent elements and the average bulk density.

1.2 Theoretical Considerations

Important Neutron Interactions with Matter for API

Neutrons can interact with matter in different ways. As opposed to gamma rays or charged particles, neutrons interact mostly with atomic nuclei and rarely with electrons because of their charge neutrality. The specific type of neutron-nucleus interaction depends strongly on the energy of the incident neutron as well as the internal structure of the target (^{A}X) or compound ($^{A+1}$X) nucleus. Nuclei have excited states or energy levels, which are somewhat analogous to the excited states in atoms. In the simplistic single-particle model, these energy levels can be populated by the excitation of one or more nucleons upon energy transfer from an interaction. The level scheme depicting these states in ^{12}C is shown in Figure 1.3. This is an example of a low-mass nucleus and hence the energy levels are separated by wider energy gaps compared to heavier nuclei, which in general have a greater density of states. Special exceptions are observed in magic nuclei that have particularly stable configurations and their energy levels resemble those of lower mass nuclei. Each of these energy levels have a characteristic energy width (Γ), which determine the lifetime of such a state. For instance, the measured energy width of the 4.4 MeV level in ^{12}C is approximately 0.01 eV [27]. Hence, the mean lifetime (τ) is as follows

$$\tau = \hbar/\Gamma = 66\,\mathrm{fs} \tag{1.2}$$

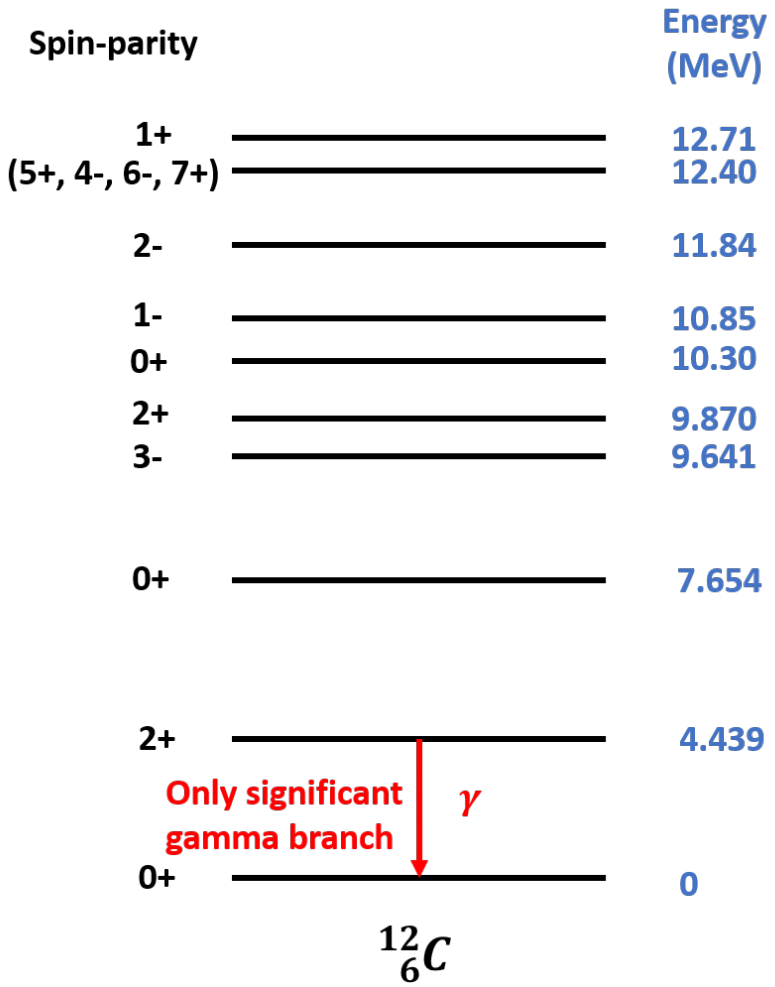

Figure 1.3: ^{12}C decay scheme showing excited states in the nucleus that can be populated by a 14.1 MeV neutron [3]. Note that the highest possible excitation energy that can be left in the nucleus is approximately 13 MeV due to recoil. Only the 4.4 MeV state has a significant gamma branch. The only other gamma-ray source on carbon would be from ^{13}C, but its natural isotopic abundance is only 1.1 %.

The implications to our API system of such a short mean lifetime is that its effects on the time-of-flight resolution and peak broadening in the energy spectrum due to the uncertainty principle are negligible. Other effects, however, such as Doppler broadening will have a significant effect on the energy resolution. This concept will be revisited in Chapter 3.

A neutron can interact with the nucleus and leave it unchanged either in its isotopic composition or internal energy, i.e. in its ground state, in a process known as elastic scattering. This process can be largely modeled with classical mechanics and is the most important moderation mechanism at medium to low neutron energies. If the incoming neutron leaves the nucleus in an excited state without changing its isotopic composition, the process is known as inelastic scattering and it usually takes place at higher neutron energies. This process is a threshold reaction, which means that it cannot take place at neutron energies below the first excited state of the nucleus. Therefore, neutron energies higher than 4.4 MeV are required in our API application. In fact, the energy threshold is slightly higher because of the kinetic recoil energy of the target nucleus. Therefore, the actual energy threshold (E_{th}) for such a reaction is given by Equation 1.3.

$$E_{th} = \frac{A+1}{A} E_1 = \frac{13}{12}(4.4\,\text{MeV}) = 4.8\,\text{MeV} \tag{1.3}$$

where A is the mass number of the target nucleus and E_1 is the energy of the first excited state. This energy threshold is why a DT neutron generator is used, which emits 14.1 MeV neutrons as opposed to a DD neutron generator (2.5 MeV neutrons). Further discussion about inelastic scattering and its role in slowing down high-energy neutrons are presented in [29] and Chapter 4 when discussing shielding structures. A neutron can also undergo capture, which changes the isotopic composition of the target nucleus and brings additional binding energy into the nucleus. Therefore, it can leave the nucleus in an excited state which usually decays by β^- accompanied by the emission of one or several gamma rays that are specific to the daughter isotope. This is the main idea behind neutron activation analysis (NAA) for isotopic determination of unknown samples. Neutron capture generally happens after the neutrons have been slowed down to thermal energies, which requires longer periods of time greater than our API time windows of a few tens of nanoseconds, and therefore, are not part of the API spectrum. Additionally, position information is lost because multiple scattering events are necessary to reach thermal energies. However, information from neutron capture gamma rays can be valuable for determining average water content since ^{1}H emits 2.2 MeV gamma rays upon a single neutron capture. This process is negligible for the case of ^{12}C, which has a very low neutron capture cross-section. There are other processes that can take place upon neutron interactions with nuclei such as nuclear fission, charged particle emission, or spallation. However, they are not specifically relevant for this application and therefore will not be discussed further.

Cross-sections and Reaction Rates

The probability of each of the previously explained reactions to occur is described by the cross-section, and it is better understood within the concept of reaction rates (R) as shown in Equation 1.4

$$R(E,\vec{r}) = N_t \iint \sigma(E)\ \phi(E,\vec{r})\ dE\, d\vec{r} \tag{1.4}$$

where R is the reaction rate in γ/s as a function of energy E and position $\vec{r}$, N_t is the total number of target nuclei, σ is the microscopic cross-section for the emission of that particular gamma ray (including branching ratios), and ϕ is the neutron flux. The integration takes place over all energies and positions. Note that this simple equation can help us predict the gamma ray expected from reactions in different isotopes in back-of-the-envelope calculations. However, codes like MCNP6 [18] employ a more rigorous and complete treatment. The main message to be taken from this equation is that the reaction rate is directly proportional to the number of target nuclei N_t, and we can directly measure $R(E,\vec{r})$ as the area under the peak in the gamma spectrum (taking into account detector efficiency factors). Additionally, we can measure $\phi(E,\vec{r})$ or its time-integrated quantity (fluence) by counting alpha particles accounting for the solid angle subtended by the detector. Cross-sectional data, easily accessible from large databases such as ENDF [3], allows for a forward analysis in extracting the absolute abundance of elements. However, certain complications arise due to the flux variability in deeper soil layers as a function of water content. Some analysis considerations are touched upon in Chapter 5.

Properties of Deuterium-Tritium (DT) Fusion

DT fusion is an exothermic reaction that can be induced at low incident energies making it an ideal reaction for low-power compact neutron generators. The reaction occurs below the Coulomb energy barrier due to quantum tunneling between the deuteron and triton. The Coulomb energy barrier is shown in Equation 1.5 where the deuteron and triton are separated by approximately 5 fm of their nuclear radii.

$$E_{DT} = \frac{e^2}{4\pi\epsilon_o}\frac{Z_D Z_T}{R_D + 5\,\mathrm{fm} + R_T} = 170\,\mathrm{keV} \tag{1.5}$$

The cross-section for this reaction ($\approx$ 5 b) is more than 100 times that of DD and TT fusion at 100 kV [52] due to a strong resonance in the ^{5}He compound system that peaks around 107 keV. At these low energies, the only significant reaction channel is the immediate disintegration of the compound nucleus ^{5}He into a neutron and an alpha particle, as shown in Equation 1.1. While there is a small ($\approx$ 0.04%) branch to the emission of a 17 MeV photon and the production of a neutron and alpha-particle at rest, the vast majority of the decay of the ^{5}He compound system occurs through the emission of a 14.1 MeV neutron and a 3.54 MeV alpha particle. In the center of mass system, these particles are emitted at 180

Variable	Description
θ_b	lab scattering angle
θ'_b	CM scattering angle
T	lab kinetic energy
v	particle velocity
Q	Q-value of reaction
m	particle mass

Table 1.1: Parameter notation for Equations 1.6 and 1.7.

degrees from each other. However, in the laboratory system they are emitted at an angle given by Equation 1.6. Each of the terms of this equation are explained in Table 1.1.

$$\tan\theta_b = \frac{\sin\theta'_b}{\cos\theta'_b + \gamma} \tag{1.6}$$

where γ is given by:

$$\gamma = \frac{v_{cm}}{v'_b} = \left(\frac{m_a m_b}{m_X m_Y}\frac{T_a}{T_a + Q(1 + m_a/m_X)}\right)^{1/2} \tag{1.7}$$

these equations apply to a reaction of the form:

$$a + X \rightarrow Y + b \tag{1.8}$$

For our API system, which accelerates a mixture of deuterium and tritium ions towards a titanium target, the main nuclear reactions are:

$$D(T,n)\alpha$$
$$T(D,n)\alpha$$
$$T_2(D,n)\alpha$$
$$D_2(T,n)\alpha$$

Each of them results in a slightly different angle in the lab frame between the emitted neutron and alpha particle as given by Equation 1.6. There is also the possibility of reactions involving triatomic species. However, their proportion is very low for this type of ion source, and hence will not be considered in the analysis. Furthermore, since non-monatomic species are accelerated at a lower energy per nucleon for a given accelerating voltage, the cross-section also drops significantly. Experimentally, we do not have information as to which of these reactions took place in an event-by-event basis. Therefore, the differences in the kinematics

from all these reactions have to be considered. From Equation 1.6 we can calculate the uncertainty due to these effects from the point of view of the kinematics alone, which turns out to be approximately 0.9 cm averaged over all angles as measured 60 cm from the neutron source.

Alpha Particle and Gamma Ray Detection

Both alpha particles and gamma rays interact with matter mostly via electromagnetic processes with the atoms in the medium. Alpha particles with a higher linear energy transfer (LET) are more ionizing than gamma rays and therefore have a shorter range that is described by individual collisions of the alpha particle with surrounding electrons (electronic stopping). It is possible for alpha particles to interact with nuclei (nuclear stopping) but this process is significantly less common at high energies and hence most detectors rely on electronic stopping. Different materials can be used for the detection of alpha particles as reviewed extensively in [28]. However, API requires a fast response (rise time) for nanosecond timing, short pulses (decay times) for high-rate handling, and a large amount of ion-hole pairs released per interaction to minimize energy uncertainty needed for position reconstruction. Additionally, the detector material needs to be robust, easy to handle, radiation resistant, and able to withstand vacuum bakeout temperatures. Therefore, the choices were somewhat limited to fast inorganic scintillators such as Yttrium Aluminum Perovskite (YAP:Ce) or zinc oxide (ZnO:Ga). We decided to use YAP because even though it is slower and has a longer pulse than ZnO, it emits more light per interaction than the powdered form of ZnO [46] and is easier to handle in monolithic crystals that are not hygroscopic as opposed to ZnO. The advent of monolithic ZnO crystals could potentially be more beneficial as it would allow to handle higher rates. More details regarding specific properties and performance of YAP are presented in Chapter 2.

Gamma rays are more penetrating than alpha particles and can travel through air for several meters without interacting. Therefore, larger detector volumes are required to maximize efficiency. Apart from that, similar constraints as alpha detection apply to gamma detectors that are used for API. Furthermore, the detectors need to be rugged with no active cooling to allow for field deployment. The result is that HPGe detectors cannot be used for API because of their very long pulse widths and slow response which does not permit a time resolution better than tens of nanoseconds, and they require the use of cryogenics or expensive mechanical cooling systems. Therefore, the choices were again constrained to fast inorganic crystals. The state-of-the-art scintillator LaBr(Ce) is the best in terms of both fast timing and energy resolution. However, large crystals are more difficult to grow and they are significantly more expensive than other similar detectors such as NaI. In this work we used both LaBr and NaI in our API application. The NaI crystal (5-inch) is larger than LaBr (3-inch) and hence it can provide information from deeper layers. Additionally, for a commercial product requiring multiple detectors, NaI would drive the cost down significantly.

Depth [cm]	**Voxel size [cm^3]**	**(1±0.5)%C**	**(1±0.2)%C**	**(1±0.1)%C**
0 - 5	$5 \times 5 \times 5$	4 min	25 min	100 min
0 - 10	$10 \times 10 \times 10$	0.6 min	4 min	16 min
20 - 30	$10 \times 10 \times 10$	4 min	25 min	100 min
20 - 35	$15 \times 15 \times 15$	1.5 min	8 min	35 min

Table 1.2: MCNP6 simulation results for expected measurement times with two gamma ray detectors.

1.3 Feasibility Analysis

Measuring soil carbon with 14.1 MeV neutrons is not a new idea. A group at Brookhaven National Laboratory (BNL) implemented a system with a pulsed neutron generator but no API [56]. Therefore, their system provides an estimation of carbon abundance averaged over the field of view and depth with no position information, which leads to information from only the top few centimeters of soil. Additionally, the gamma spectrum is more difficult to analyze due to background contributions from reactions on structural materials of the interrogating system. In order to estimate measurement times for our system based on carbon content, we performed MCNP6 simulations and the results are summarized in Table 1.2. We used a generic dry soil composition ($\rho = 1.3\,\mathrm{g\,cm^{-3}}$) and a neutron source of 2×10^8 n/s located 60 cm above ground. The flux maps as a function of depth in soil are shown in Figure 1.4. Note that the measurement times can be reduced significantly if more gamma-ray detectors are used.

We also estimated the neutron scattering in the soil, which would add to the calculated error in the position reconstruction. A pencil beam of neutrons incident on soil was simulated and the position where a neutron produced a 4.4 MeV gamma from ^{12}C was tallied. The results are shown in Figure 1.5. The plotted curves show only the scattered neutrons at different depths, which represent 2% of the unscattered ones. Note that most of them are within 5 cm from the original direction of the neutron beam, and hence do not present a significant effect in the positional error. These simple simulations show that the system is in principle feasible and measurement times are reasonable.

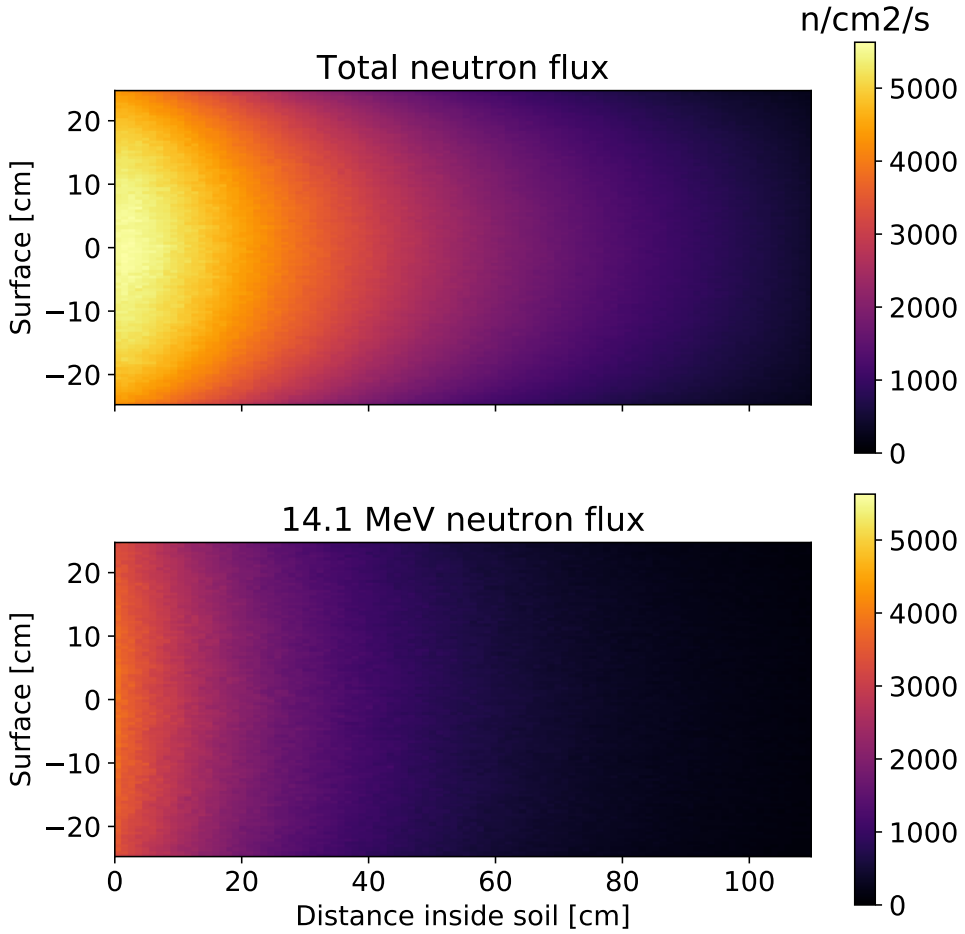

Figure 1.4: MCNP6 simulation of the total (top) and 14.1 MeV (bottom) neutron flux as a function of depth for a dry generic soil. The neutron source strength is 2×10^8 n/s. Note that only neutrons of 14.1 MeV are of interest for the API system since all others that produce a gamma ray will either be outside of the time window or have an incorrect location.

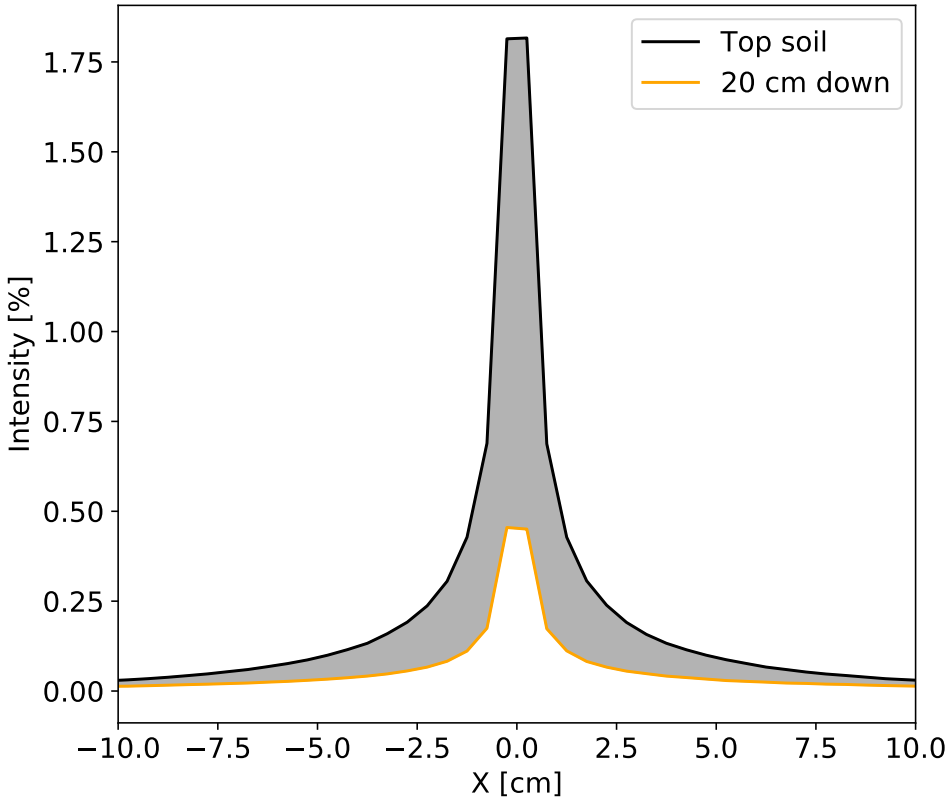

Figure 1.5: MCNP6 simulation of 14.1 MeV neutron scattering as it enters the soil. Most scattered neutrons are within 5 cm from the original direction of the neutron, and they only represent approximately 2% of all neutrons. The solid gray line shows the possible spread in scattered neutrons within the first 20 cm of soil.

Chapter 2

Position-Sensitive Alpha Detector

The purpose of the pixelated alpha detector is twofold: it is used to obtain the neutron starting time for time-of-flight measurements (depth resolution), and it allows for the calculation of the neutron direction of travel (X-Y resolution). The physical location of the alpha detector in the API system is shown in Figure 1.2 where the sapphire window acts as the vacuum interface and it allows the scintillation photons created by the alpha particles in the YAP to reach the position-sensitive photomultiplier tube. In this chapter, we present the design and performance characteristics of the detector. Simulations were performed to understand the range and energy deposition of alpha particles in our detector material, the resulting scintillation light spread onto the photocathode and its overall transmission, the optimal geometrical parameters of its components, and the performance of the electronics readout board among others. Additionally, we present experimental tests that provide information regarding its position resolution, uniformity, and rate capabilities among other characteristics. Some of the results and discussion presented herein have already been published and can be found in [50].

2.1 Initial Considerations

The project goal is to measure carbon in soil with a voxel resolution of 5 cm. Given that a 14.1 MeV neutron travels approximately 5 cm in 1 ns, the system as a whole (gamma detector plus alpha detector) needs to have a time resolution on the order of 1 ns. Additionally, in order to achieve a X-Y resolution in the soil of approximately 5 cm, the alpha detector needs to have a position resolution of ≈ 1 mm for the specific geometry given in Figure 2.1. However, this last requirement also depends on other parameters such as the neutron beam spot size, which can be one of the main contributors to the loss of resolution. The alpha detector should also be able to handle high rates on the order of 10^7 α/s at the maximum neutron output of the neutron generator, i.e. 2×10^8 n/s. The scintillator material of choice is the cerium-doped inorganic crystal Yttrium Aluminum Perovskite ($YAlO_3$) or YAP(Ce) due to the following reasons: it can withstand vacuum bakeout temperatures, it has a fast

response (rise time of approximately 3 ns), short decay time (27 ns), relatively high light yield (17000-20000 photons/MeV for gamma rays but $\sim 3-5$ times lower for alpha particles), high density (5.55 g cm^{-3}), and sufficient energy resolution (20% for a 5 MeV alpha). It is also non-hygroscopic and hence easy to handle.

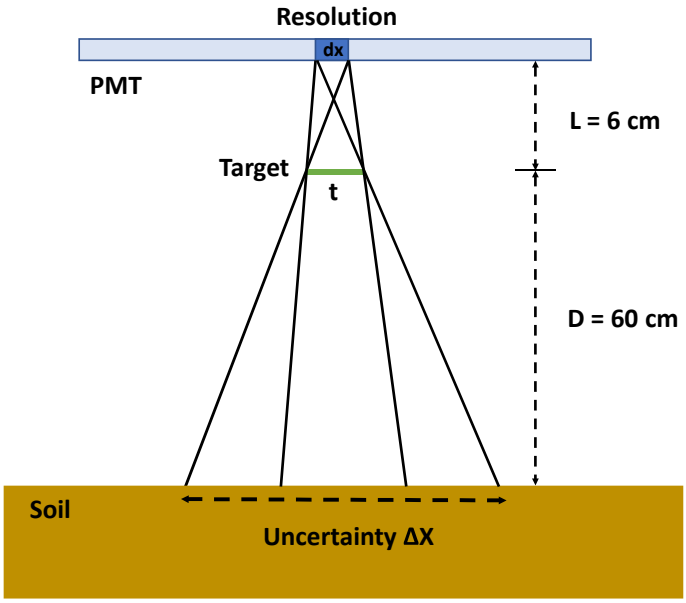

Figure 2.1: Effects of pixel resolution in the alpha detector (dx) on the overall system resolution for a given neutron beam spot size of $t = 2$ mm. For $dx = 1$ mm, $\Delta X = 3.2$ cm on the surface of the soil and $\Delta X = 4.7$ cm at a depth of 30 cm.

The dimensions of the YAP crystal used are 50 mm × 50 mm × 1 mm (manufactured by Crytur [12]) and it is placed inside the vacuum chamber approximately 6 cm from the titanium target where the neutrons and alpha particles are created. As the alpha particles enter the YAP crystal, they lose energy mainly due to collisions with electrons and thereby transfer their energy to the crystal. All alpha particles will stop within a few micrometers inside the YAP, as shown in Figure 2.2a. This process creates a large number of electron-hole pairs, which upon de-excitation through activator sites (cerium) emit optical photons with a primary wavelength of approximately 370 nm [28]. This wavelength is well-matched to our PMT spectral sensitivity, which peaks at 400 nm [20]. In the YAP crystal, approximately 6000 photons/MeV are emitted in a single 3.5 MeV alpha particle interaction [32]. The photons then propagate through a 3 mm-thick vacuum sapphire window (MPF Products [33]) to the photocathode of the PMT (Hamamatsu H13700-03 [20]). In order to further increase

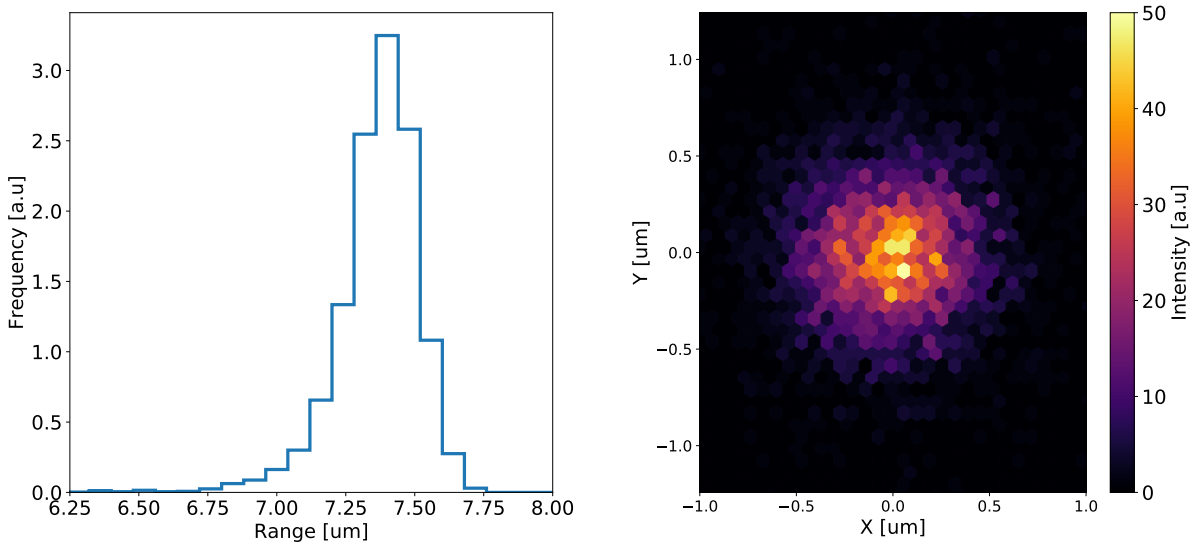

(a) Range

(b) Lateral spread

Figure 2.2: TRIM simulation of range (Z-direction) and lateral spread (X-Y) of 3.5 MeV alpha particles in YAP.

the number of photons reaching the PMT, the YAP surface facing the alpha source was coated with a 400 nm thick aluminum layer functioning as a mirror and as a ground plane to prevent the scintillator from charging up due to the deposition of positively charged alpha particles. During the final integration of the system with the neutron generator, an additional aluminum foil of 1 µm thickness is used in between the titanium target and the YAP crystal in order to provide a pinhole-free surface to protect the photomultiplier from ion source light. A layer of a certain thickness (for aluminum >1 µm) is also needed to prevent scattered deuterium and tritium ions from reaching the scintillator. The foil together with the existing coating of the YAP provides the required total thickness. The energy loss of the alpha particle in the foil is on the order of 50 keV as simulated with SRIM [64] and is therefore negligible. Sapphire was chosen as the vacuum window material for its superior optical properties and mechanical strength, which allows for a significant reduction of the required thickness of the window, and therefore reduces the spread of light from a single alpha-particle interaction onto the photocathode. This design differs from several other recent designs that use a fiber optic faceplate to couple the scintillator light to the PMT, such as in [63].

In order to calculate the range and lateral spread of 3.5 MeV alpha particles in YAP, the simulation software SRIM [64] was used where a layer of $YAlO_3$ was defined with a density of 5.55 g cm^{-3}. The simulation assumed alpha particles orthogonally incident on

the YAP surface (Z-axis). Figure 2.2a shows that most alpha particles stop in the material somewhere between 7 and 7.75 µm, and Figure 2.2b shows that the maximum lateral spread is approximately 1 µm. These numbers are used as input parameters for the subsequent COMSOL simulations presented in the following section.

In order to maximize the light yield, the YAP thickness needs to be larger than the range of a 3.5 MeV alpha particle in the material, which is approximately 7.4 µm, as shown in Figure 2.2a. However, using a very thin YAP is impractical in terms of fabrication and mechanical mounting/handling. On the other hand, the disadvantages of a thick YAP are that it allows for background X-rays and gamma rays to deposit more of their energy in the crystal thereby increasing the overall background rate.

The PMT is operated at a voltage bias of −1 kV and the anode is pixelated into an array of 16 × 16 individual electrodes, each of them with an active area of 2.8 mm × 2.8 mm and 3 mm center-to-center distance (information obtained from a previous but similar model H9500-3). The signals can be read out from those individual pixels as well as from the penultimate dynode, which serves as a common timing signal for fast timing applications.

2.2 COMSOL Simulations of Scintillation Photon Transport

The alpha detector system can be modeled with a geometrical (ray) optics approach because the wavelength of the scintillation light is much smaller than the dimensions of our system. Therefore, reflection, refraction, and absorption are the main physical processes that determine the performance of the alpha detector. Figure 2.3 shows a 2D schematic of scintillation light propagation in the system where a few ray traces are shown to exemplify the effects of total internal reflection and refraction in our specific geometry. The equation that describes such processes is called Snell's law and it is shown in Equation 2.1.

$$n_1 \sin\theta_1 = n_2 \sin\theta_2 \tag{2.1}$$

where n_1 and n_2 are the indices of refraction of medium 1 and 2, respectively, and θ_1 and θ_2 are the incident and refracted angles with respect to the normal.

An important consequence of this equation is the fact that total internal reflection, i.e. no transmission at an optical boundary, can only take place when light enters a medium with lower index of refraction, which in our case happens at the YAP–vacuum and sapphire–grease interfaces. Total internal reflection occurs when light rays with an angle greater than the critical angle θ_c are incident on a boundary, as shown in red (YAP–vacuum) and green (sapphire–grease) in Figure 2.3. The critical angle for the former case is approximately 31.2° and for the latter is 55°. Combining these two angles, we get an acceptance angle of $\theta_a = 26.8°$. Therefore, every light ray with an incident angle greater than θ_a will undergo total internal reflection at either of these two boundaries. This results in a cone of light being

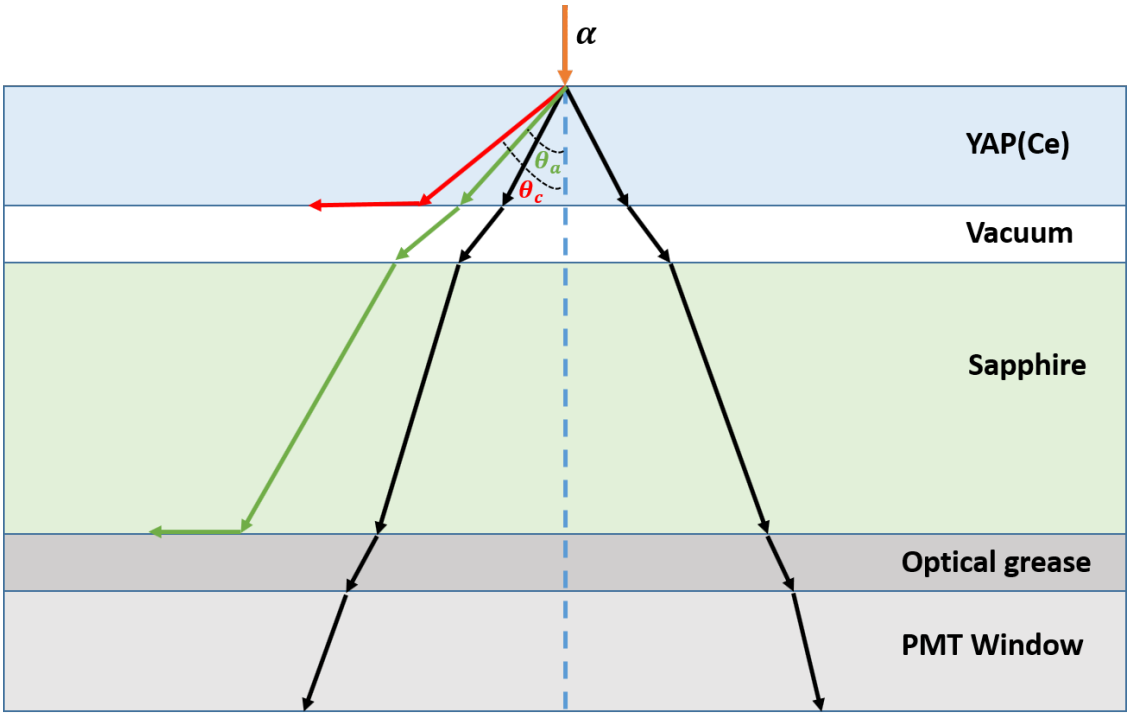

Figure 2.3: 2D schematic (not to scale) of some important features of light propagation through our system. Total internal reflection can happen at the YAP-vacuum and sapphire-grease interfaces. Therefore, only a narrow cone of light defined by the acceptance angle θ_a makes it to the photocathode. The rest undergoes total internal reflection and eventual absorption.

transmitted to the photocathode. In order to understand this process further and optimize certain parameters, we performed simulations of the entire system.

COMSOL Multiphysics [11] is a finite element analysis software that allows for simulations of physical processes by solving coupled systems of partial differential equations within elements of a specified geometry. It has a multitude of physics packages or modules for electromagnetism, fluid flow and heat transfer, structural mechanics, and chemical engineering. We used the "Ray Optics" module to simulate the light propagation throughout the alpha detector system. This module allows to model electromagnetic wave propagation with a ray tracing approach. These rays can be refracted, reflected, or absorbed at boundaries in the model geometry. The approximations used in this approach are appropriate for geometries larger than the wavelength of interest. Other software used for similar purposes include Zemax [61], and Geant4 [2].

These simulations are important in order to optimize geometrical parameters and estimate the amount of photoelectrons per alpha event that reach the photocathode, which directly influences the shape of the waveform. They also help us understand the light spread

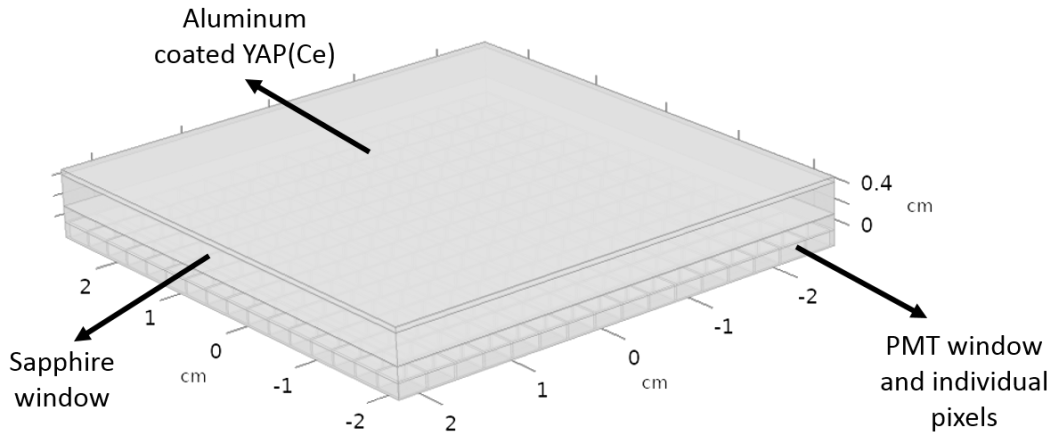

Figure 2.4: COMSOL geometry of the complete detector system

onto the photocathode, which influences the choice of reconstruction algorithm, and hence the ultimate attainable position resolution. Figure 2.4 shows the modeled geometry of our system. Table 2.1 shows the most relevant parameters used in the COMSOL simulations. The thicknesses of the vacuum layer and optical grease were not measured for practical reasons. However, simulations show that the results are almost completely independent of these two parameters assuming light absorption in the optical grease does not increase drastically within tens of micrometers. Table 2.2 shows some of the properties pertaining to the photomultiplier we use. This model is superior to the more conventional series H9500 [20] since it has a higher quantum efficiency and better pixel-to-pixel uniformity.

The PMT borosilicate glass window thickness and pixel spacing are set by the specifications of our photomultiplier. However, the other parameters can be varied. Particularly, the YAP and sapphire window thicknesses can be changed in order to control the light spread onto the photocathode. Since the sapphire window thickness is greater than that of the YAP, it is the component that mainly determines the spread of light onto the photocathode. It also serves as the vacuum interface, and hence it needs to be mechanically strong to counteract atmospheric pressure. We used COMSOL to increase the thickness systematically from 1 to 5 mm and the results are shown in Figure 2.5. We finally decided to use a 3 mm thick window as it provides sufficient mechanical strength and desired light spread.

Figure 2.6a shows that most photons from an alpha particle interaction do not reach the sapphire window due to total internal reflection at the scintillator-vacuum interface because of the mismatch between their indices of refraction. Due to the requirements of the neutron generator it is not possible to use optical grease to better match the indices of refraction at this interface. This effect has its advantages and disadvantages. For instance, a more localized photon distribution that activates only a few independent pixels could allow not only for a superior position resolution but also for higher rate handling capabilities depend-

Name	**Material**	**Thickness (mm)**	**Index of refraction** (370 nm)
Photocathode	Bialkali	–	–
PMT window	UV glass	1.5	1.5354
Optical grease	$PhenylSiO_2CH_3$	0.06	1.466
Vacuum interface	Sapphire	3.0	1.7925
Vacuum layer	Vacuum	0.005	1.0
YAP(Ce)	$YAlO_3$	1.0	1.931
Mirror layer	Aluminum	0.0004	–

Table 2.1: Main parameters used in COMSOL simulations. The thicknesses shown for the YAP and sapphire window are the ones chosen for the API system. Most values for the indices of refraction used were obtained from [42].

ing on the readout scheme. On the other hand, fewer photons reaching the photocatode translates into a degraded energy resolution, which directly affects the position reconstruction algorithm. Therefore, there exists an optimum trade-off depending on the requirements of the application. Simulations show that for a 3.5 MeV alpha particle only approximately 400 photoelectrons make it to the first stage of the dynode structure of the PMT (assuming 30% quantum efficiency), even though a total of approximately 21000 photons are created in the YAP crystal per alpha event. These simulations further show that light spreads approximately over a 3×3 array of pixels, as shown in Figure 2.6b.

The fact that there is a finite light spread onto the photocathode means the position resolution can be even smaller than the pixel size depending on what reconstruction algorithm is used e.g. center of mass reconstruction, Anger logic, etc. For example, J. W. Cates et al. [10] demonstrated a position resolution of < 0.5 mm with a similar experimental setup and using a 4-corner readout scheme.

As mentioned previously, one of the purposes of the 400 nm aluminum layer is to serve as a mirror, which increases the amount of photons transported to the photocathode. In order to quantify this improvement, we simulated $1/16^{th}$ of the alpha detector system with YAP and sapphire thicknesses of 1 and 3 mm, respectively. The results are shown in Figure 2.7.

Note that the diameter of the light projection onto the photocathode is relatively constant, i.e. 7.7 mm, but there is a twofold increase in transmitted light. These simulations also show a slight increase in background signal due to reflections from the mirror that make it to random pixels. However, observations show that this background does not affect the position reconstruction significantly.

Parameter Name	Parameter Value
Spectral response	185 – 650 nm
Peak wavelength	400 nm
Dynode	12 stages
No. of pixels	256
Pixel size / pitch	2.8 × 2.8 / 3 mm
Effective area	48.5 × 48.5 mm^2
Dimensional outline	52 × 52 × 33.3 mm^3
Operating temperature	0 – 50 °C
Quantum efficiency (420 nm)	30%
Transit time spread	0.38 ns
Maximum bias voltage	−1100 V

Table 2.2: Properties of the Hamamatsu H13700-03 position-sensitive photomultiplier tube.

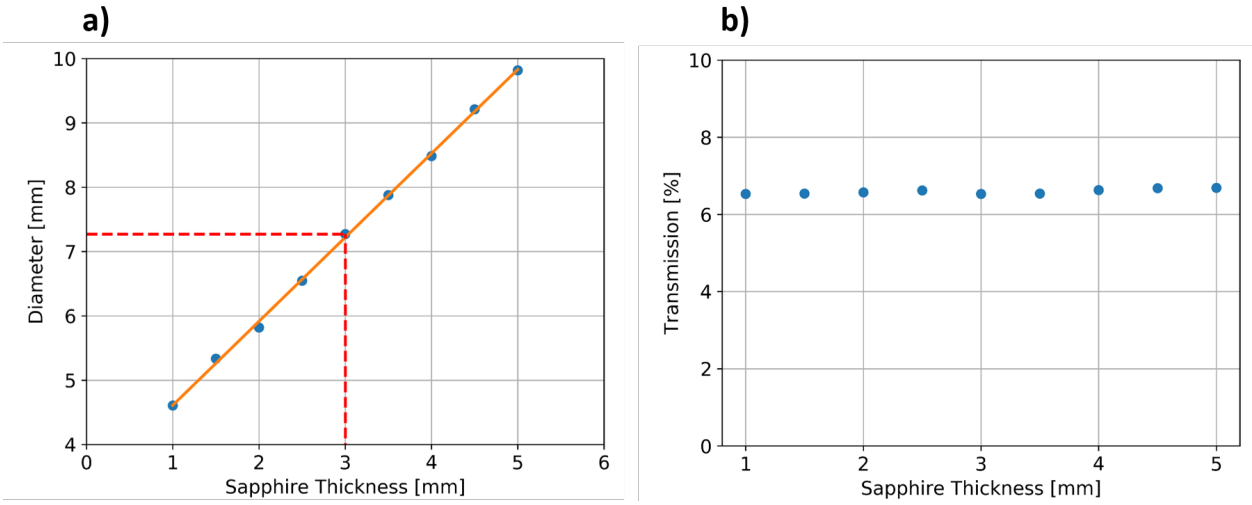

Figure 2.5: COMSOL simulation results of a) the light projection onto the photocathode, and b) the percent transmission of light that reaches the photocathode. Both results are for a single alpha event and they are plotted versus different sapphire window thicknesses. Note that the transmission is constant because most of the light is internally reflected within the YAP crystal. Based on these results, we decided to use a 3 mm thick sapphire window as indicated in a) with the red dotted line.

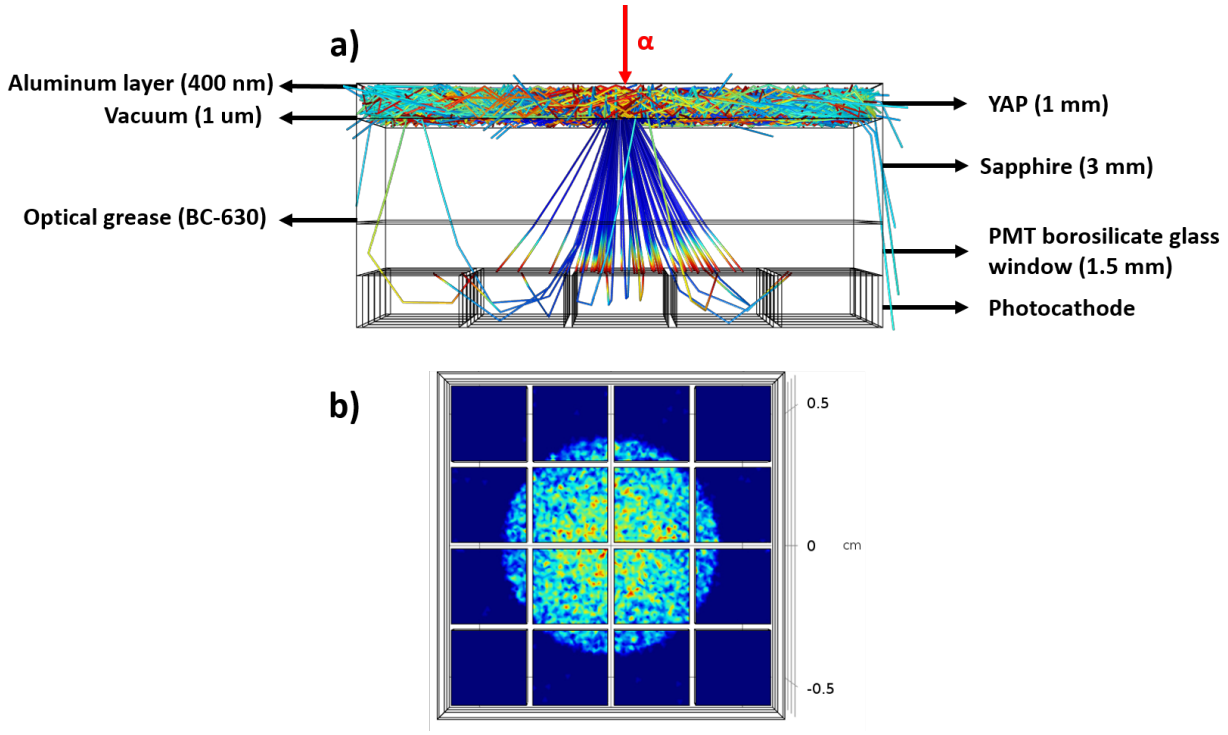

Figure 2.6: COMSOL Multiphysics [11] simulation of optical photon transport through one sixteenth of the alpha detector system showing a) the simulation geometry (side view) and ray tracing for a single alpha event, and b) the resulting light spread (top view) onto the photocathode. The pixel size of the detector is 2.8 mm and the pitch is 3.04 mm.

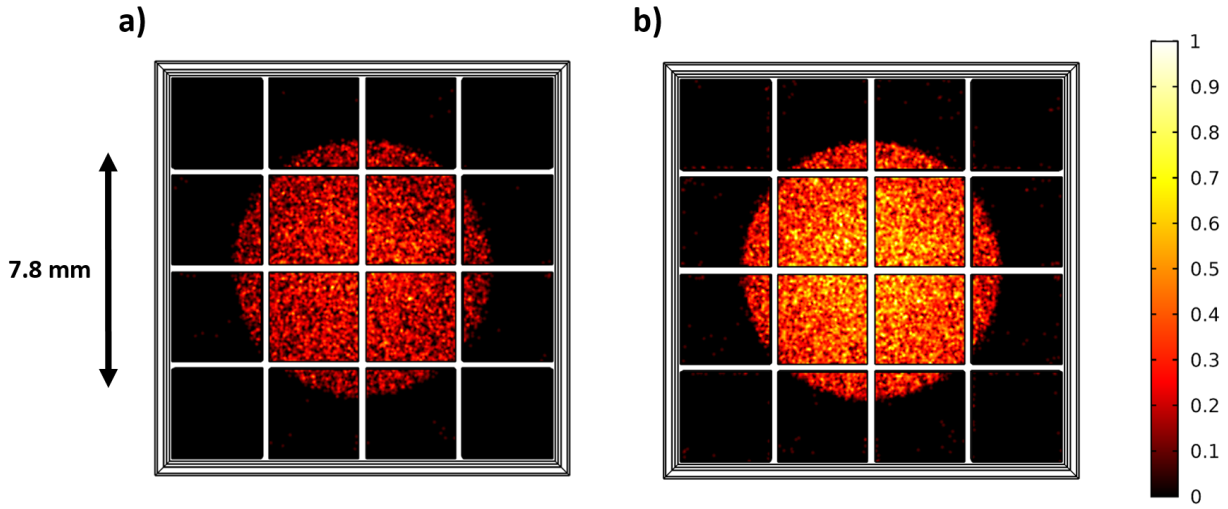

Figure 2.7: COMSOL simulation of scintillation photon transport through one sixteenth of the alpha detector system showing a) the transmitted light with no mirror surface, and b) the increase in transmitted light due to the mirror. This improvement scales by a factor of 2, making the total transmission approximately 6.6% with no significant change in diameter of the light projection onto the photocathode.

2.3 PMT Resistive Readout

Several options exist for the PMT electronic readout. All 256 pixels can be connected using a resistive network where only four corners are read out as shown in Figure 2.8. This is the more traditional method implemented in systems such as in [45]. However, the high alpha rates expected can be a limitation for this scheme because every alpha event would create a signal regardless of where the interaction took place and hence it would induce a certain dead time. In order to overcome this, another option is to connect the rows and columns into single measurements units such as in [40], which decouples each anode output into two directions (X and Y). This causes a single alpha event to activate approximately 3 rows and 3 columns as indicated by the COMSOL simulations in Figure 2.4 causing a dead time only in that region. Therefore, higher rates can be handled ($\approx \times 3$), and if loading resistors are added, a gain correction per pixel can be implemented. However, data analysis is more involved, more digitizers are needed (a total of 32), and the board layout becomes more complex given the large increase in number of resistors and the higher chances for cross-talk. Finally, the highest signal rate could be handled by digitizing every pixel. However, the data rates to be analyzed become increasingly large, and 256-channel digitizers would probably have to be implemented in a custom field-programmable gate array (FPGA), which would increase costs and development time significantly. On the other hand, this may be the most cost-effective option in the long run if mass production of this system is required.

We decided to first implement a 4-corner readout scheme to understand its rate limitations and position resolution. The approach was based on [45] and [37]. The resistive network was analyzed using the software package LTspice [31] and designed to minimize distortion. For this purpose, the side resistor values shown in Figure 2.8 were chosen in order to provide a linear response with respect to interaction location.

The PMT signals were appropriately shaped by XIA-designed pre-amplifier circuits with $\times 10$ gain and a low-pass filter to enable optimal arrival time detection in a fully digital Pixie-16 system (500 MHz) from XIA [57]. The pre-amplifier schematic is shown in Figure 2.9.

The Pixie-16 was set up to trigger on the last common dynode (timing channel) of the PMT (the signal from the four corners has slower rise times due to the resistive network) and for each trigger the energies from the corners were automatically recorded. The position of interaction in the scintillator was then calculated using Equation 2.2.

$$x = \frac{A+B}{A+B+C+D}, \quad y = \frac{A+C}{A+B+C+D} \tag{2.2}$$

where A, B, C, and D are the measured energy values of the signals at each corner, respectively. This equation is somewhat analogous to finding the center of mass in a system where four objects with different masses are placed at the corners of a two-dimensional grid. Typical digitized waveforms of such an alpha interaction in YAP are shown in Figure 2.10.

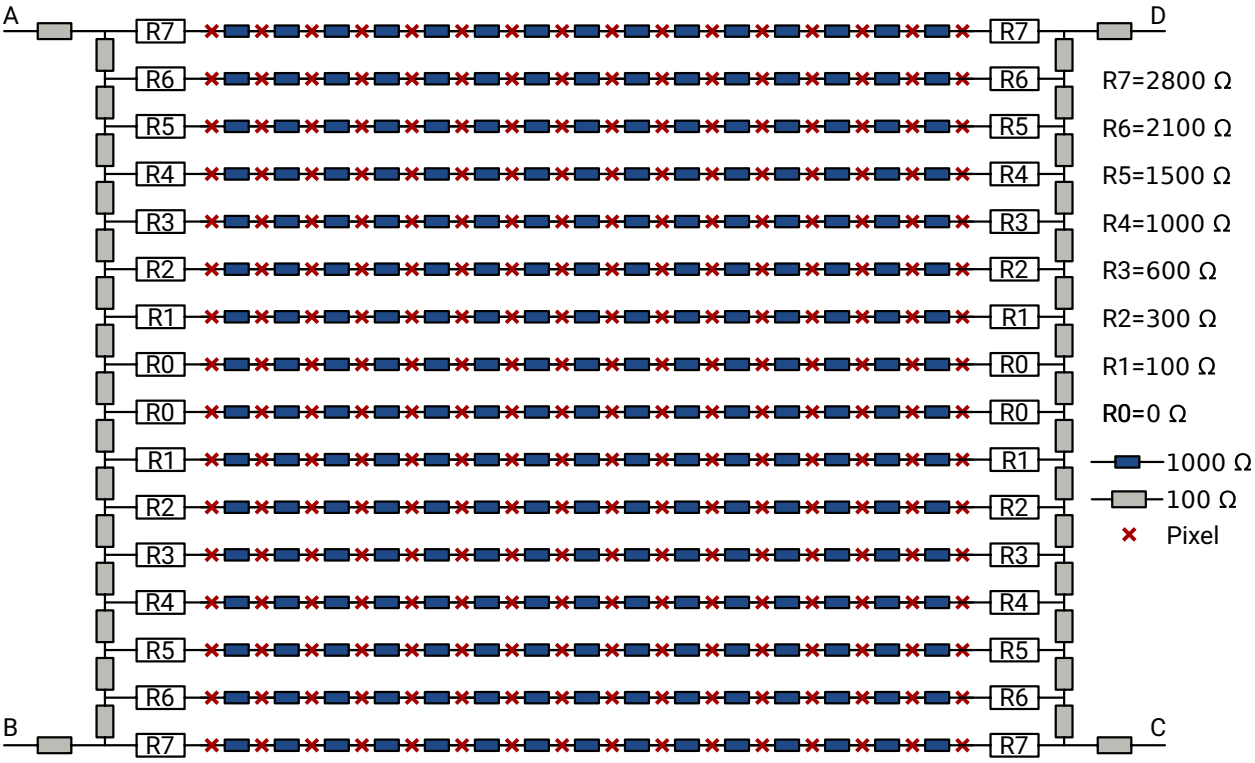

Figure 2.8: A schematic of the 4-corner readout board. Rows of pixels are connected with 1 kΩ resistors (blue) and terminated with a varying resistor at the end of each row. The rows are then connected using 100 Ω resistors (gray). The resulting four corners are each connected to a pre-amplifier circuit, which sends the signals to the digitizer.

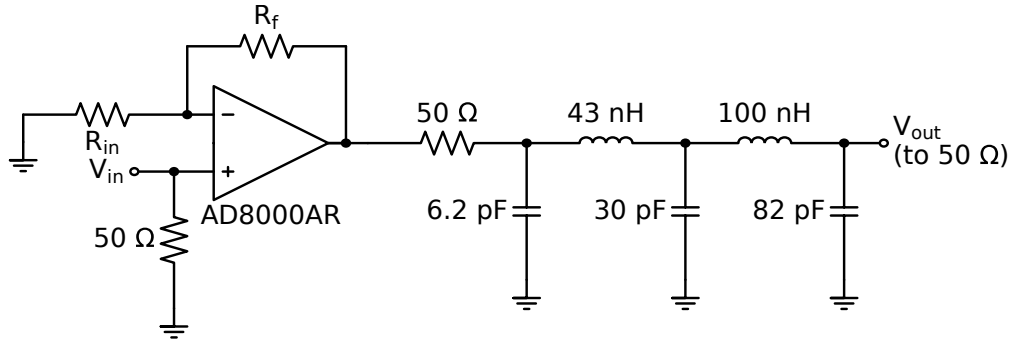

Figure 2.9: The pre-amplifier design from XIA [57] used for signal amplification as well as for filtering of the signal for optimal digitization in the Pixie-16 system. The amplification factor is variable and depends on the ratio of the two resistors labeled R_{in} and R_f.

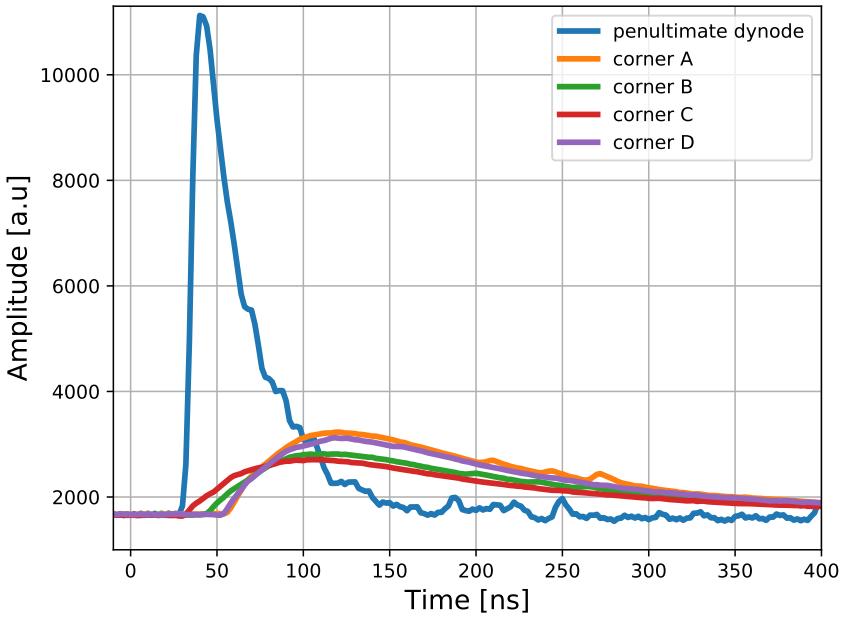

Figure 2.10: Digitized traces from the last dynode of the PMT and from the 4 corners of the readout board. The traces from the four corners have a lower amplitude due the fact that the signal is distributed between the four corners and their rise time is lower due to additional RC delays from the resistive network. The average amplitude of the penultimate dynode signal for a 5.5 MeV alpha is approximately 400 mV when the PMT is operated at −1000 V.

SPICE Simulations of the Four-Corner Resistive Readout Board

LTspice is a SPICE simulation software for analog circuit design [31]. It has a graphical interface where we implemented the four-corner readout layout shown in Figure 2.8. In order to test the linearity of the output, which is mainly a function of the side resistors R_0 – R_7, a DC current source was connected to every pixel (red crosses in Figure 2.8). The input current source was taken from COMSOL simulations shown in Figure 2.7. We measured the voltage drop across the 50 Ω resistor located at the end of each corner. We then used Equation 2.2 to calculate the resulting position. For a more accurate result, we simulated alpha particles arriving on a regular grid, which resulted in approximately 3500 individual simulations. Because of this large number, the process was automated using Python and ngspice [38], which is a command line based simulator that can take LTspice output files. The result is shown in Figure 2.11.

This result increased our confidence in the board design that is used in the system. Note that the 50 Ω resistors at the corners are needed to match the impedance of the DAQ, and hence avoid signal reflections. However, also notice that there is a non-linear edge effect due

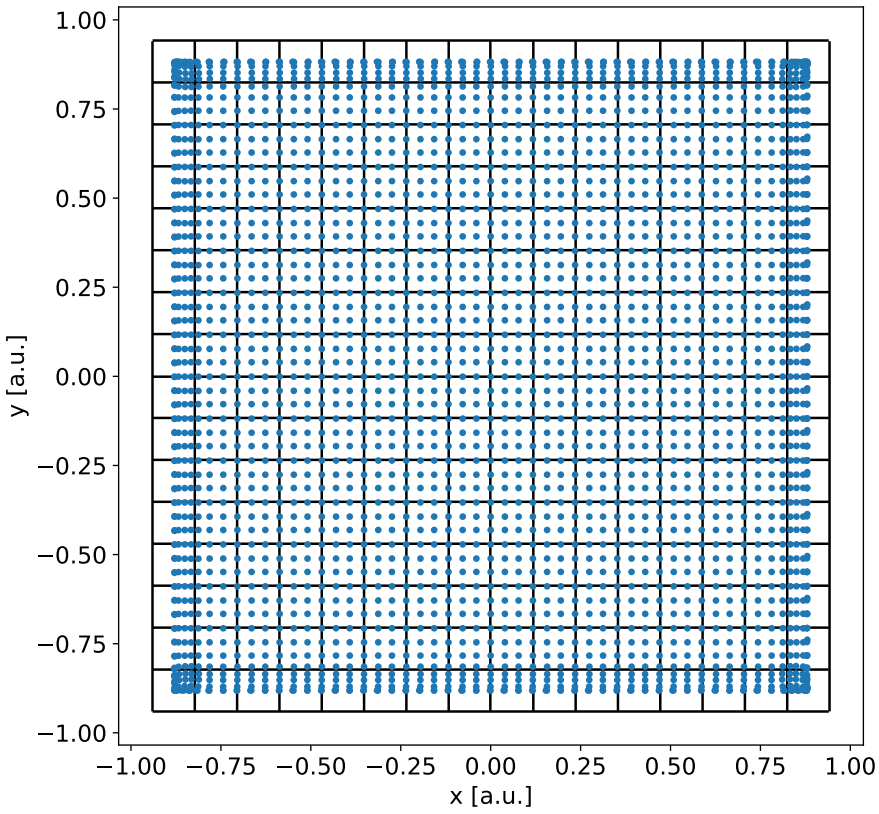

Figure 2.11: LTspice output showing the resulting calculated position from a distributed DC current source from COMSOL simulations applied every 0.9 mm. This source is used as a proxy for an alpha particle interaction. Simulations show a high degree of uniformity except at the edges.

to two processes: 1) edge events produce fewer scintillation photons. This effect reduces the amplitude of the signal at the 4 corners, which in turn results in increased signal noise and a more inaccurate position reconstruction, and 2) the location of interaction as given by Equation 2.2 yields incorrect results because it computes the "center of mass" of an incomplete circle, which is biased inwards. This effect is discussed in more detail in the following section.

2.4 Experimental Tests and Outlook

In order to quantify the position resolution and uniformity of the alpha detector, aluminum masks with different hole patterns were placed in between an ^{241}Am (3.9 MBq) alpha source and the YAP crystal in a 6-inch cube vacuum chamber. ^{241}Am decays primarily by the emission of an alpha particle with an average energy of approximately 5.5 MeV. Even though the energy of the alpha particles emitted by ^{241}Am is higher than the 3.5 MeV alphas from the DT reaction, it bears no significance in terms of position resolution nor overall uniformity. Figure 2.12 (left) shows a "flood-field" mask with 256 holes separated by 3 mm center-to-center, which is the same as the separation between individual pixels.

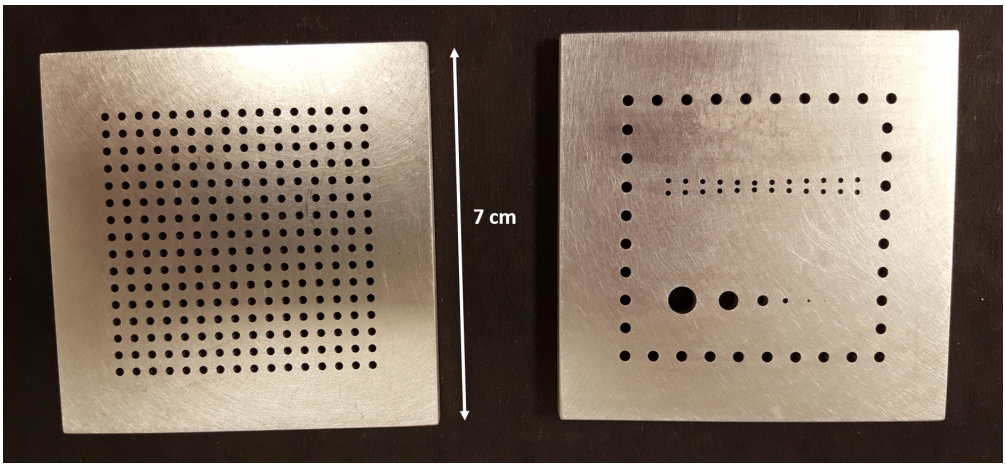

Figure 2.12: Different aluminum mask designs used for the alpha detector performance tests. The flood-field mask on the left has 256 holes separated by 3.04 mm, which is the same separation as the pixel-to-pixel center of the PMT. The mask on the right was designed to measure the ultimate position resolution of the alpha detector.

The mask was placed in between the ^{241}Am source and the YAP crystal at a relative distance of approximately 10 cm from each other, the chamber was evacuated to a few mTorr, and coincident data was taken for 200 seconds. The 6-inch flange with the sapphire window, YAP holder, and mask are shown in Figure 2.13.

The reconstruction was performed using Equation 2.2, and the result is shown in Figure 2.14b. Note the high spatial uniformity except near the edges where light spread is not uniform. Therefore, only a small correction is needed in this particular setup. In chapter 6, we show how a thinner YAP crystal improves the resolution.

Notice how even though a 16×16 mask was used, only a 14×14 array is observed in Figure 2.14b. In order to understand this effect, we performed another set of experiments where all the holes were covered except for the outermost ones (Figure 2.15b). Then, we only covered the outermost holes (Figure 2.15a). We later superimposed these two results and noticed an overlapping at the edges, as shown in Figure 2.15c. This effect is predicted

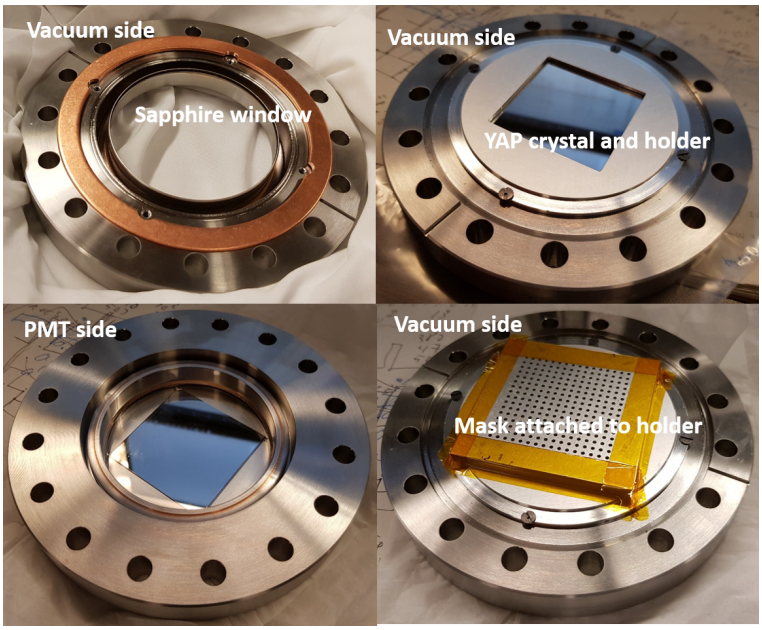

Figure 2.13: Setup used to test different YAP crystals, reconstruction algorithm, and overall uniformity. The sapphire window, YAP, and aluminum holder shown are the same as the ones used in the neutron generator.

in the LTspice simulations shown in the previous section. We can either mask the inside border of the YAP crystal and have a smaller field of view or we can perform a correction in software based on simulations. Both options are being considered for an improved setup that is currently under development.

Another experiment in the 6-inch cube was performed in order to quantify the position resolution of the alpha detector in isolation from the overall system. For this purpose, a mask was machined with a hole pattern with decreasing center-to-center distance, as shown in Figure 2.12 (right). The results are shown in Figure 2.16. Notice that even the holes that are 0.2 mm apart (edge-to-edge) can be resolved with our current setup, which improves upon previous work such as [63].

In summary, the alpha detector was designed, simulated, and tested in order to characterize its performance independently from the overall system. A position resolution of 0.2 mm was demonstrated, which surpasses the requirement of < 1 mm for a system resolution of less than 5 cm. Additionally, the detector shows a high degree of spatial uniformity, which makes it possible to use the algorithm with a minimum of software corrections. A summary of the most important results from the simulations and experiments presented in this chapter are shown in Table 2.3.

As for future improvements, the measurement time of carbon in soil (or any other sample) needs to be short for a commercial system, which translates into being able to operate at

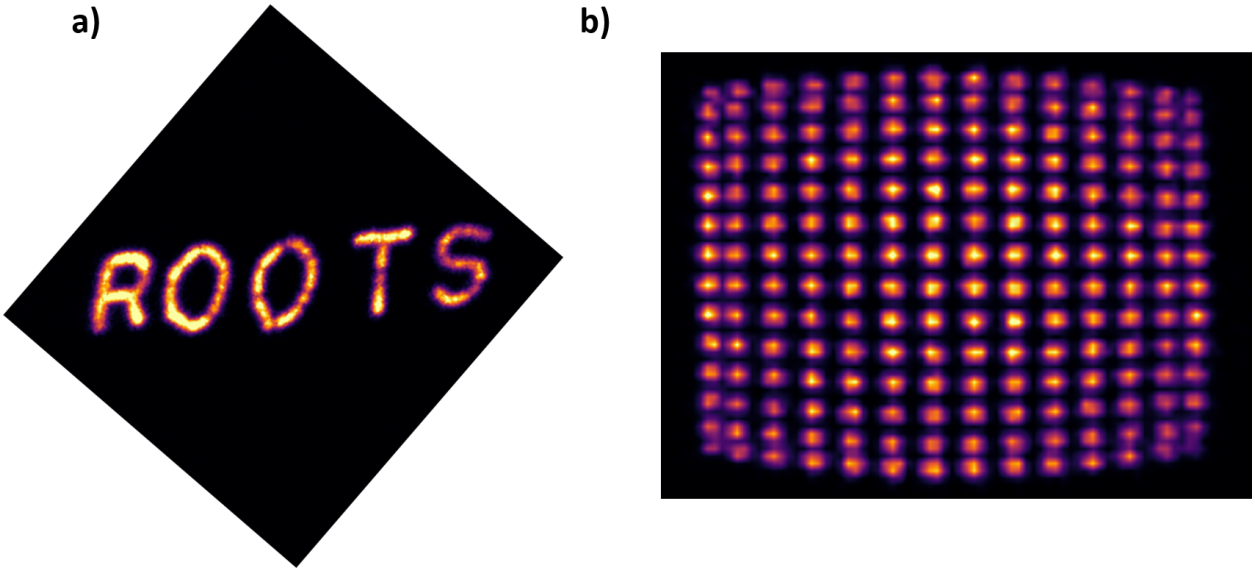

Figure 2.14: Position reconstruction of different mask configurations designed to characterize the resolution and reconstruction algorithm of the alpha detector. The figure on the left (a) is the result of an aluminum mask with several small punched holes that spell out the word "ROOTS", and the figure on the right (b) is the mask shown on the left of Figure 2.12.

higher rates. Therefore, an important improvement would be to increase the rate capabilities by implementing a new readout board that decouples several pixels so the system can handle higher alpha rates. Therefore, a 16×16 resistor board was designed and will be tested at LBNL, which would allow for a ×3 improvement in rate capabilities together with the option of pixel-by-pixel gain correction for even greater uniformity. This hardware implementation together with an improved pileup correction algorithm in the PIXIE-16 will allow for even higher alpha rate handling capabilities. Additionally, the system performance can be further improved by mounting a thinner YAP crystal which allows for a lower energy deposition from X-rays and gamma rays thereby reducing unwanted background. Preliminary testing of a 0.1 mm thick YAP for the next generation API system achieved better results and are shown in Chapter 6.

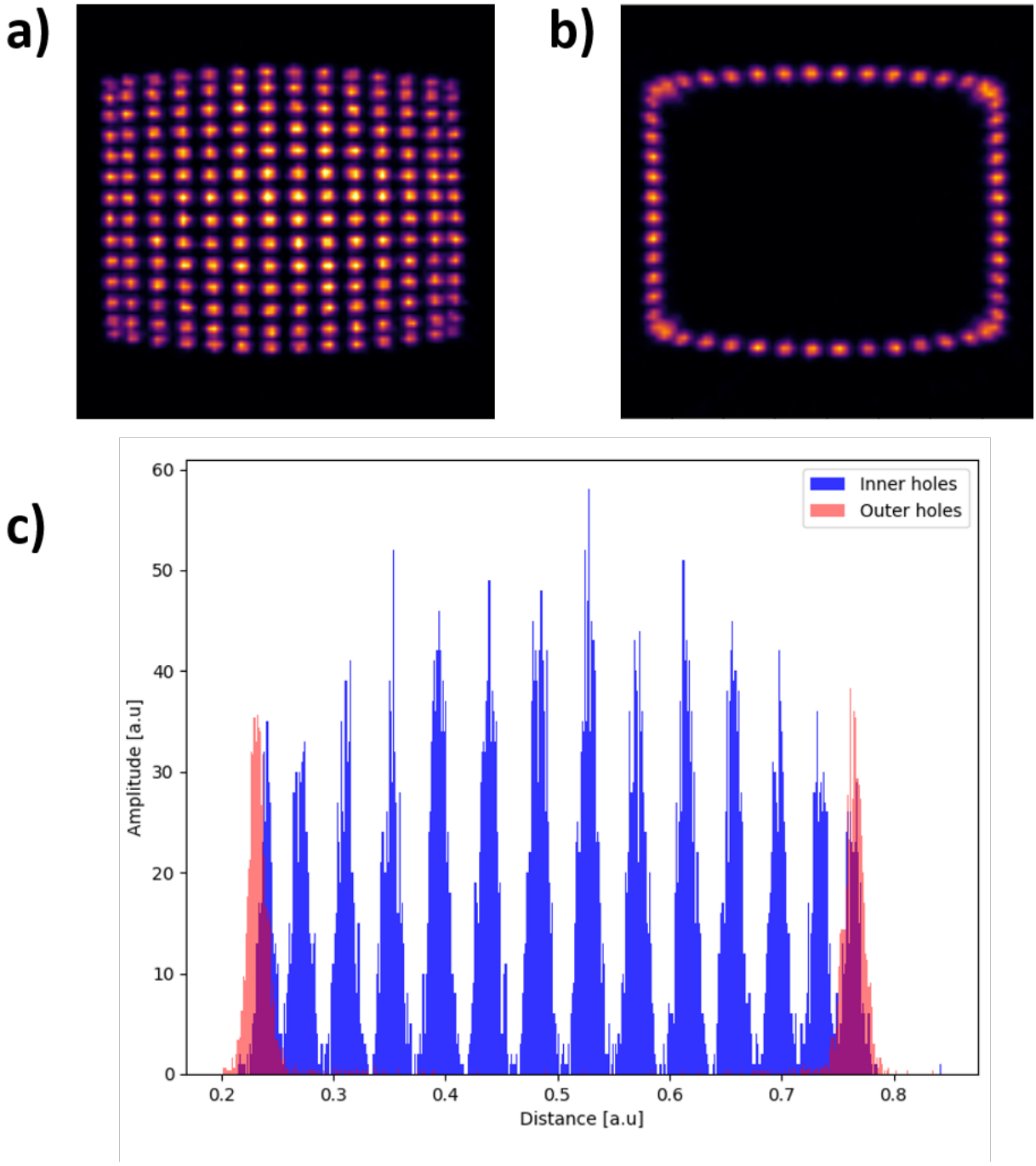

Figure 2.15: Edge effects in the alpha detector system showing an overlap of the outermost holes with the immediately preceding ones. a) shows the mask with 16×16 array of holes with the outermost holes covered so no alpha particles can go through them, b) shows the the same mask but with only the outermost holes uncovered instead, and c) is a 1D projection of a single (center) row with results of a) and b) superimposed.

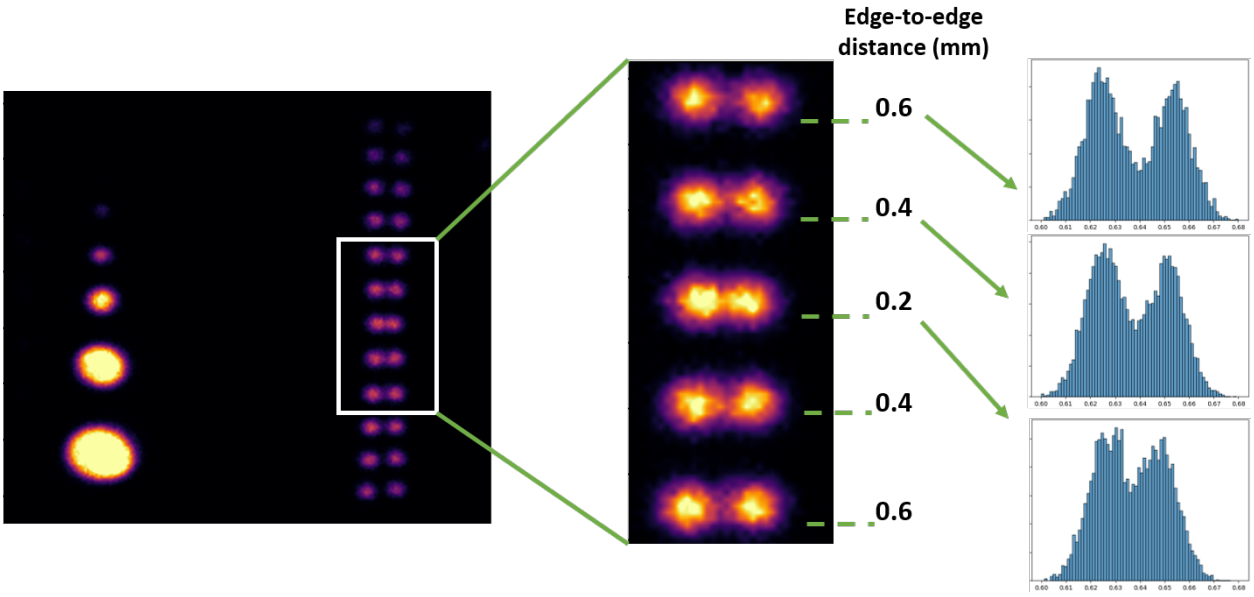

Figure 2.16: Position resolution test of our detector system showing a series of holes separated by varying distances. Note that the minimum separation between the holes (edge-to-edge) is 0.2 mm and they can still be clearly resolved.

Range of 3.5 MeV alphas in YAP	7.4 µm
YAP thickness	1.0 mm
Sapphire thickness	3.0 mm
Diameter of light projection on photocathode	7.7 mm
No. of pixels hit per alpha	3×3
No. of photoelectrons per alpha at first dynode stage	400
Light transmission YAP–PMT	6.6%
Measured position resolution	0.2 mm

Table 2.3: Summary of simulation and experimental results.

Chapter 3

Gamma Detectors, Data Acquisition System, Energy, and Time determination

The characterization of both gamma detectors (LaBr and NaI) and the optimization of the parameters and algorithms used by the DAQ are important for the optimal operation of the API system. In this chapter we present the main features of the DAQ in regards to energy and time determination, and we make recommendations as to what parameters are best suited for API measurements. Additionally, we model the response of LaBr in MCNP6 and compare the results to experimental data. We mostly present results for LaBr because of its superior energy and time resolution. However, similar conclusions apply to NaI.

3.1 Digital Energy Filter

The PIXIE-16 implements a variation of a trapezoidal filter in order to account for high rate environments, which allows for some degree of pileup correction in the sense that it can correctly measure the energy of a pulse that is on top of another pulse having a single decay constant. The basics of trapezoidal filtering is not discussed here, but can be found in the literature such as in [24]. In order to illustrate the PIXIE-16 algorithm, refer to Figure 3.1 where two arbitrary digitized traces are shown with a sampling frequency of 500 MHz, just like it is done in the DAQ. The filter is for the most part described in [47]. The goal is to calculate the shaded area J and baseline C assuming a single known decay constant τ of the trace, which depends on the type of detector used. The Digital Signal Processing Unit (DSP) uses three running sums S_1, S_2, and S_3 of widths L, G, and L, respectively.

Let A be the amplitude of the trace at the beginning of S_1. The respective sums can then be expressed as follows:

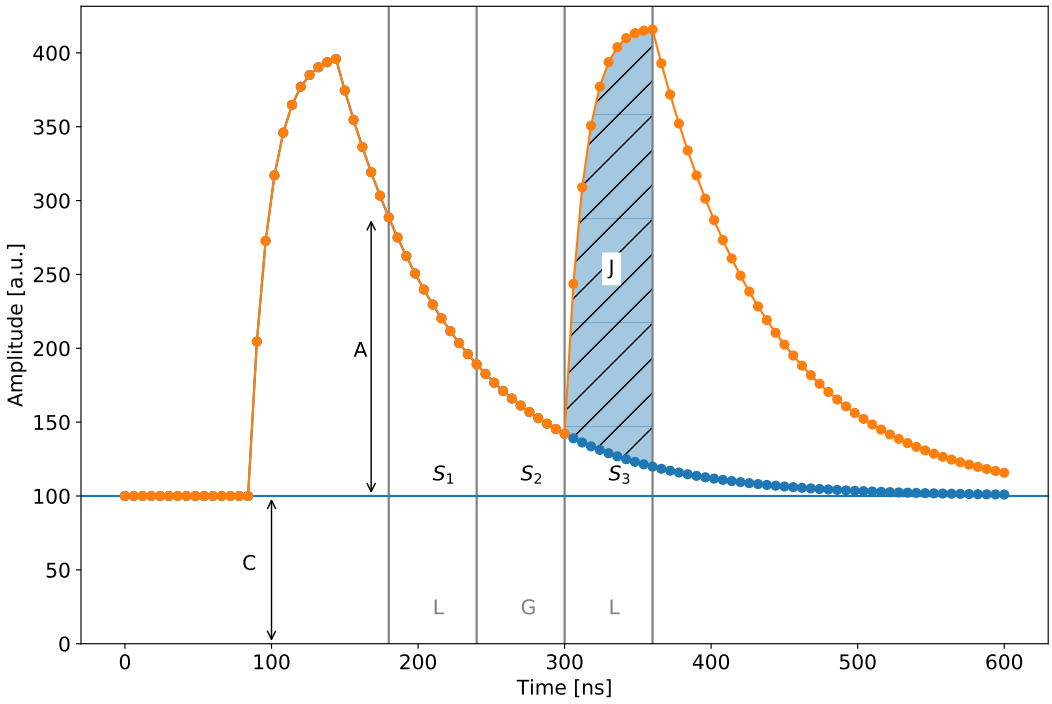

Figure 3.1: Arbitrary digitized traces as it is done in the DAQ PIXIE-16 showing the steps used in the algorithm for energy determination and pileup correction.

$$\begin{aligned} S_1 &= A\frac{1-q^L}{1-q} + CL \\ S_2 &= Aq^L\frac{1-q^G}{1-q} + CG \\ S_3 &= Aq^{L+G}\frac{1-q^L}{1-q} + J + CL \end{aligned} \tag{3.1}$$

where $q = e^{-\Delta t/\tau}$ and Δt is the sampling interval, i.e. 2 ns for the PIXIE-16. The energy is then calculated as shown in Equation 3.2

$$\begin{aligned} E &= -\frac{1-q}{1-q^L}q^L S_1 + (1-q)S_2 + \frac{1-q}{1-q^L}S_3 \\ &= \frac{1-q}{1-q^L}J + (1-q)C(L+G) \end{aligned} \tag{3.2}$$

Note that the second term of this last equation is just the baseline of the trace times some constants. Therefore, it can be subtracted to yield Equation 3.3

$$E - baseline = \frac{1 - q^L}{1 - q} J + noise \tag{3.3}$$

The value "$E - baseline$" is the value the PIXIE-16 calculates internally and reports as the energy for each trace. In order to verify that this algorithm works as implemented in the FPGA, we performed an experiment with a ^{22}Na radioactive source and captured individual traces. Then, each trace was run through the algorithm above and compared to the reported energy. This comparison is shown in Figure 3.2, which also shows some of the intrinsic spectral features of LaBr due to its internal radioactivity. This activity is mainly due to ^{138}La and ^{227}Ac; the latter being an impurity in the lanthanum extraction process. ^{227}Ac decays primarily by alpha emission with energies greater than 2 MeV, and hence are not shown in Figure 3.2. Note this procedure shows that we can reproduce the energy calculation as reported by the PIXIE-16 with a high degree of confidence, which allows us to optimize certain parameters directly in software.

The isotope ^{138}La constitutes 0.089% of natural lanthanum and it decays with a half-life of 1.05×10^{11} years via electron capture ϵ (65.6%) or β^- (34.4%) into ^{138}Ba and ^{138}Ce, respectively. The decay scheme is shown in Figure 3.3.

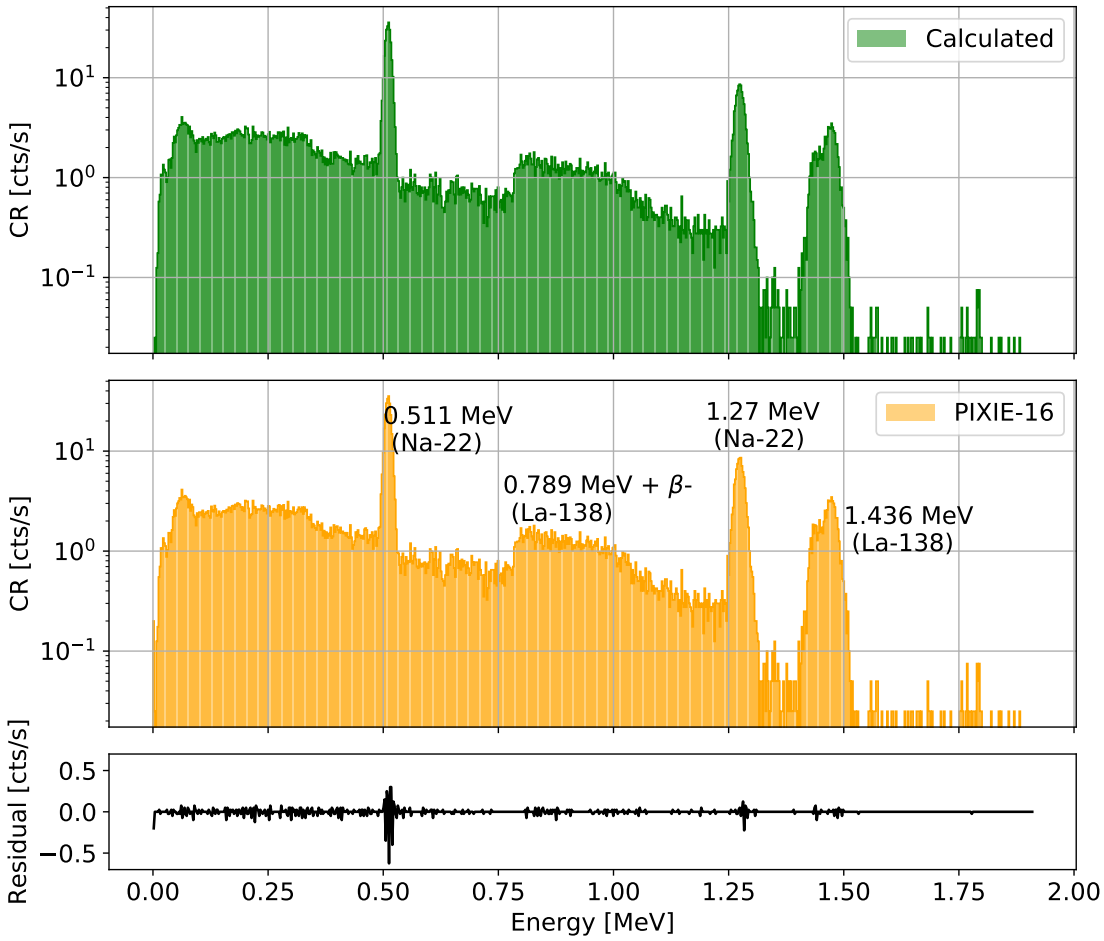

Figure 3.2: Comparison between PIXIE-16 reported energy and energy calculated based on raw traces using the algorithm shown in Equation 3.3.

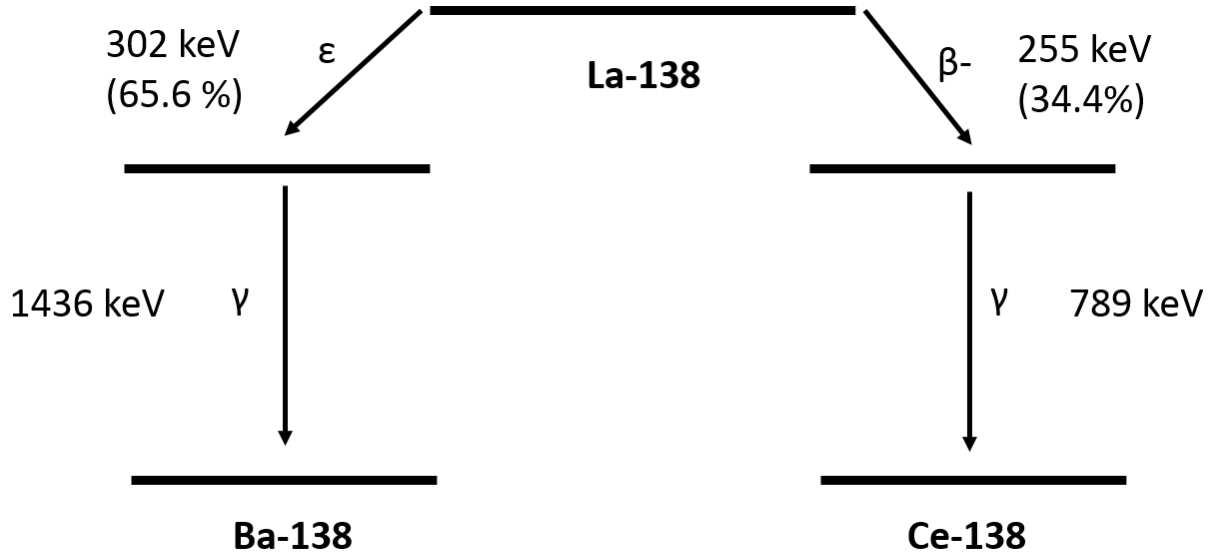

Figure 3.3: Decay scheme of ^{138}La that explains the internal radioactivity of the detector. Note that when data is taken in API mode, the energy deposition from these types of radiation do not appear in the spectrum because of the coincidence logic.

3.2 Constant Fraction Discrimination (CFD) Algorithm for Determination of Arrival Times

The arrival times of the alpha particle and the gamma ray need to be measured with a certain precision in order to calculate the neutron time of flight and hence the depth of interaction. One of the objectives of the project is to obtain a depth resolution of 5 cm, which requires a time resolution of approximately 1 ns, as explained in the introductory chapter. The time resolution depends on the intrinsic properties of the detector and the related electronics used to process the signal. Detectors with fast charge collection yield better timing performance. This is the case for YAP and LaBr. NaI has a longer charge collection time and hence we can expect its time resolution to be worse than the other two. Among YAP and LaBr, both having similar charge collection times, the best timing performance is obtained with LaBr because it generates the greatest number of information carriers (electrons) per interaction, and hence the arrival time is less influenced by the signal noise [28]. Traditionally, the best timing performance is achieved with analog systems, which are not limited by quantization in time as opposed to digital systems. However, the advantages of digital acquisition systems outweigh this limitation. Digitization of a signal provides complete information about the detected event, which allows for noise filtering, corrections for baseline shifts and pileup among others. Both digital and analog systems suffer from time walk and jitter. The latter is the error in timing accuracy due to noise in the waveform, which originates from

a variety of sources including electronic noise and average number of information carriers produced per interaction. Depending on the algorithm used to determine the arrival time, different pulse amplitudes can lead to different arrival times, as shown in Figure 3.4. This is known as time walk. For instance, a simple threshold is not appropriate for situations where a large energy spread (dynamic range) is expected, such as in this application. There are many techniques that can be used to obtain time information from a pulse. However, not all of them apply equally well to our specific application. The simplest technique is known as leading edge discrimination (LED), which uses a simple threshold as explained in Figure 3.4 (right). This technique is appropriate for situations where the dynamic range is small. The PIXIE-16 implements what is known as a digital constant fraction discrimination algorithm (CFD) in order to obtain the time of arrival of a pulse. This method originates from analog techniques, and its advantage over other methods such as LED is that time walk is significantly reduced because it determines time at a constant fraction of the pulse amplitude, as shown in Figure 3.4 (left). A simple illustration of the analog CFD technique is shown in Figure 3.5. The pulse is inverted, delayed, and the amplitude reduced by a constant fraction. Then, it is added to the original pulse, which results in a bipolar signal. The zero crossing of this signal is taken as the arrival time.

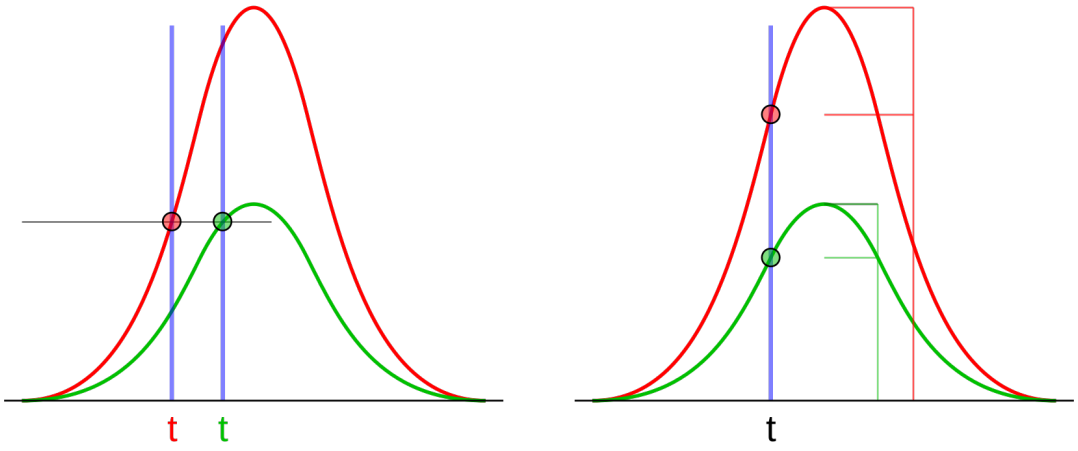

Figure 3.4: Difference between two common timing techniques: leading edge discrimination (LED) and constant fraction discrimination (CFD). The advantage of CFD is that the time of arrival is independent of the pulse amplitude, which is important in applications where a wide energy range is expected. Image taken from [14].

The CFD algorithm implemented in the PIXIE-16 (500 MHz ADC, rev. F) follows the standard analog technique closely and it is shown in Equation 3.4, which has four free parameters that can be optimized, i.e. w, B, D, and L. The constant fraction w varies

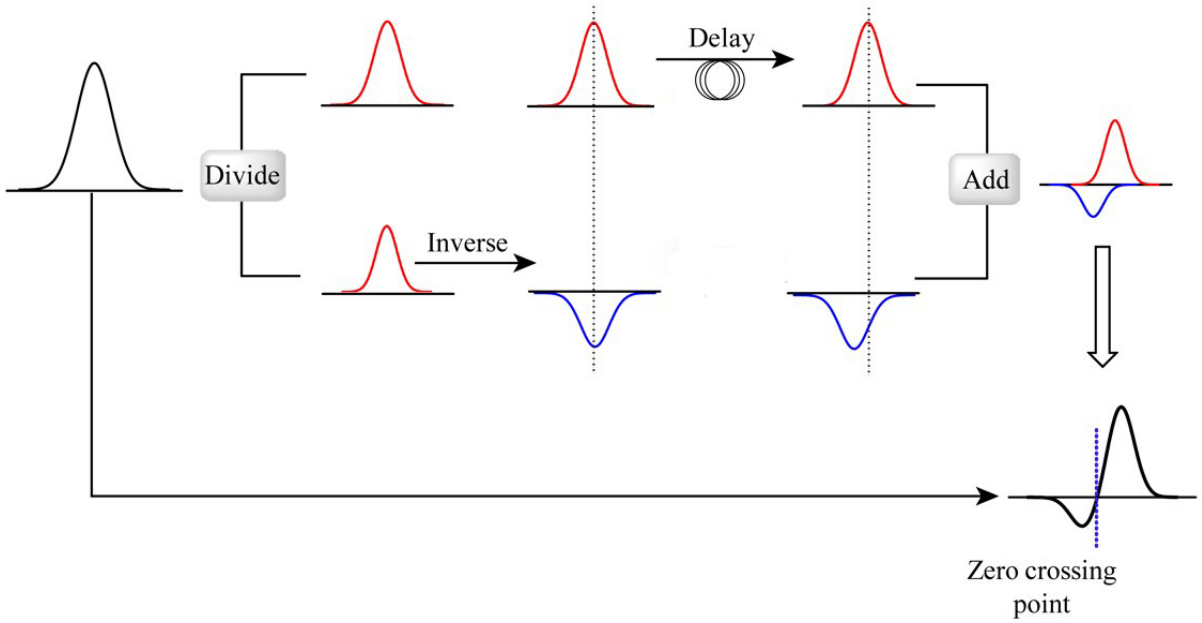

Figure 3.5: Simplified concept of the CFD technique showing the most important steps in the calculation. The zero crossing point is taken to be the time of arrival. Image taken from [48].

between 0 and 1, and the other three are integer values equal to a certain number of points in the digitized trace. Finally, the ADC trace data is $a(i)$.

$$CFD(k) = w\left(\sum_{i=k}^{k+L} a(i) - \sum_{i=k-B}^{k-B+L} a(i)\right) - \left(\sum_{i=k-D}^{k-D+L} a(i) - \sum_{i=k-D-B}^{k-D-B+L} a(i)\right) \tag{3.4}$$

However, this CFD algorithm is not very flexible because the values are hard-coded in this version of the PIXIE-16. The reason for this is that although the speed of the ADC is 500 MHz, that of the FPGA is only 100 MHz. Therefore, the ADC data rate needs to be slowed down by a factor of 5 (every 10 ns) before reaching the FPGA, and this is achieved by summing five data points at a time. Then the CFD is calculated as given in Equation 3.4 where each $a(i)$ is now a sum over five data points. A search for the arrival time is started by what is known as the fast filter (FF), which is explained in more detail below, and the FPGA selects the first zero crossing of the CFD after the CFD trace reached a certain threshold. Linear interpolation between the values around the zero crossing is used to give a < 2 ns time stamp accuracy. Since the FPGA is resource limited, the CFD algorithm was implemented using a fixed set of CFD parameters, which were optimized for LaBr detectors by XIA [57]. These parameters are shown in Table 3.1.

CFD Parameter	Value
w	1
B	5
D	5
L	1

Table 3.1: Fixed CFD parameters as implemented in the PIXIE-16

These values, however, may not be optimal for our system given that we use three different detectors to detect the coincidence between high-energy gamma rays (> 1 MeV) and 3.5 MeV alpha particles. Therefore, we first decided to test these parameters with a simple setup consisting of a ^{22}Na source placed between YAP and LaBr, as shown in Figure 3.6.

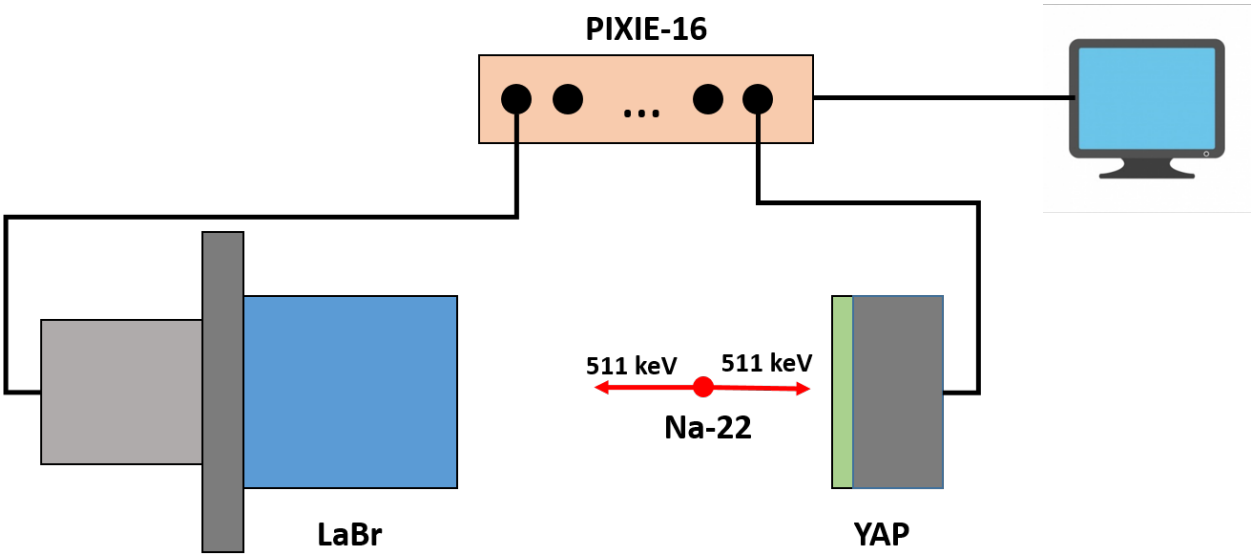

Figure 3.6: Experimental setup used to characterize the time resolution of our system and optimize different CFD parameters.

^{22}Na is a neutron-deficient isotope of sodium that mainly decays by $\beta+$ emission into ^{22}Ne with a half-life of 2.6 years. This decay is accompanied by the emission of a 1.27 MeV gamma ray, which happens during the transition between the 2^+ and 0^+ states in the ^{22}Ne nucleus. The β^+ particle travels a very short distance within the sample until it encounters an electron with which it annihilates emitting in the process two 511 keV gamma rays at 180° from each other. Because these two gamma rays are emitted at the same time, measurements

of the arrival time difference between two detectors can provide information about the time resolution of the system. The source was placed closer to the YAP crystal given that its absolute detection efficiency is lower due to its thickness (1 mm), and traces were saved for subsequent analysis. We then performed our own CFD calculation based on the raw traces. We used Equation 3.4, but changed the parameters w, B, D, and L systematically. The calculation of the CFD time requires four additional parameters known as the fast filter (FF), the fast filter threshold (FFthresh), the CFD threshold (CFDthresh), and the CFD delay (CFDdelay). The FF is a digital trapezoidal filter with adjustable rise time or fast length (FL), flat top or fast gap (FG), and threshold for pulse trigger detection. The equation implemented in the PIXIE-16 for the FF is shown in Equation 3.5. The FFthresh acts on the fast filter trace and it determines if an event is recorded or considered in the coincidence logic. The CFDthresh acts on the CFD trace and is independent of the FFthresh. The reason for having two different thresholds is so that the PIXIE-16 can still process events that fail to clear the CFDthresh. The time of such an event would not be useful to us but the energy information could be. Furthermore, the FF events are used to determine pileup and total count rates. Finally, the CFDdelay shifts the CFD trace with respect to the FF so the FPGA starts looking for a CFD crossing at a time specified by the user.

$$FF(k) = \left(\sum_{i=k-(FL-1)}^{k} a(i) \quad - \sum_{i=k-(2FL+FG-1)}^{k-(FL+FG)} a(i) \right) \tag{3.5}$$

Figure 3.7 shows an example of a 511 keV gamma coincident event between YAP and LaBr. Note that because there are a lot more scintillation photons emitted per unit of energy deposited in the respective crystals, the LaBr trace, its FF, and CFD have less jitter allowing for a more precise time determination.

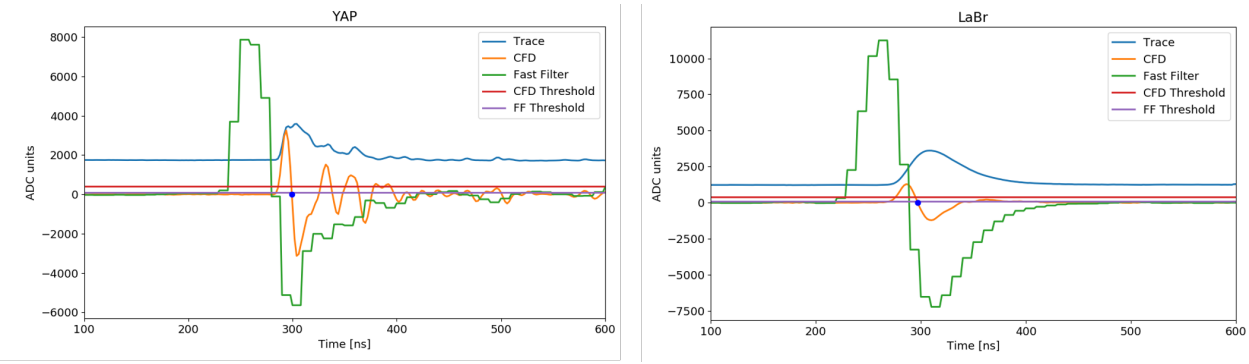

Figure 3.7: Example of a coincident event between YAP and LaBr showing its corresponding CFD time calculation as performed by the PIXIE-16 logic. The blue dot is the value reported as the arrival time.

Performing this exact same calculation for multiple coincident events, we can construct a

histogram of the CFD time differences between YAP and LaBr, as shown in Figure 3.8. For this calculation we used the default PIXIE CFD parameters as shown in Table 3.1, hence convincing ourselves that we understand the internal time calculation as performed by the PIXIE-16. Some experimental parameters are shown in Table 3.2.

Parameter	**LaBr**	**YAP**
PMT voltage	$-700\,\mathrm{V}$	$-1000\,\mathrm{V}$
Preamp voltage	$\pm\ 5\,\mathrm{V}$	$\pm\ 5\,\mathrm{V}$
Amplification	$\times 1$	$\times 10$
No. of traces	77875	77875

Table 3.2: Experimental parameters used to obtain Figure 3.8.

We then used this approach to do a parameter scan to optimize the CFD values for our specific detectors by performing CFD calculations for different combinations of w, B, D, and L. The series of combinations are shown in Table 3.3, and the resulting FWHM values as a function of iteration number is shown in Figure 3.9. The different symbol blocks represent the same value of w for both detectors, and the variations within each block are combinations of the other parameters B, D, and L. A clear pattern can be recognized where the parameter that makes the largest difference is w. The smaller w becomes, the better the time resolution is.

CFD Parameter	**Value**
w	$1, 0.75, 0.5, 0.3125, 0.25$
B	$5, 10$
D	$5, 10$
L	$1, 3$

Table 3.3: CFD parameters used for the optimization procedure shown in Figure 3.9.

However, as the value of w decreases, the CFD trace becomes asymmetric making the amplitude of the positive "hump" increasingly smaller, and hence the CFD threshold has to be set closer to the noise level, which can potentially make the overall calculation unstable for very small values of w. Therefore, we requested a firmware change of w from 1 to 0.3125. The latter value was obtained from the summation $\frac{1}{4} + \frac{1}{16}$. Values of w can only be set to be sums of powers of two due to the binary logic implemented in the FPGA. Ideally, we would also

want to change the other three CFD parameters for each detector in order to achieve better performance. However, this takes more resources for smaller improvements. Therefore, we started by changing the parameter w alone for all detectors, and the results are shown in Figure 3.10. Note that there is a significant improvement in time resolution of approximately 300 ps for the combination YAP-LaBr. The observed time shift of approximately 8 ns between the mean of the distributions is because the CFD trace intersects the threshold earlier in time and hence an earlier time is reported. Nevertheless, this time shift does not affect our measurements given that the quantity of interest is only the time difference between the two radiation quanta.

The previous optimization was performed with a radioactive source and with a simple experimental setup. Nevertheless, the particle energies in the actual API system are higher, i.e. 3.5 MeV for the alpha particle and 1-6 MeV for the associated gamma ray, and hence the number of information carriers produced per interaction is correspondingly higher, which translates into a better time resolution as explained before. An experiment to test these CFD parameters is shown in Chapter 4.

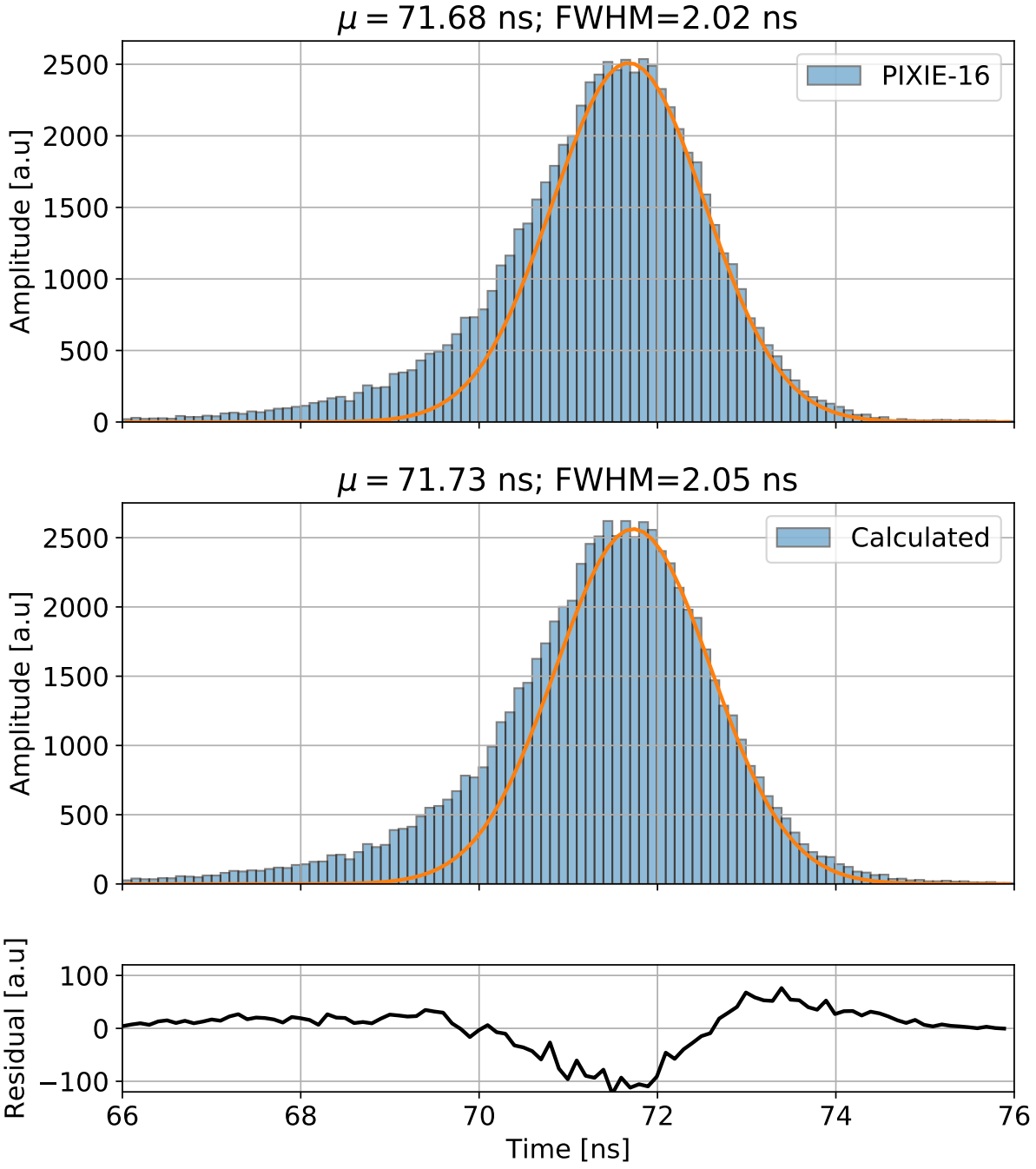

Figure 3.8: Time spectra obtained directly form the PIXIE-16 (top) and calculated (bottom) from raw captured traces. Note the asymmetry in the low energy end. The measured time resolution with default PIXIE-16 parameters of approximately 2 ns would result in a depth resolution of about 10 cm. The fact that the mean of the distribution is around 72 ns comes mainly from the different transit times of the PMT's and cable delays.

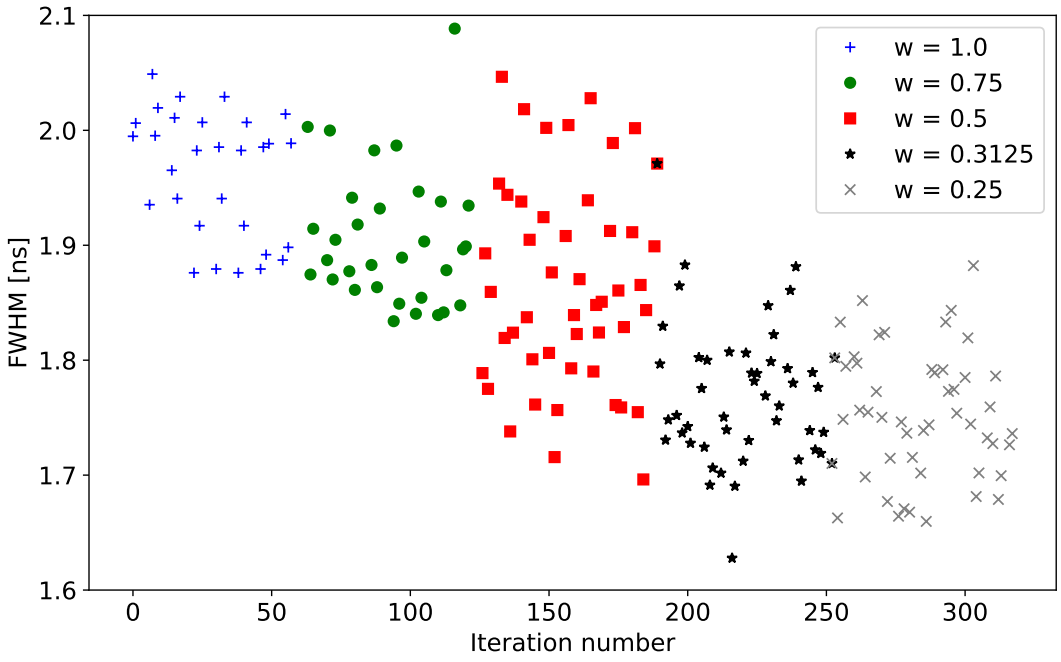

Figure 3.9: Calculated CFD time resolution from raw traces for the experiment depicted in 3.6. Each data point represents a certain combination of CFD parameters, shown in Table 3.3. Values within each symbol block are different combinations of B, D, and L. Note the improved time resolution as w decreases.

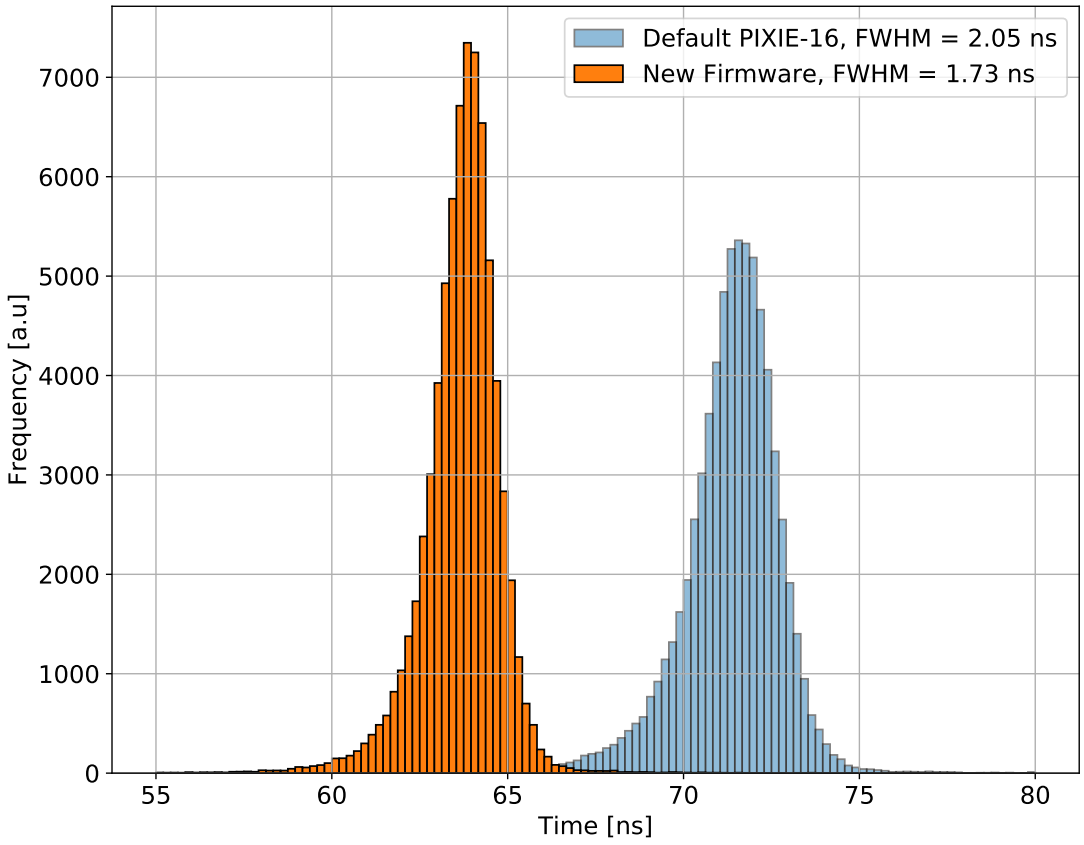

Figure 3.10: CFD calculation for default PIXIE-16 parameters (see Table 3.1) compared to the case where only w is changed from 1 to 0.3125 for the YAP-LaBr combination. Note the time resolution improvement of approximately 300 ps. This time resolution is further improved in the actual API system due to the higher energies of the alpha particle and gamma ray, respectively.

3.3 Modeling of Gamma Detectors with MCNP6

The response of both gamma detectors needs to be modeled in order to predict measurement times, expected gamma lines, and interfering reactions. We decided to use the Monte Carlo N-Particle (MCNP6) transport code [18] for these purposes. One of the many features of MCNP6 is that it allows for neutron-photon coupled simulations together with energy deposition in detectors. However, because MCNP6 works by sampling from probability distributions, some of the nuclear physics is lost in the process. For instance, it does not include nuclear level decay schemes. When a neutron interacts with a nucleus in MCNP6, it randomly samples from probability distributions that contain information about the gamma-ray energy that is emitted and in what proportion. Thus, it cannot account for gammas that come out in coincidence with each other and it does not attempt to conserve the Q-value of the reaction for any particular history. Therefore, the energy deposition tally (F8) fails in neutron-photon coupled calculations. One way to work around this is to split the overall simulation in three separate steps: 1) neutron transport to the sample tallying the gamma rays emitted in its volume, 2) photon transport to the detectors using the photon source obtained in step 1, and 3) energy deposition in the detector volume using experimental data to account for its finite energy resolution. In the following discussion, we present an example that will illustrate the overall process. It consists of a graphite brick of dimensions $14.4 \times 33.2 \times 6$ cm^3 that is irradiated in coincidence mode, as shown in Figure 3.11. Table 3.4 shows a description of the MCNP6 tallies (type of particle scoring events) that are used for these simulations.

Tally Name	Tally Description
F4	Track-length estimate of cell flux
F8	Energy distribution of pulses created in a detector
GEB	Gaussian energy broadening modifier

Table 3.4: MCNP6 tallies and tally modifiers used in the modeling of neutron-induced gamma-ray response on LaBr and NaI. All of these tallies are normalized per source neutron [18].

Neutron Transport Simulation

The neutron transport simulation makes use of the F4 tally in MCNP6, which records the energy-dependent average photon flux over a cell e.g. the carbon brick. At this point, there is no need to be concerned about the units since the spectrum is normalized given that it serves as the probability density function in step 2. We assume a 14.1 MeV monoenergetic

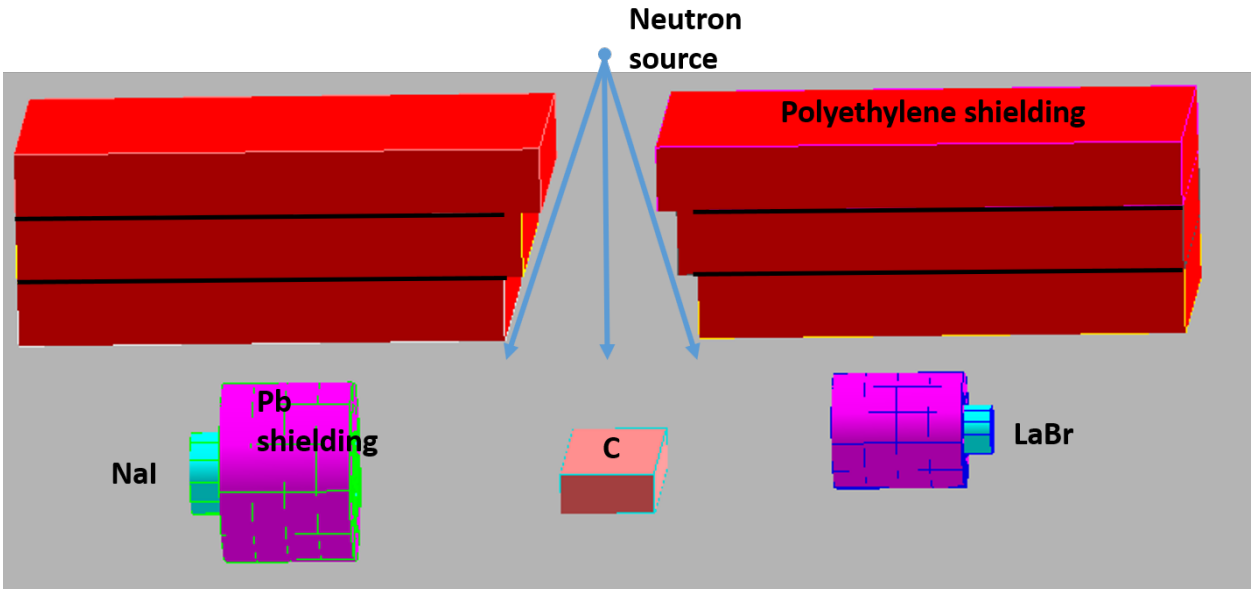

Figure 3.11: MCNP6 geometry used to model the LaBr and NaI detector response. The example shown is for a graphite brick exposed to point source of 14.1 MeV neutrons, which are produced at the origin. The gamma detectors are placed at either side of the graphite brick. They are both shielded by large borated polyethylene blocks and a few centimeters of lead all around.

neutron point source, as shown in Figure 3.11. The results of such simulation for the carbon brick setup is shown in Figure 3.12.

Similar results can be obtained from a point detector (F5 tally) located at the center of the sample. However, F4 accounts for its volume and possible neutron/gamma scattering effects, and therefore is more comprehensive. At this point we have a neutron-induced volumetric photon source originating from the graphite brick.

Photon Transport Simulation and Energy Deposition in Detectors

The discrete probability distribution obtained in step 1 is used as a (gamma) source information card (SI) and source probability card (SP) in a second simulation where the F8 tally is used in order to calculate the energy deposition in both detector crystals. We assume that the gamma rays are emitted isotropically and originate from the sample volume itself. This tally calculates the energy distribution of pulses created in a detector [18]. The standard F8 tally is a pulse-height tally and the energy bins are no longer the energies of scoring events, but rather the energy balance of all events in a history [18]. Figure 3.13 shows the results of this simulation for LaBr.

Note some of the important features in the gamma spectrum that are captured in this sim-

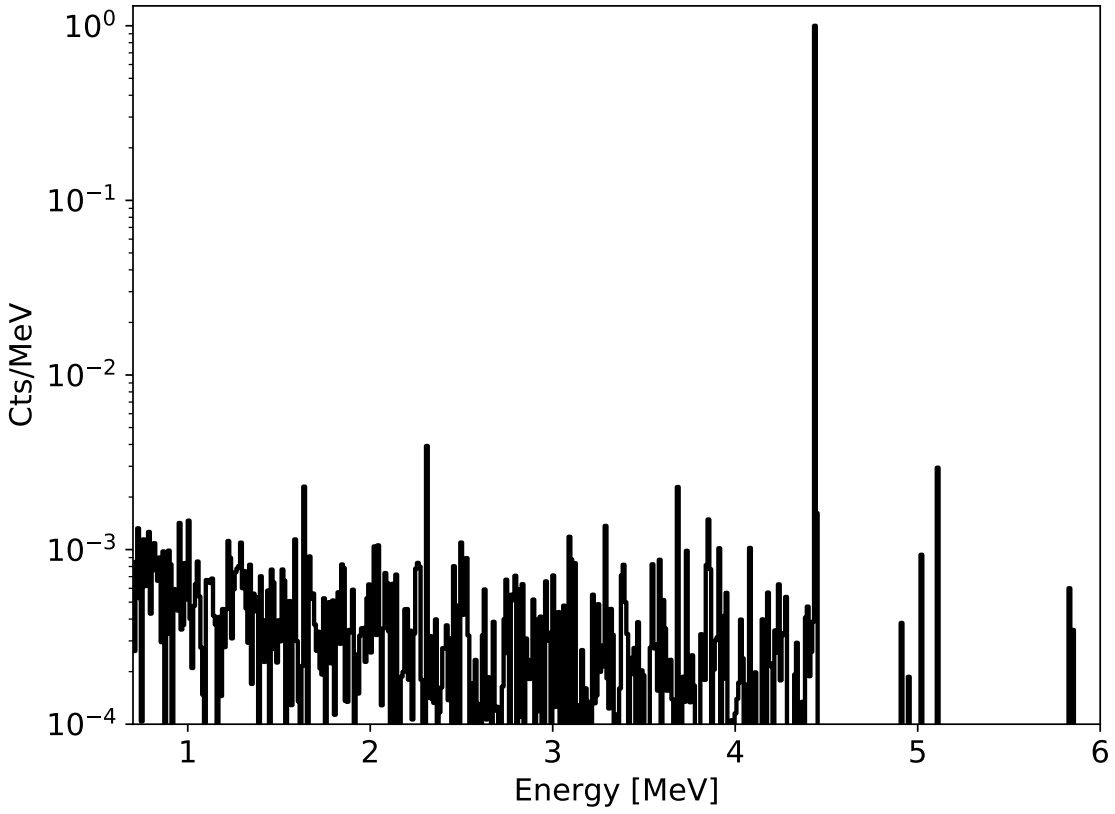

Figure 3.12: MCNP6 results from an F4 tally on a graphite brick used to obtain the gamma probability density function used in subsequent steps of the simulation.

ulation such as the Compton continuum, the single, and the double escape peaks. Nonetheless, the Gaussian broadening of the peaks due to the finite number of charge carriers created per gamma event is not yet calculated in this tally and it requires experimental parameters specific to the detector in question.

Gaussian Energy Broadening for Energy Resolution

In order to account for the finite energy resolution of our detectors, we use the Gaussian Energy Broadening (GEB) tally modifier in MCNP6 which takes in three experimental parameters a, b, and c that conform to our specific detectors. These parameters describe the FWHM of the observed energy broadening according to Equation 3.6. Ideally, the energy resolution should only be proportional to the square root of the gamma energy given that

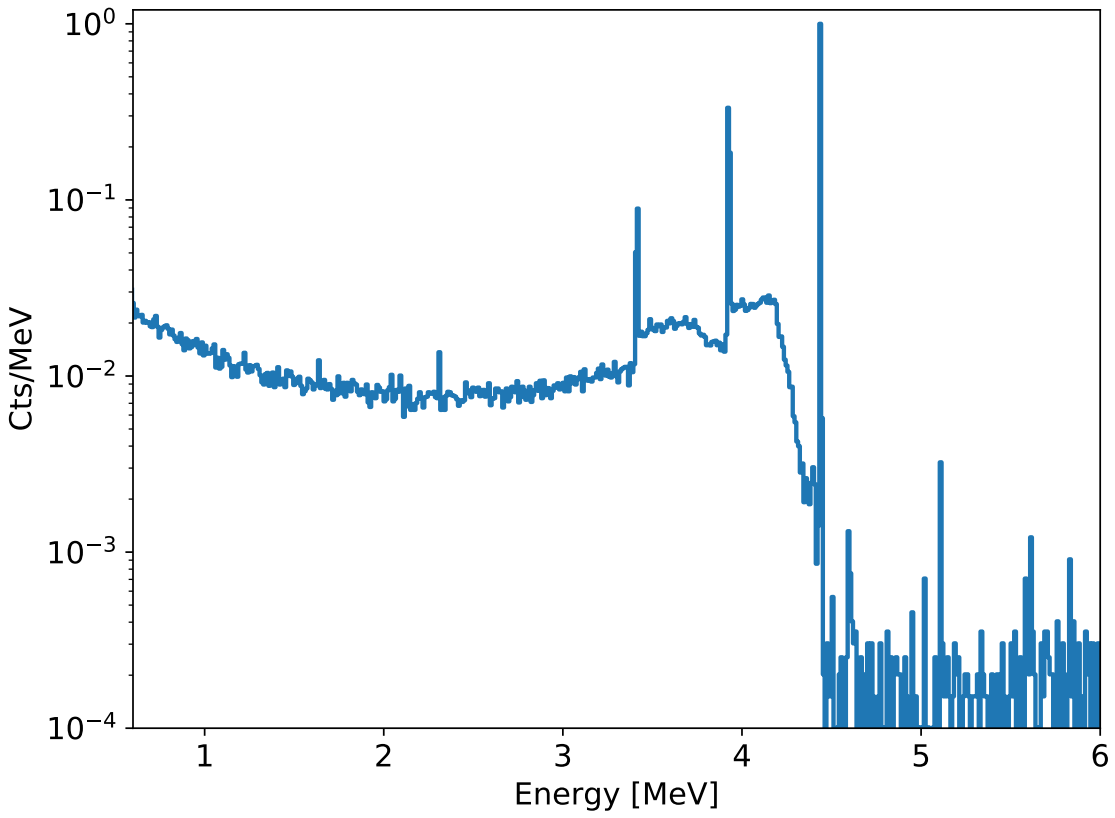

Figure 3.13: MCNP results from an F8 tally (energy deposition) on a LaBr detector. Note in particular the photopeak and their escape peaks which are captured by this tally.

the main contribution to peak broadening comes from the number of information carriers created per gamma event. However, there are other sources detrimental to the energy resolution such as statistical fluctuations in the number of photoelectrons produced in the PMT per gamma event. There are also influences from non-statistical effects that can contribute to peak broadening. Therefore, a more adequate representation is given by Equation 3.6.

$$FWHM = a + b\sqrt{E + cE^2} \tag{3.6}$$

where E is the energy of the gamma ray in units of MeV. The units of a, b, and c are MeV, $\text{MeV}^{1/2}$, and 1/MeV, respectively. The energy scored is sampled form a Gaussian with that FWHM [18].

The FWHM for both gamma detectors are shown in Chapter 5 where a complete gamma-ray spectrum is analyzed. For illustration purposes, we show the MCNP6 results for LaBr

in Figure 3.14.

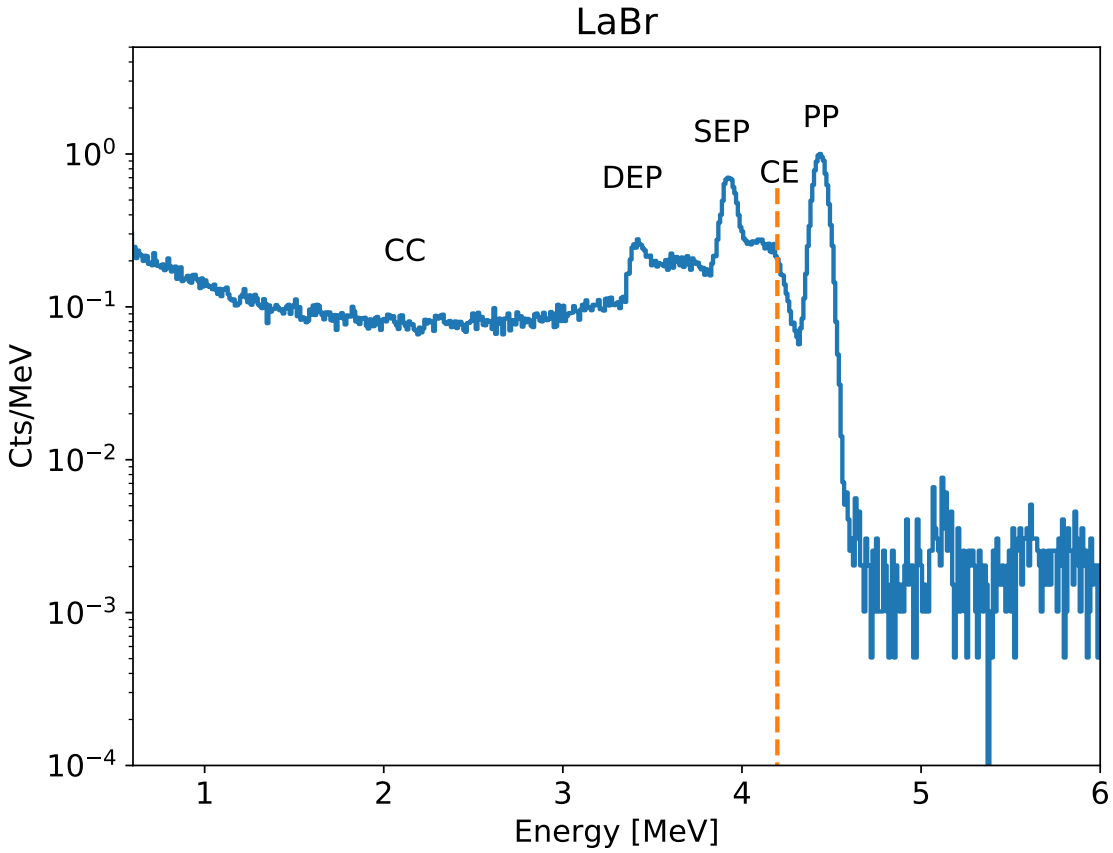

Figure 3.14: MCNP6 simulation result of a 3-inch LaBr detector using an F8 tally for energy deposition in the crystal together with the tally modifier GEB. The main spectral features are labeled as follows: PP: photopeak, CE: Compton edge, SEP: single escape peak, DEP: double escape peak, and CC: Compton continuum.

The experimental parameters used to fit this plot are as follows: $a = 0.020$, $b = 0.044$, and $c = 0.117$. Figure 3.15 summarizes all the three steps of this procedure to model the detector response in MCNP6. As a general rule, MCNP6 simulation results should have an error below 5%. In the previous simulations this was achieved with $1{\times}10^8$ particle histories.

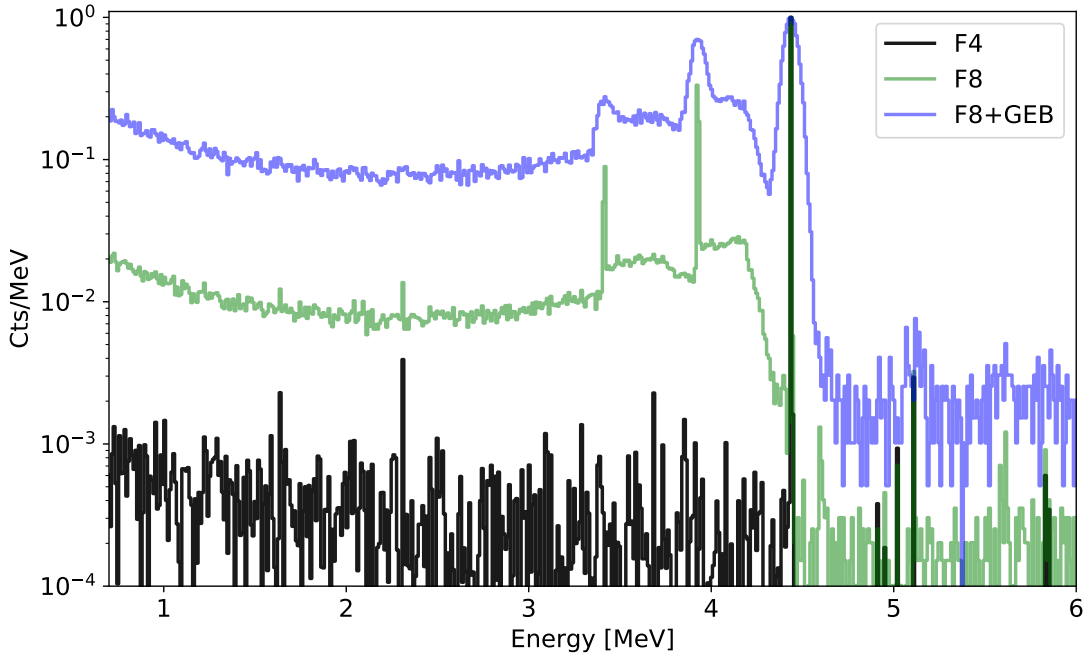

Figure 3.15: The three main steps for an MCNP6 simulation of a 3-inch LaBr detector response to a volumetric gamma source originating from a graphite brick irradiated with 14.1 MeV neutrons. Each of the plots is the result of a specific tally as explained in the text.

3.4 Comparison to Experiments and Sources of Error

In order to validate this preliminary model we performed an experiment where an API spectrum of a graphite brick was obtained. As explained in greater detail in Chapters 4 and 5, API allows for a gamma spectrum specific to a well defined volume. Therefore, a spectrum from graphite alone can be obtained. Figure 3.16 shows the gamma-ray spectrum obtained experimentally given the geometry in Figure 3.11.

Note that there is a remarkable agreement between experimental data and this model except in the Compton continuum region where further adjustments of the experimental parameters a, b, and c should yield a better agreement. Note, however, that these results do not provide information regarding absolute cross-section accuracy because all spectra are normalized. Additionally, some data libraries show a significant difference in cross-section values as a function of angle for 14.1 MeV neutron-induced gamma rays, which requires additional measurements. Nuclear data needs are revisited in Chapter 5.

MCNP6 modeling is particularly important in order to predict the overall performance of the system. We showed that this 3-step procedure can yield very accurate results compared

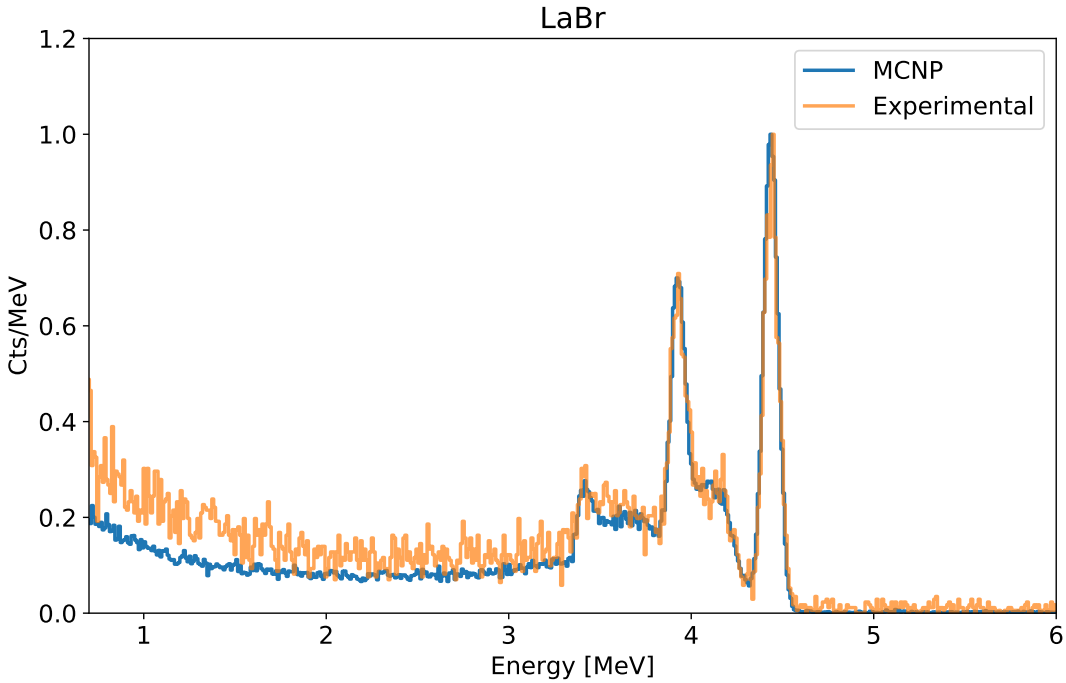

Figure 3.16: Comparison between an MCNP6 simulation and experimental data. For the setup geometry refer to Figure 3.11. Note that the spectrum is normalized to the photopeak, and hence we cannot draw any conclusions regarding gamma-ray intensities at this point.

to experimental measurements. This procedure can be useful to complement the analysis of soil data or other samples with different isotopic composition.

Doppler Broadening Effects on Energy Resolution

One important observation about the gamma spectrum shown in Figure 3.16 is that the energy resolution at 4.4 MeV is $\approx 2\,\%$, which is larger than the expected (1 %) assuming an inverse square root relation between the FWHM and the gamma energy. This estimate was obtained from the FWHM at 0.511 keV, which is 3 % for our detector as shown in Figure 3.2. We believe that one of the main reasons for this discrepancy is that the excited ^{12}C nucleus decays very rapidly (66 fs) and hence can emit a gamma ray while recoiling after interacting with the 14.1 MeV neutron. This process results in an energy shift of the gamma ray that can range from effectively zero to a value given by the maximum energy of the recoiling nucleus. In order to estimate this upper bound, we can use conservation of energy and momentum as shown in Equations 3.7.

$$\begin{aligned} \frac{1}{2}m_n v_i^2 &= \frac{1}{2}m_n v_f^2 + \frac{1}{2}m_A v_A^2 + E_g \\ m_n v_i &= -m_n v_f + m_A v_A \end{aligned} \tag{3.7}$$

where m_n is the neutron mass, v_i the initial neutron speed, v_f the final neutron speed, m_A the mass of the target nucleus, i.e ^{12}C, v_A its recoil velocity, and E_g the gamma ray emitted by the nucleus, i.e 4.439 MeV. solving this system of equations for v_A yields a speed of $v_A = 0.04c$ and the upper bound for the energy shift due to Doppler broadening is therefore $E_s = E_\gamma \frac{v_c}{c} = 180\,\text{keV}$. This value is significant enough to be observed experimentally. The true energy shift is a distribution depending also on scattering angles and detector positions. A more detailed analytical treatment or a simulation is required to obtain a realistic distribution, such as in [6].

Chapter 4

Integrated API System

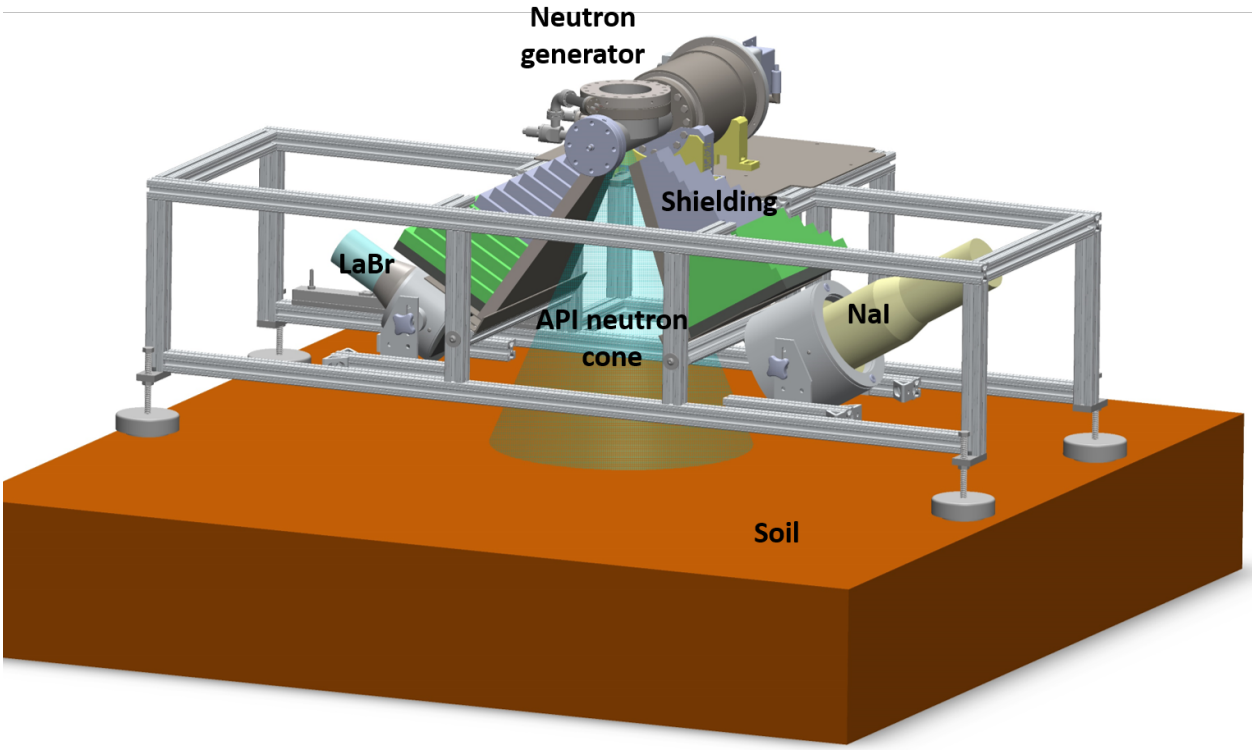

Figure 4.1: CAD rendering of the integrated API system. The photomultiplier tube of the alpha detector (not shown) is placed vertically on the sapphire window held in place by a 6-inch flange shown at the top of the neutron generator head. The API cone of tagged neutrons is also shown as reference.

The API system shown in Figure 4.1 shows the CAD drawing of the integrated system. The main components are shown including the neutron generator, the gamma detector

shielding, both gamma detectors, and the overall arrangement to be used in the field. For relative dimensions between the most relevant components, refer to Figure 1.1. In this chapter, we present the performance of the integrated system and the 3D position resolution to be expected in the field. Additionally, we present the theoretical calculations used for the position reconstruction and for the shielding structure. The latter was specifically designed to reduce the 14.1 MeV neutron flux and induced gammas on the detectors given the space constraints.

4.1 Gamma Detector Shielding

The gamma detectors need to be shielded from the neutron source and from the gamma rays generated in the shielding itself. The most effective way of slowing down 14.1 MeV neutrons is through inelastic scattering as opposed to elastic scattering at lower neutron energies [29]. The reason for this is that a high energy neutron can excite different energy levels in the target nucleus and hence lose energy proportionally. Additionally, the microscopic elastic scattering cross-section drops significantly for neutron energies higher than around 100 keV, as shown in Figure 4.2.

It is worth noting that direct comparison of microscopic cross-sections is not, however, a complete indicator of shielding capabilities in different materials. In turn, the macroscopic cross-section is a more relevant figure of merit given that it accounts for the atomic density of the medium.

In order to quantify and compare the neutron energy loss per collision for both elastic and inelastic scattering, a simple model based on classical mechanics is presented in standard textbooks such as in [29]. Equation 4.1 describes the average neutron energy loss in a single elastic scattering event ($\bar{E_e}$), where E_n is the incident neutron energy and α is given by Equation 4.2.

$$\bar{E_e} = \frac{1-\alpha}{2} E_n \tag{4.1}$$

$$\alpha = \left(\frac{A-1}{A+1}\right)^2 \tag{4.2}$$

Inelastic scattering is more difficult to model because it depends on the available excited states in the target nucleus. In general, inelastic scattered neutrons show up in energy groups centered around the incident neutron energy minus the energy of the excited state that was populated. However, when the neutron energy is sufficiently large so that it is able to populate many levels, the neutron groups cannot be resolved and a continuous spectrum is observed. This spectrum takes a Maxwellian distribution and can be found in standard textbooks such as in [29]. Assuming this situation applies to a certain degree in the case of ^{56}Fe, which is the material of choice for our shielding, we can calculate the average energy loss per collision E_i with Equations 4.3 and 4.4.

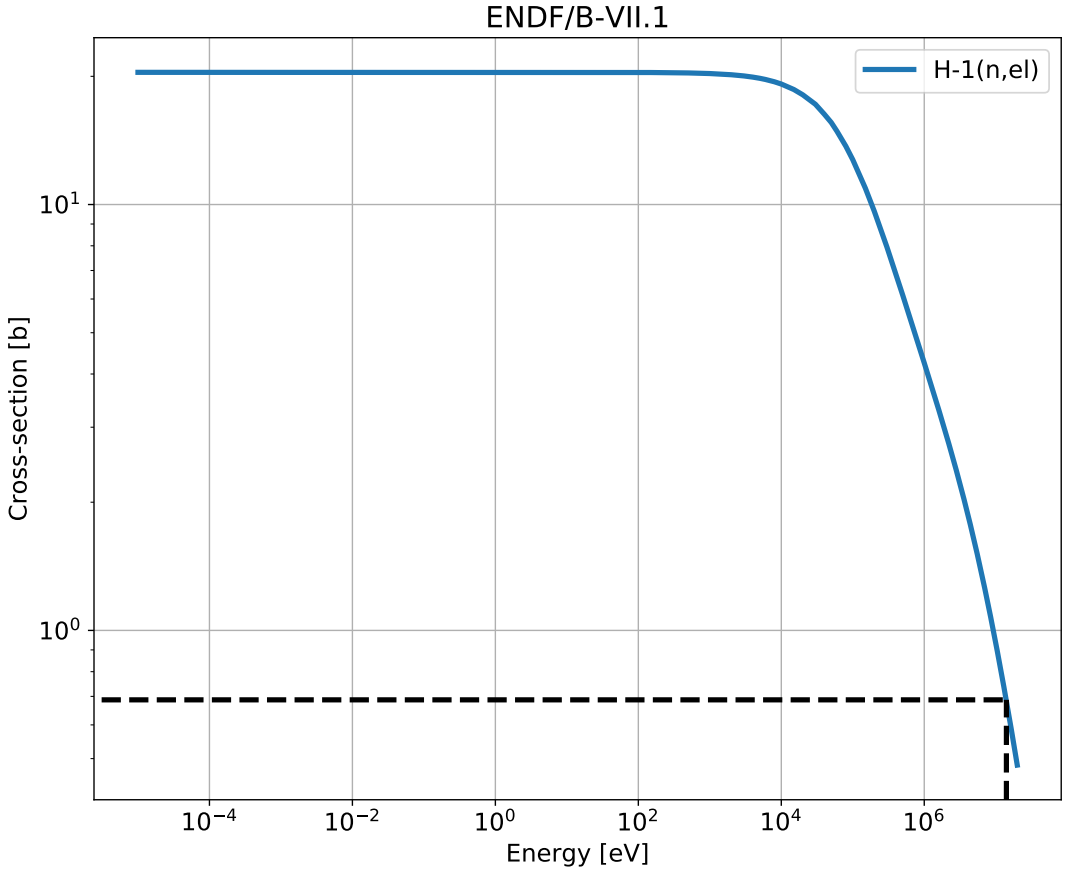

Figure 4.2: Microscopic elastic scattering cross-section taken from [4]. Note how the cross-section drops for higher neutron energies, which reduces the shielding capabilities of hydrogen. The dotted line indicates the 14.1 MeV incident neutron energy.

$$\bar{E}_i = 2T \tag{4.3}$$

$$T = 3.2\sqrt{E_n/A} \tag{4.4}$$

where T is the nuclear temperature (derived from the liquid-drop model) in MeV, and E_n is the incident neutron energy also in MeV. Figure 4.3 shows three curves: the average neutron energy loss per collision by elastic scattering on hydrogen and ^{56}Fe together with the average energy loss per collision by inelastic scattering on ^{56}Fe.

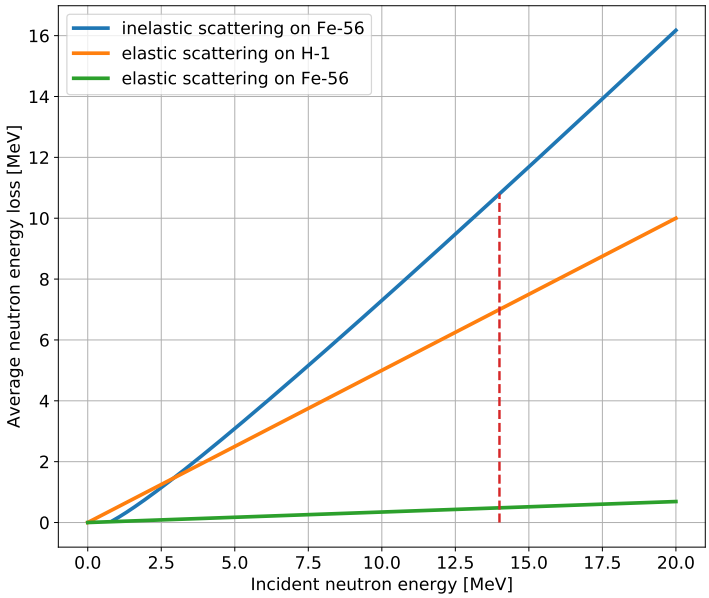

Figure 4.3: Energy loss per collision for elastic scattering on hydrogen/^{56}Fe and inelastic scattering on ^{56}Fe. For incident neutron energies higher than approximately 2.5 MeV, inelastic scattering is more effective for neutron shielding. Also note the energy threshold for inelastic scattering, which is 862 keV for ^{56}Fe corresponding to its first excited state. The dashed line shows the 14.1 MeV energy mark.

Note that for 14.1 MeV neutrons incident on hydrogen (^{1}H), the average neutron energy after a single collision is $\frac{1}{2}E_n = 7$ MeV, but the average neutron energy after a single inelastic scatter on ^{56}Fe is 3.2 MeV. For our purposes, any neutron interaction with the shielding material would attenuate the direct neutron flux, except for (n,xn) reactions that may potentially increase the number of neutrons. This latter reaction is more likely in higher mass nuclei such as lead. Considering all of these factors, intermediate-mass nuclei are preferred for attenuating the direct 14.1 MeV neutron flux. The material of choice because of its availability, relatively high cross-section (around 2 b elastic+inelastic), machinability, etc. is iron, which has been used in the past for this purpose such as in [19], [9], and [55]. Once high energy neutrons slow down to a certain point, the process of elastic scattering takes over and hydrogen is the most effective of all because of its similar mass to that of the neutron, i.e. complete energy transfer is possible. Therefore, borated polyethylene is used as the second layer. The isotopic composition of natural boron constitutes of approximately 20% ^{10}B, which has a significantly high neutron capture cross-section at thermal energies. Upon neutron interaction in the shielding structure, ^{10}B emits low-energy gamma rays of 478 keV (capture), hydrogen emits 2.2 MeV gamma rays, and inelastic scattering on carbon results in a hard 4.4 MeV gamma. Therefore, another layer of high-Z material is needed to

attenuate these gamma rays. Because of the space constraints, we decided to use one inch of Tungsten. The detectors themselves are shielded all around by two inches of lead, as shown in Figure 4.4 (left).

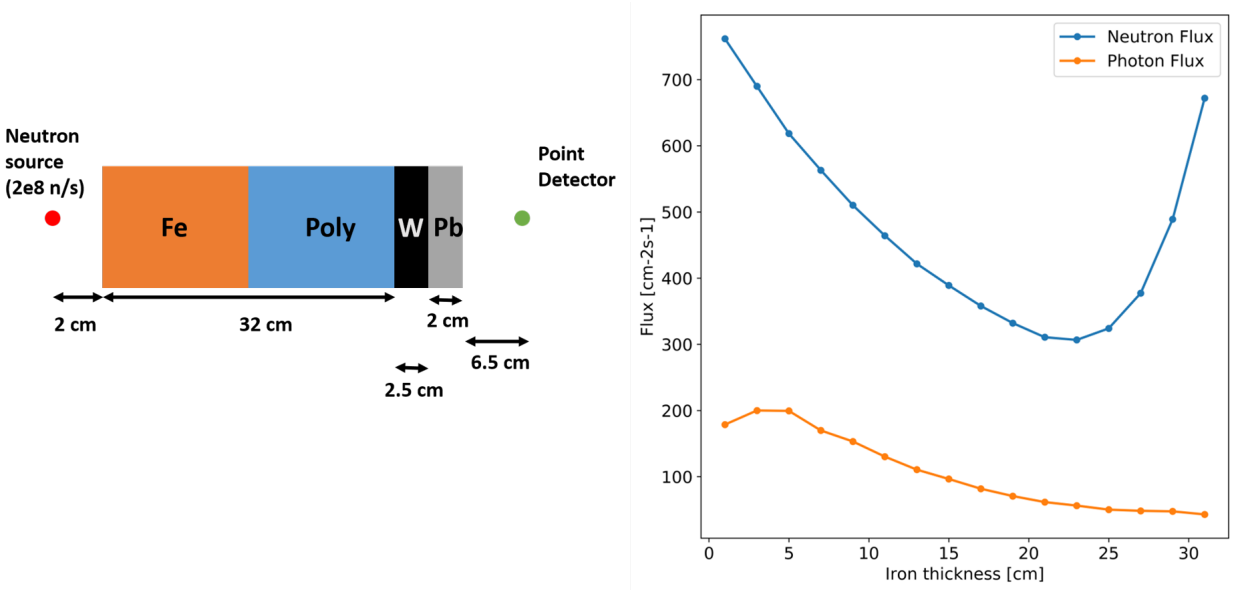

Figure 4.4: Shielding geometry as modeled in MCNP6 (left) and corresponding results (right) for the case of a point neutron source with output equal to 2×10^8 n/s. Note that there is an optimum ^{56}Fe thickness for lower neutron and gamma fluxes at approximately 21 cm.

MCNP6 simulations were performed to optimize the shielding geometry. Specifically, we needed the iron-polyethylene thickness to be optimized. The total space available for the iron-polyethylene shielding structure is 32 cm. Therefore, we varied the thickness of individual components keeping the total thickness constant. The results are shown in Figure 4.4. Note that the efficiency of iron to shield high-energy neutrons start falling off at approximately 21 cm. This value is consistent with the work reported in [19], which improve our confidence in the simulation results. Therefore, we decided on the shielding geometry shown in Figure 4.1. The tapered design (shadow shielding) allows for a reduction of gammas created in the shielding and its overall mass.

4.2 API Timing Considerations

Precise time measurements are required for API in order to determine the neutron interaction depth. Therefore, digital constant fraction discrimination (CFD) is used to obtain the time of arrival information of a pulse and its overall performance is shown in this section. Additionally, we present a brief discussion on the timing logic implemented in the DAQ.

CFD Performance

The CFD parameter optimization outlined in Chapter 3 was performed with a ^{22}Na radioactive check source, i.e two 511 keV gamma rays in coincidence. However, the API system performance is determined by the arrival times of the alpha particle (3.5 MeV) and the neutron-induced gamma ray (0.5 - 6 MeV). The number of photons produced in the YAP crystal per unit of energy is different for either charged particles or gamma rays, and the energy range of interest of the gamma rays to be detected with the LaBr and NaI detectors is greater than 511 keV. Therefore, in order to test that the CFD parameter change $w = 0.3125$ applies equally well to the actual API system, we prepared two other experiments. The first one consisted of two carbon bricks separated from each other by 12 cm with low-density foam, as shown in Figure 4.5a. They were irradiated in coincidence mode for 1800 s with the old firmware ($w = 1$), and then for 1800 s with the new firmware ($w = 0.3125$). The time spectra for both detectors with the two different values for w are shown in Figure 4.6.

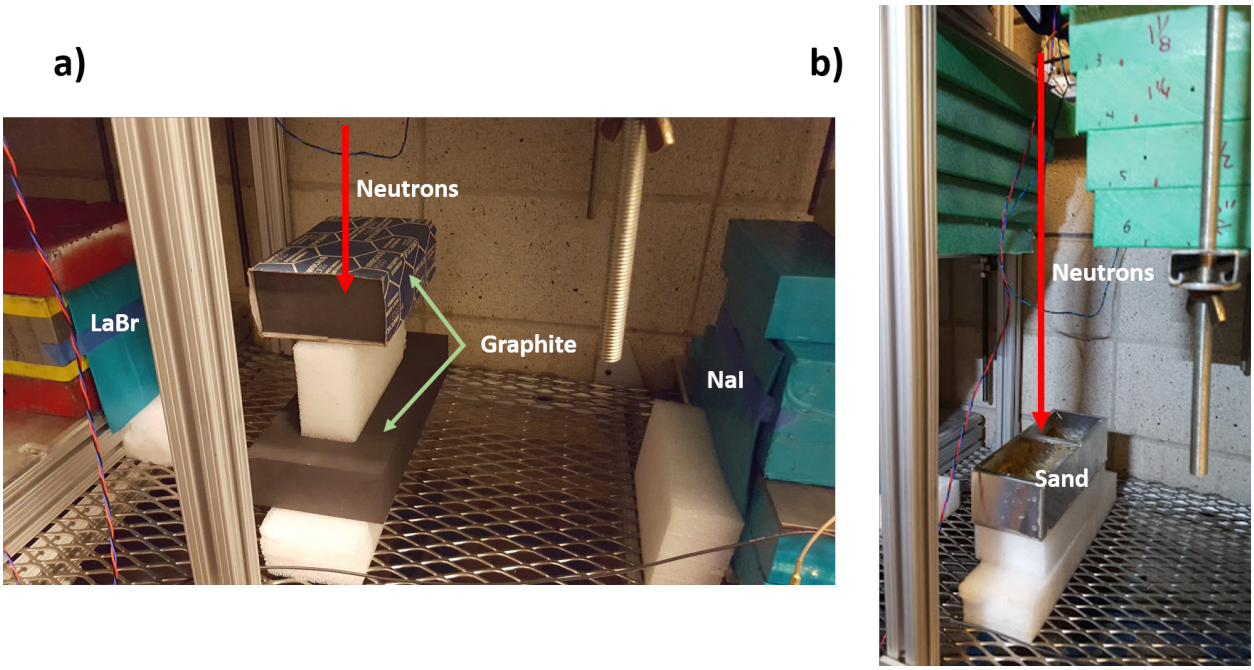

Figure 4.5: Two different experimental setups designed to test the CFD parameter change from $w = 1$ to $w = 0.3125$. a) Shows two large carbon bricks located underneath the neutron generator and stacked 12 cm apart. This setup is also used to test the API reconstruction algorithm in the next section. The top brick is placed approximately 60 cm from the neutron beam spot. b) Two aluminum boxes filled with one inch of wet sand. There are two square lead sheets in front of the gamma detectors to attenuate soft gammas.

As expected, the time resolution is better than the one predicted with the ^{22}Na source. The two left-most peaks correspond to the top and bottom graphite bricks, respectively.

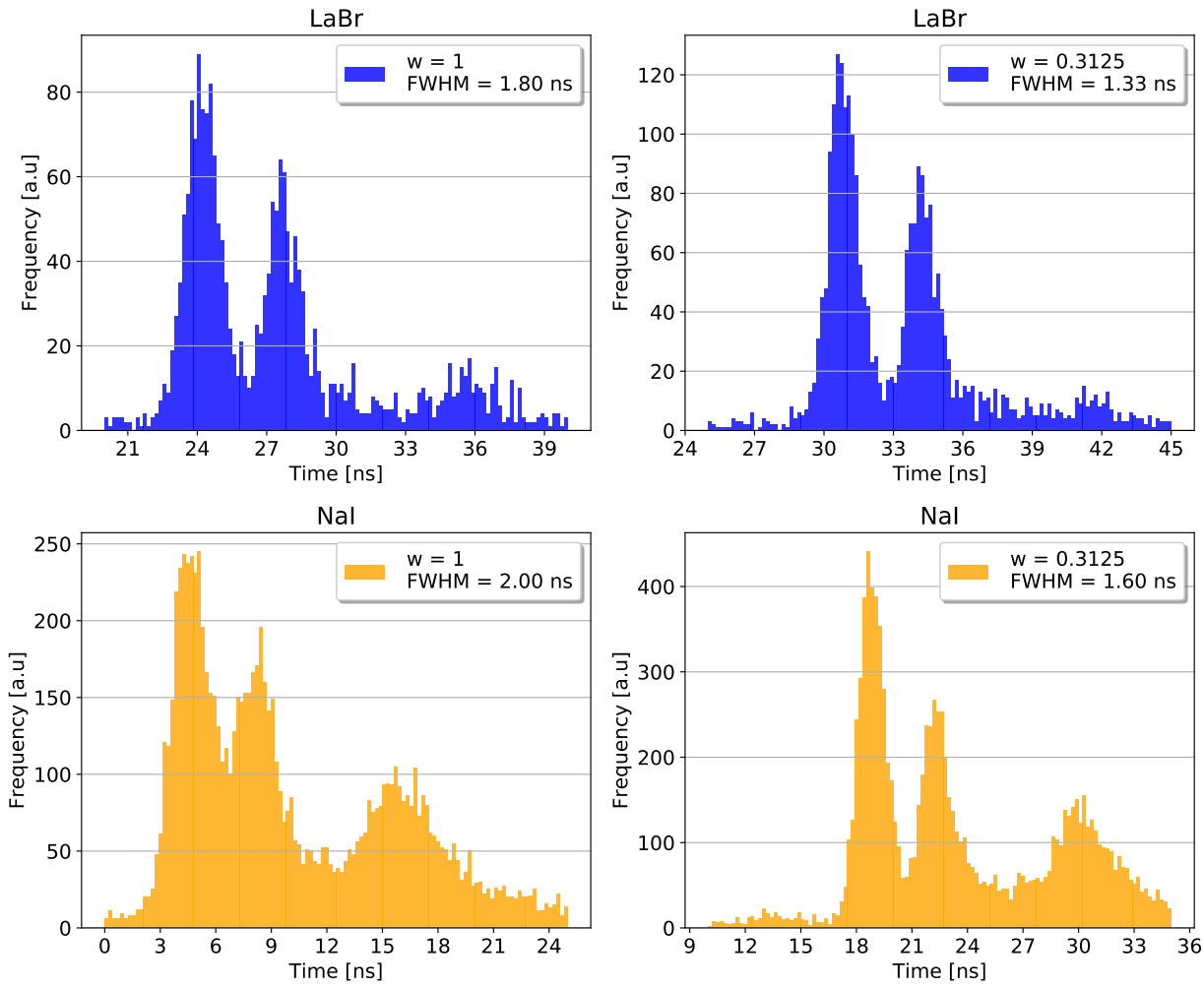

Figure 4.6: API time spectra for the experimental setup shown in Figure 4.5a. Data was taken using two different PIXIE-16 firmware that vary in the CFD parameter w. The two peaks on the left of the spectra correspond to the two graphite bricks, respectively. Note the time resolution improvement for the case of $w = 0.3125$, in particular for the NaI-YAP combination.

The counts on the right of these two peaks are due to the concrete floor and side walls, which contain some carbon. The values of the FWHM shown in the plot do not take into account the errors produced by the thickness of each brick. Therefore, the actual resolution is better than the quoted values. In order to translate this time resolution into actual position resolution, we need to take into account the geometry of the setup, which is shown in the following sections.

The other experiment consisted of two aluminum boxes containing one inch (Z-direction)

of wet sand, as shown in Figure 4.5b. The reason for using sand and aluminum is because the main nuclei present in the samples are ^{27}Al, ^{16}O, and ^{28}Si, which upon inelastic scattering with a 14.1 MeV neutron emit gamma rays with main energies shown in Table 4.1.

Element	**Energy** (MeV)
^{28}Si	1.78
^{27}Al	2.21
^{16}O	2.74
^{28}Si	2.84
^{16}O	3.68
^{16}O	3.85
^{12}C	4.44
^{28}Si	4.50
^{16}O	6.13

Table 4.1: Main 14.1 MeV neutron-induced gamma lines (mostly inleastic) from oxygen, silicon, and aluminum. Note the large dynamic range (energy spread).

These energies span the range of interest for our application, and the benefit of the CFD algorithm is that the resulting time is largely amplitude independent as explained previously. Therefore, if the time resolution improves equally well in this energy range, it would increase our confidence on this parameter change, i.e. $w = 0.3125$. Figure 4.7 shows the time spectra corresponding to this experiment for both LaBr and NaI.

The small peak in between the sand (left) and the floor (right) is due to surrounding structures such as the side walls and shielding. It is present even when the sand sample is taken out. Therefore, for future experiments, we can avoid it by raising the sample by 10 or 15 centimeters, which would shift the peak of interest to the left. The conclusion from these tests is that the firmware change allowed us to improve the time resolution of our system, and we expect a depth resolution between 5 to 10 cm. Further marginal improvements can be obtained by optimizing the other CFD parameters. Other researchers recently suggested that an even larger improvement can be obtained from a different algorithm altogether, such as in [23]. However, it should be kept in mind the possibility of time walk with other methods.

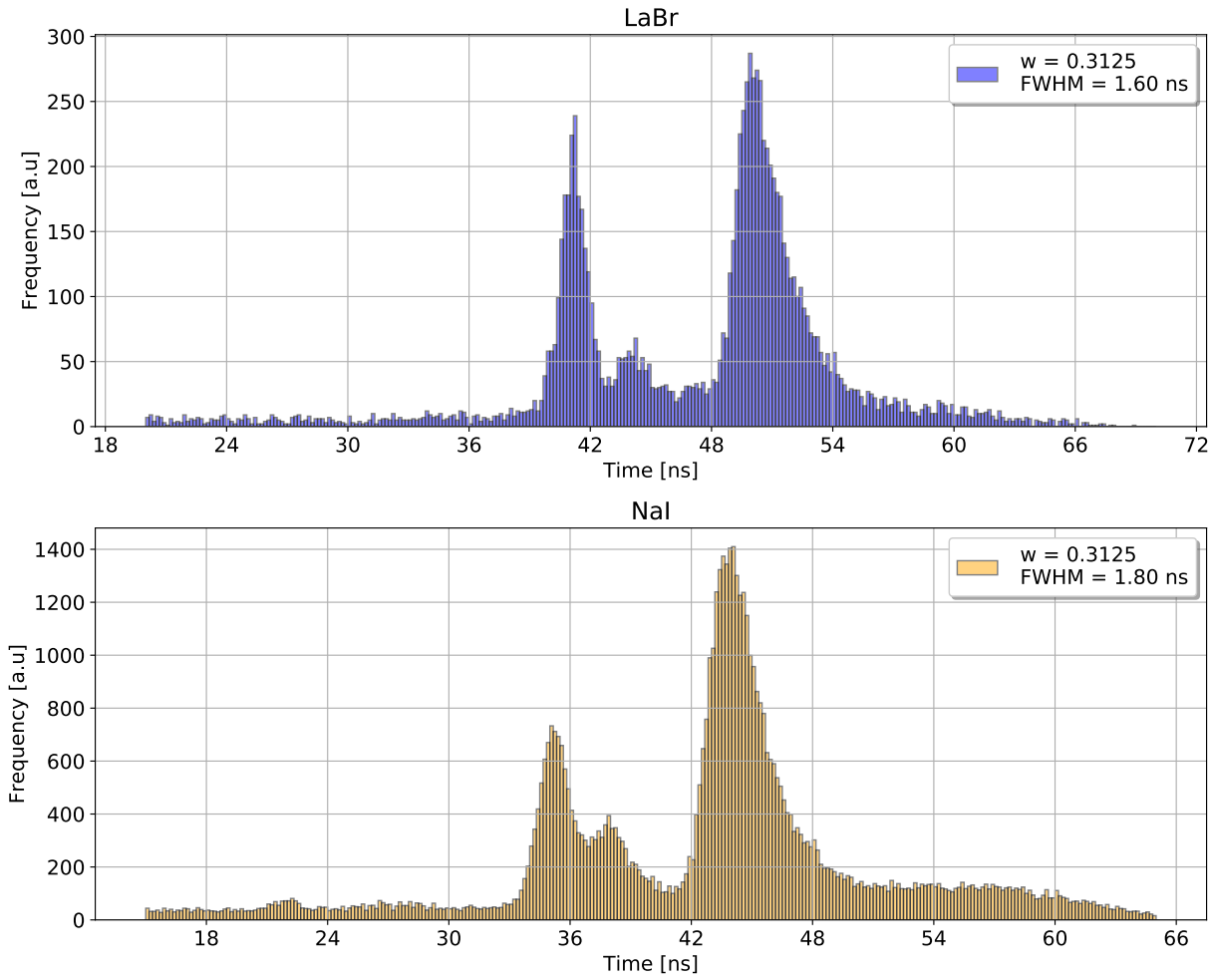

Figure 4.7: API time spectra of the experimental setup shown in Figure 4.5b. Data was taken using the new PIXIE-16 firmware, which uses the CFD parameter $w = 0.3125$. The peak to the left of the spectra correspond to the sand boxes, and the approximate FWHM for this peak is displayed in the legend. These time spectra are obtained by restraining the energies (^{16}O: 6.1 MeV and ^{28}Si: 1.78 MeV) and X-Y position.

API Time Windows

In order to appropriately select the time windows to be implemented in the DAQ logic, it is important to understand the arrival times of the coincident alpha particle and gamma ray in all three detectors. The main factors influencing the recorded time are the flight times of the neutron and alpha particles, and the transit times of the respective photomultiplier tubes.

Figures 4.8 and 4.9 show the results of coincident events between a gamma ray and an

alpha particle for the combination of both YAP-LaBr and YAP-NaI detectors, respectively. The experiment was carried out by irradiating a graphite brick and the data recorded using a digital oscilloscope [39]. However, it is unlikely that the events shown are from this graphite brick.

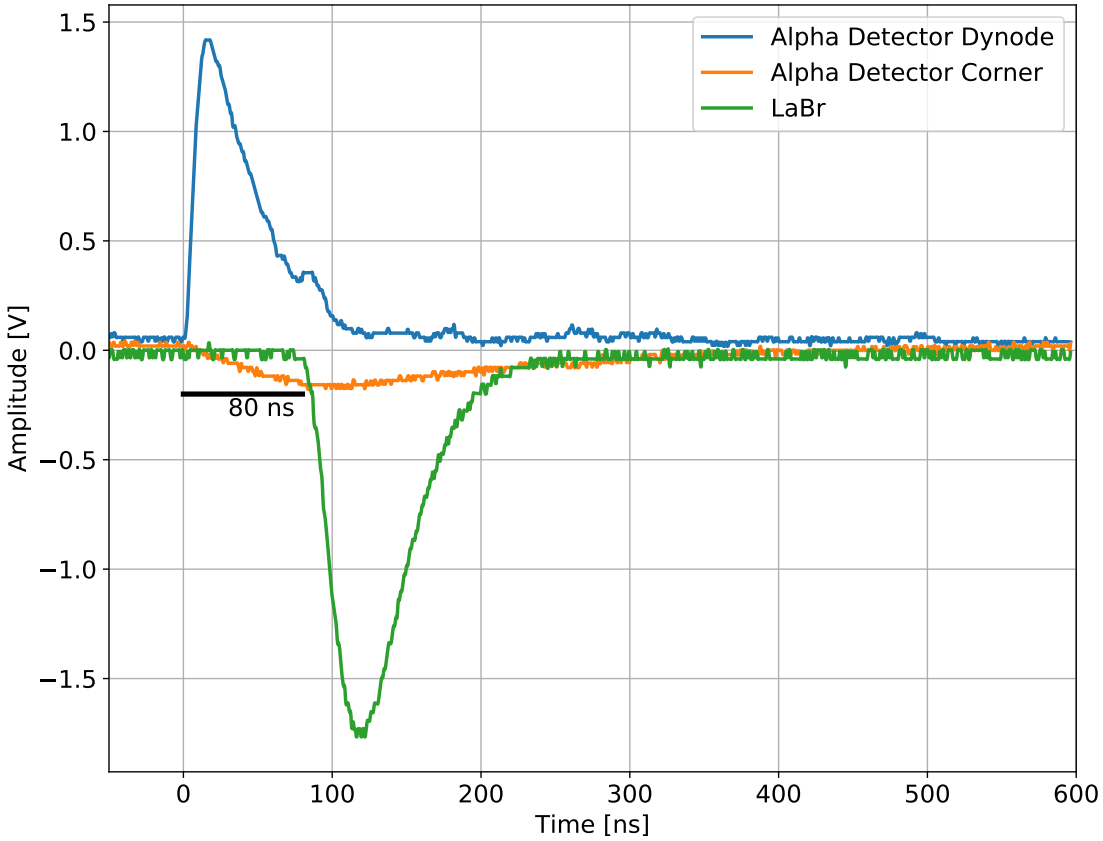

Figure 4.8: Alpha particle and gamma ray coincident event in YAP and LaBr, respectively. Note the time delay between the two signals due to the alpha/neutron time of flight and their PMT transit times. For comparison purposes, also a corner event is plotted.

Note that the PMT of the NaI detector is faster than that of LaBr, which results in a shorter time difference with respect to the alpha signal. The LaBr, NaI, and YAP detectors were operated at $-700\,\mathrm{V}$, $-1670\,\mathrm{V}$, and $-1000\,\mathrm{V}$, respectively. The reason why the polarity of the alpha signal is positive is because it is measured at the last dynode of the PMT which experiences more electrons leaving the dynode than coming in as opposed to the other two detectors. The amplitude gain is chosen so that the signal can take full advantage of the

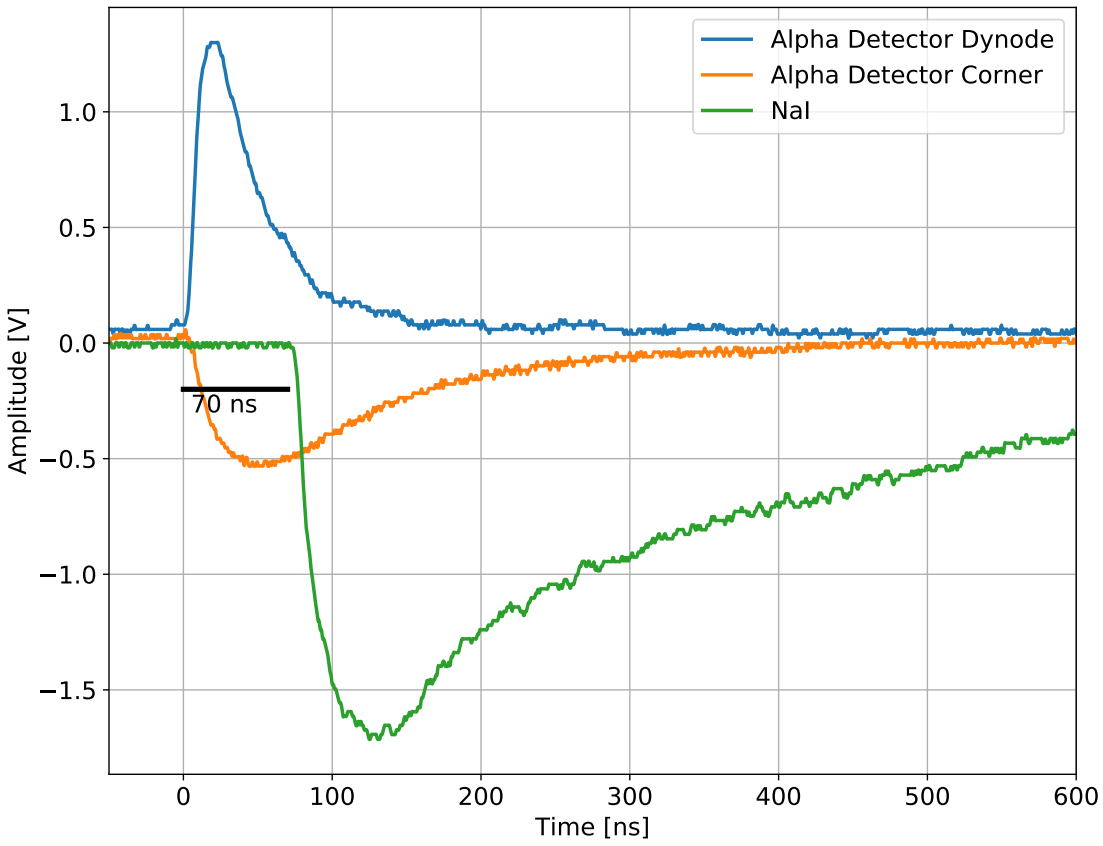

Figure 4.9: Alpha particle and gamma ray coincident event in YAP and NaI, respectively. Note the time delay between the two signals due to the alpha/neutron time of flight and their PMT transit times. For comparison purposes, also a corner event is plotted.

dynamic range of the DAQ which allows for a signal with a maximum of 2 V at its input stage [57]. The information presented above serves to optimize the time windows in our DAQ.

4.3 Position Reconstruction

The pre-processed raw data obtained from the DAQ in coincidence mode is in the format shown in Table 4.2. This information is used in order to reconstruct the 3D location of interaction following a neutron-induced inelastic scattering gamma ray.

Particle	Reported value
Alpha	CFD time
Gamma 1	CFD time, energy
Gamma 2	CFD time, energy
Alpha	corner 1 energy
Alpha	corner 2 energy
Alpha	corner 3 energy
Alpha	corner 4 energy

Table 4.2: Pre-processed data obtained from the DAQ (PIXIE-16). The Alpha CFD time signal comes from the penultimate dynode of the photomultiplier tube. For every coincident event, there is a total of 7 reported values assuming no gamma-gamma coincidence.

The (x_0, y_0) position on the YAP crystal of the alpha detector is calculated from the 4-corner energies as explained in Chapter 2. These coordinate points are used to project down the neutron travel path. Figure 4.10 shows how the scattering location (x,y,z) reconstruction is calculated based on simple vector algebra.

The center of the active area of the YAP crystal with equal sides of length $a = 4.8\,\text{cm}$ is taken to be the origin (0,0,0), the interaction point of the alpha particle in the crystal is $(x_0, y_0, 0)$, the neutron (point) source is located $z_t = 6\,\text{cm}$ from the center of the face of the YAP, the center of the photocathode of the gamma detector is located at (x_1, y_1, z_1), and the scattering location to be calculated is at (x, y, z). The unit vector $\vec{u}$, shown in Equation 4.5 is used to determine the direction of the associated neutron.

$$\begin{aligned} \vec{a} &= \langle -x_0, -y_0, z_t \rangle \\ \vec{u} &= \frac{\vec{a}}{\mid \vec{a} \mid} \end{aligned} \tag{4.5}$$

With this unit vector, the vector $\mid \vec{n} \mid$ can be calculated as shown in Equation 4.6.

$$\vec{n} = \langle x, y, z - z_t \rangle = \vec{u} \mid \vec{n} \mid \tag{4.6}$$

In order to calculate $\mid \vec{n} \mid$, we use the known speed of the alpha, neutron, and gamma ray together with the recorded time (dt). Equation 4.7 shows the relation between dt, the travel time of the neutron t_n, the gamma ray t_g, and the alpha particle t_a.

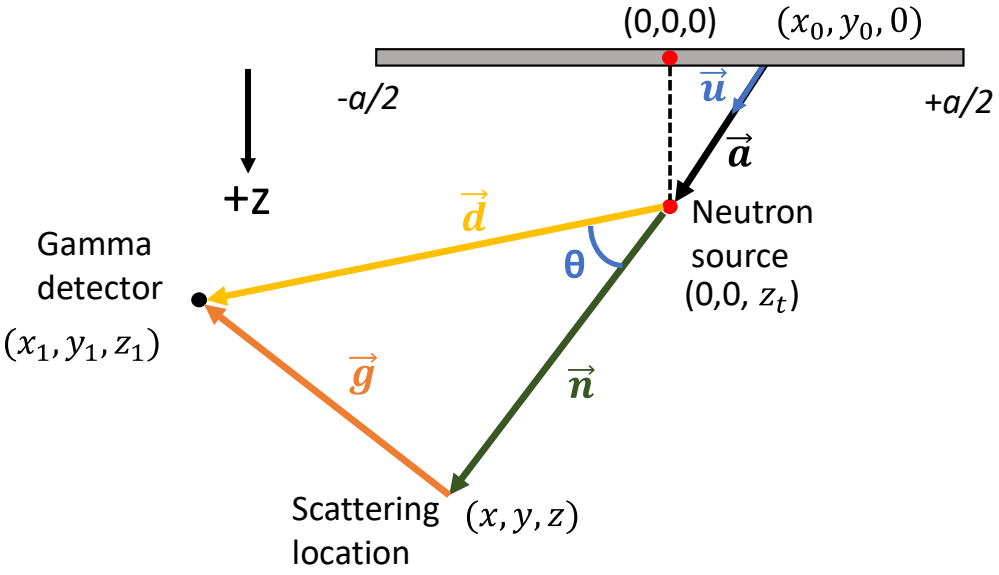

Figure 4.10: Representation of the code output

$$\begin{aligned} dt &= t_n + t_g - t_a \\ dt + t_a &= \frac{|\,\vec{n}\,|}{v_n} + \frac{|\,\vec{g}\,|}{c} \\ |\,\vec{g}\,| &= \left(dt_a - \frac{|\,\vec{n}\,|}{v_n}\right)c \end{aligned} \tag{4.7}$$

where v_n is the speed of the neutron and c the speed of light. Because dt and ta are known, we combine both of these terms into a single one $dt_a = dt + t_a$ to simplify subsequent calculations. Additionally, $\vec{d}$ is also known, so we can use the law of cosines as follows.

$$|\,\vec{g}\,|^2 = |\,\vec{d}\,|^2 + |\,\vec{n}\,|^2 - 2\,|\,\vec{d}\,||\,\vec{n}\,|\cos\theta \tag{4.8}$$

The angle θ can be obtained from the dot product between the vectors $\vec{u}$ and $\vec{d}$, as follows:

$$\begin{aligned} \vec{u}\cdot\vec{d} &= |\,\vec{u}\,||\,\vec{d}\,|\,cos(\theta) \\ \langle u_x, u_y, u_z\rangle \cdot \langle d_x, d_y, d_z\rangle &= (1)\,|\,\vec{d}\,|\,cos(\theta) \\ cos(\theta) &= \frac{u_x x_1 + u_y y_1 + u_z z_1}{|\,\vec{d}\,|} \end{aligned} \tag{4.9}$$

After combining Equations 4.7 and 4.8, we obtain a quadratic equation of the form:

$$\mid \vec{n} \mid = \frac{-b \pm \sqrt{b^2 - 4ac}}{2a} \tag{4.10}$$

where

$$\begin{aligned} a &= 1 - \frac{c^2}{v_n^2} \\ b &= 2dt_a \frac{c^2}{v_n} - 2 \mid \vec{d} \mid \cos\theta \\ c &= \mid \vec{d} \mid^2 - c^2 dt_a^2 \end{aligned}$$

and based on our choice of coordinate systems, we take the negative value of the square root. We can now use Equations 4.5 and 4.6 to obtain the coordinates of interaction as follows:

$$\begin{cases} x &= \frac{-x_0}{|\vec{a}|} \mid \vec{n} \mid \\ y &= \frac{-y_0}{|\vec{a}|} \mid \vec{n} \mid \\ z &= \frac{z_t}{|\vec{a}|} \mid \vec{n} \mid + z_t \end{cases}$$

Note that the main assumptions in this reconstruction algorithm are that the neutrons are emitted from a point source, the neutron and associated alpha are emitted exactly 180° from each other in the lab system, and the position of the gamma detector is a point in space. We will later consider how these assumptions contribute to the overall error.

In order to test this algorithm, an experiment was carried out where two thick graphite bricks were placed on top of each other separated by 12 cm with low-density foam, as shown in Figure 4.5a.

The neutron generator was operated at 50 kV ($\approx 5 \times 10^6$ n/s) and data was acquired for 113 minutes in coincidence mode. Figure 4.11 shows the resulting time *dt* and reconstructed Z histograms where the two carbon peaks are labeled. This histogram was created by selecting only the carbon peak (4.4 MeV) in the gamma spectrum and constraining the X-Y position around the carbon bricks. However, there are no constraints in the Z direction, hence the background peaks from the floor and other structural materials underneath are also visible.

Note that the percent resolution improves somewhat when going from *dt* to Z because when calculating Z, we include more available information based on the known geometry and travel times of the alpha, neutron, and gamma ray, respectively. The Z distribution was adjusted by offsetting the *dt* distribution by 11 ns due to internal time delays, particularly from the electron transit times of the PMTs. Different 2D projections for this data set are shown in Figure 4.12.

The results presented above already provide an idea about the overall system resolution, which is in the order of a few centimeters. A more precise determination of the resolution is presented in the next section.

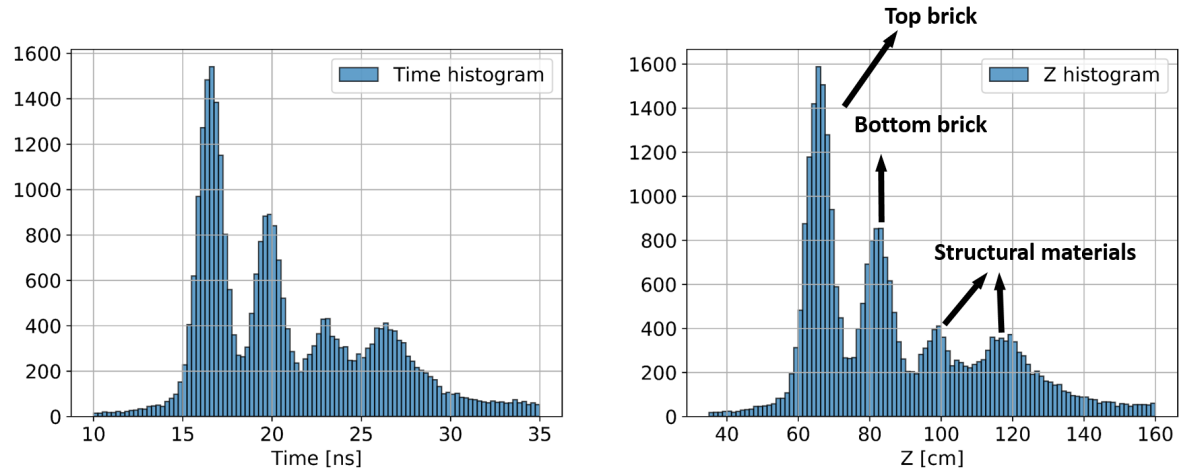

Figure 4.11: Time and Z histograms for the setup shown in Figure 4.5a, as detected with the LaBr detector. Because of time delays mainly from the PMTs, the Z histogram was adjusted by offsetting the *dt* distribution by 11 ns.

Another important feature of the API technique is that one can select a narrow region of space and obtain its gamma spectrum, which is largely free of unwanted background (either natural or from surrounding structural materials). Therefore, the spectroscopic analysis and efficiency calibration are greatly simplified. For instance, the gamma spectrum shown in Figure 4.13 is the result of constraining the time and X-Y to focus on the small graphite brick for the experiment presented above.

Notice how clean the gamma spectrum is for this particular example. The photopeak, single, and double escape peaks can be clearly observed together with their associated Compton continuum. The experiment above is better visualized in 3D. Therefore a cloud image in Mayavi [41] was produced, as shown in Figure 4.14. The 3D plot can be very useful when analyzing preliminary data in order to look for asymmetries and irregularities in the data.

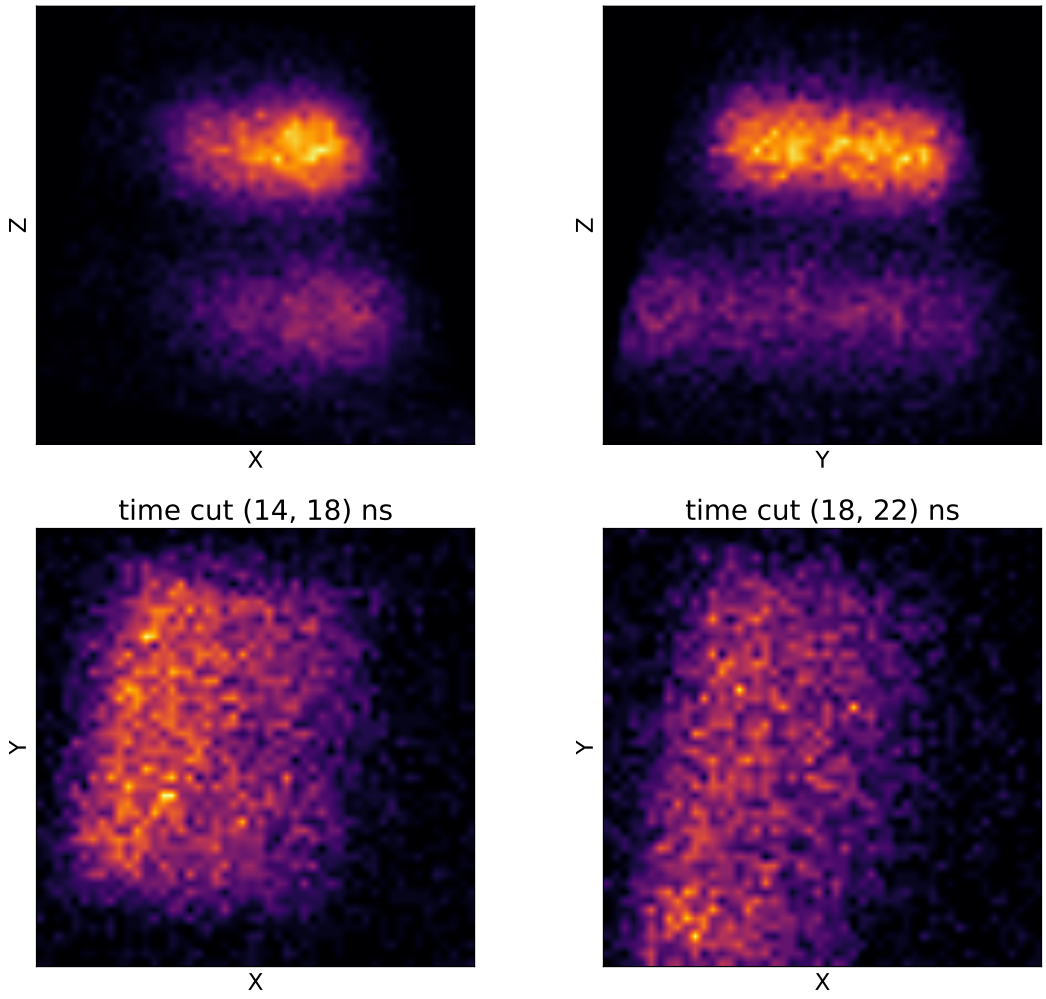

Figure 4.12: 2D projections of the setup shown in Figure 4.5a for LaBr. The X-Y projections are slightly rotated because the YAP crystal is also rotated by the same angle. The relative sizes between the two graphite bricks can be observed.

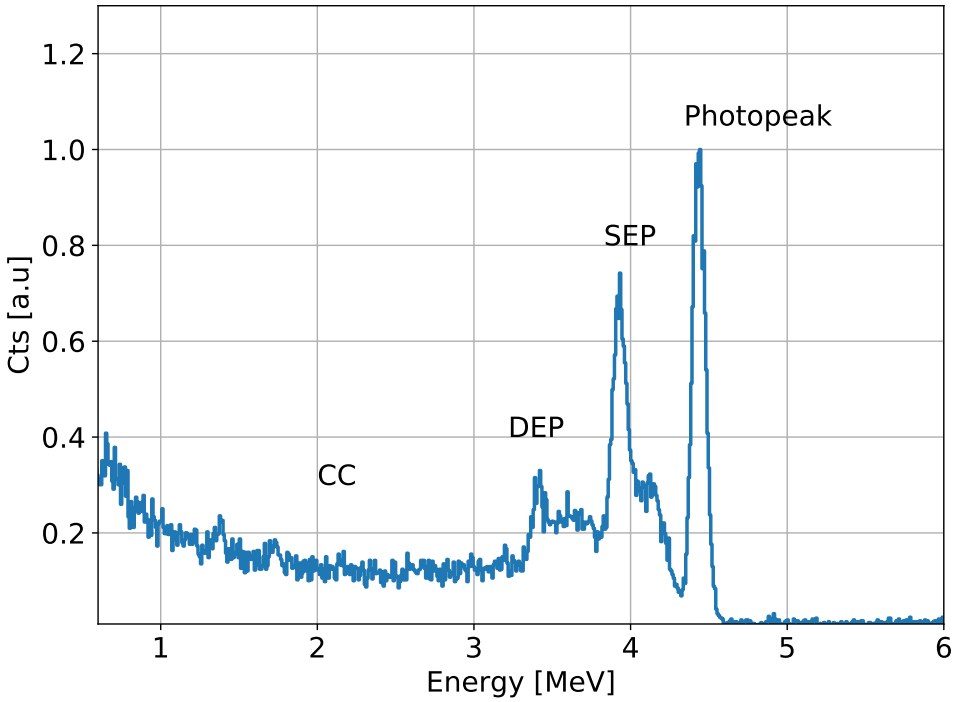

Figure 4.13: API energy spectrum (LaBr) corresponding to the experiment shown in Figure 4.12. This spectrum is obtained by constraining the analysis on the graphite bricks, hence the very clean energy spectrum corresponding to ^{12}C alone, showing an important feature of the API technique, which is its ability to focus on a small volume. The photopeak, single escape peak (SEP), double escape peak (DEP), and the Compton continuum (CC) are shown.

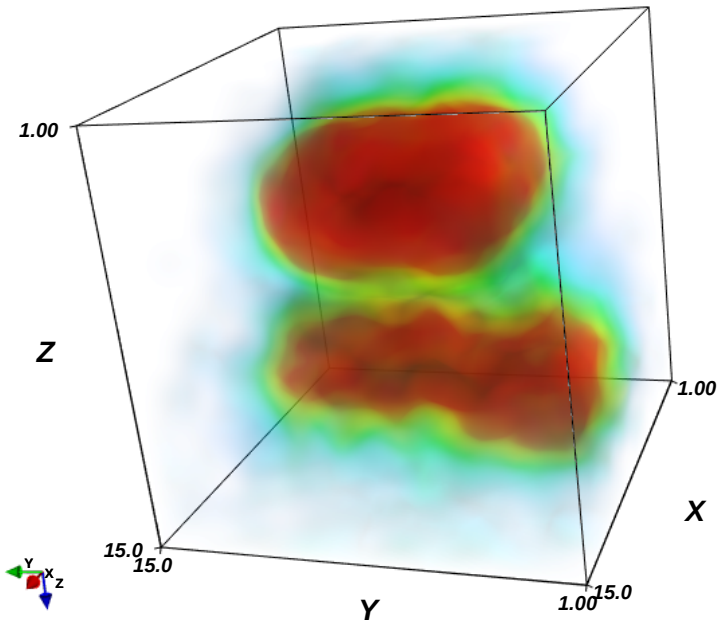

Figure 4.14: 3D representation of two graphite bricks stacked in Z and separated by 12 cm. The units on the axes are arbitrary. The image was obtained with the Python package Mayavi [41].

4.4 Position Resolution Measurements

The system position resolution was measured with graphite samples in two different configurations: 1) two thin (1 cm) slabs stacked in Z by increasingly smaller distances in order to measure the depth resolution, as shown in Figure 4.15a and 2) two thick (6 cm) graphite bricks placed next to each other (X-Y plane) and their distance varied along the Y dimension, as shown in Figure 4.15b. The neutron generator was operated at 50 kV ($\approx 5 \times 10^6$ n/s).

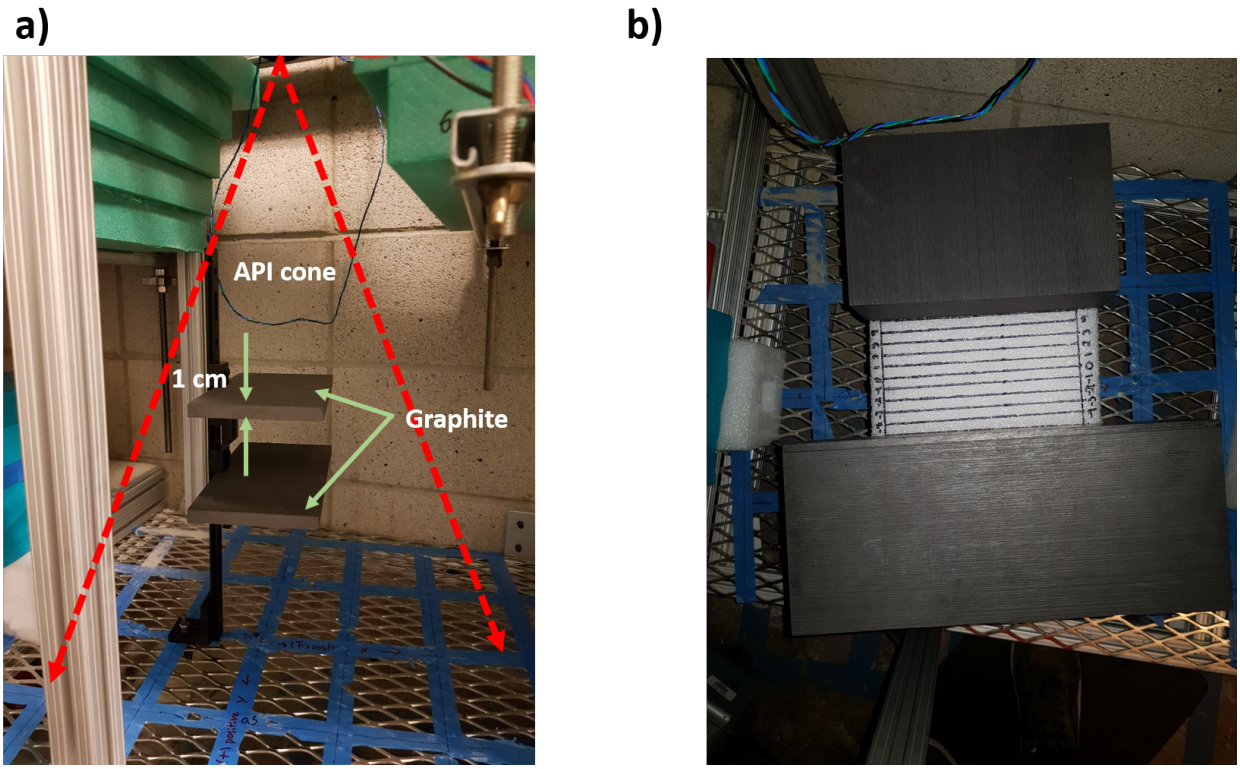

Figure 4.15: Experimental setup used to characterize the system a) depth resolution using thin (1 cm) graphite slabs, and b) X-Y resolution using thick (6 cm) graphite bricks.

System Depth Resolution

Figure 4.16 shows the experimental results (LaBr) for three different cases where the top graphite slab was brought closer to the bottom one starting at 16 cm, then 8 cm, and finally, 6 cm. Figure 4.17 shows the same setup but for the NaI detector. The data was processed by selecting events of 4.4 MeV gamma energy together with its single escape peak and by

selecting only the area surrounding the graphite in the X-Y plane. The Z coordinate was calculated by the method outlined above.

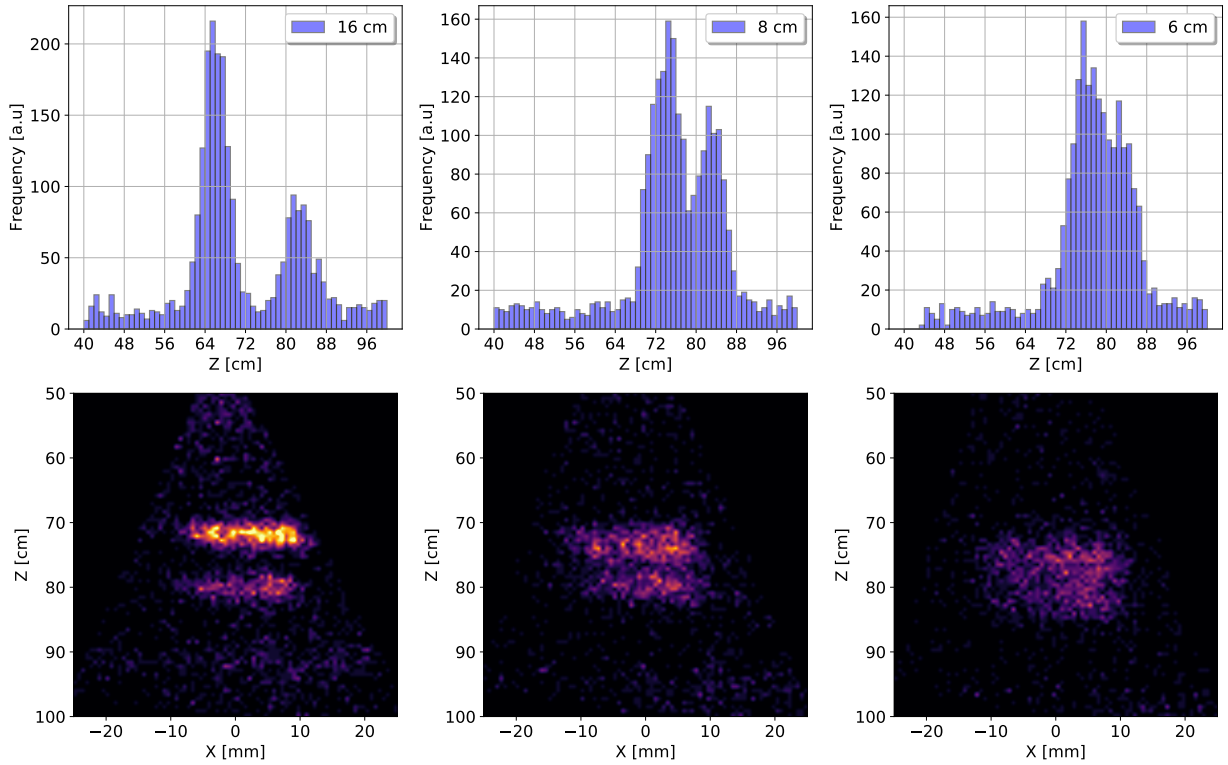

Figure 4.16: LaBr experimental results for the depth resolution measurements with two thin graphite slabs with varying distances among them. Note that at 16 cm separation, the two slabs are clearly separated. The intensity maps also show the top slab being exposed to a higher neutron flux as expected. The system resolution is somewhere between 6 and 8 cm as defined where the two peaks start touching at their FWHM.

Given the above experimental results and the somewhat optimized CFD algorithm, the system depth resolution is 7 ± 1 cm for YAP-LaBr and 8 ± 1 cm for YAP-NaI.

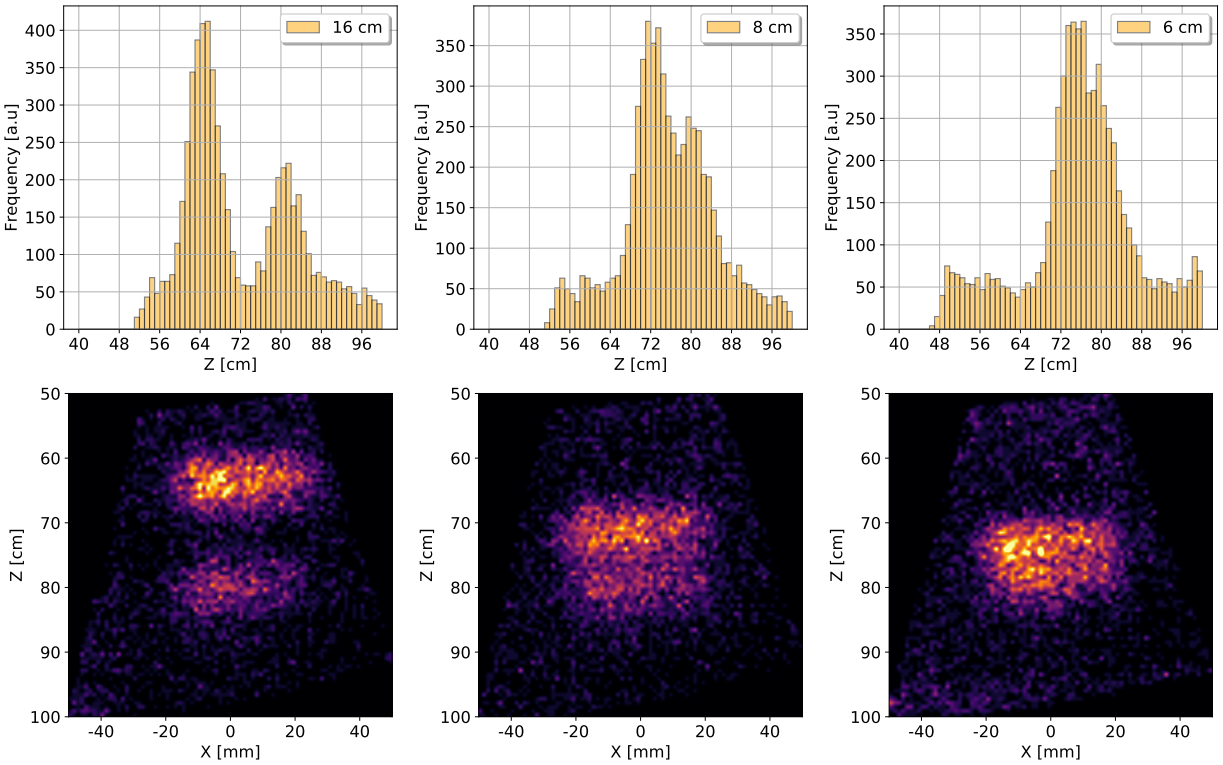

Figure 4.17: NaI experimental results for the depth resolution measurements with two thin graphite slabs with varying distances among them. Note that at 16 cm separation, the two slabs are clearly separated. The intensity maps also show the top slab being exposed to a higher neutron flux as expected. The system resolution is somewhere between 7 and 8 cm as defined where the two peaks start touching at their FWHM.

System X-Y Resolution

The system X-Y resolution was measured in a systematic way with the arrangement shown in Figure 4.15b where two thick graphite bricks were placed side by side separated initially by 10 cm. The blocks were then brought together one centimeter at a time until they could no longer be resolved as defined when the peaks start touching at their FWHM. Figure 4.18 shows the results of a representative set of these measurements

Even though these measurements were performed along a single axis, we expect the resolution to be the same along the other axis too as there is no fundamental difference in terms of the readout algorithm. The results presented are for the YAP-LaBr combination. However, similar results were obtained with YAP-NaI.

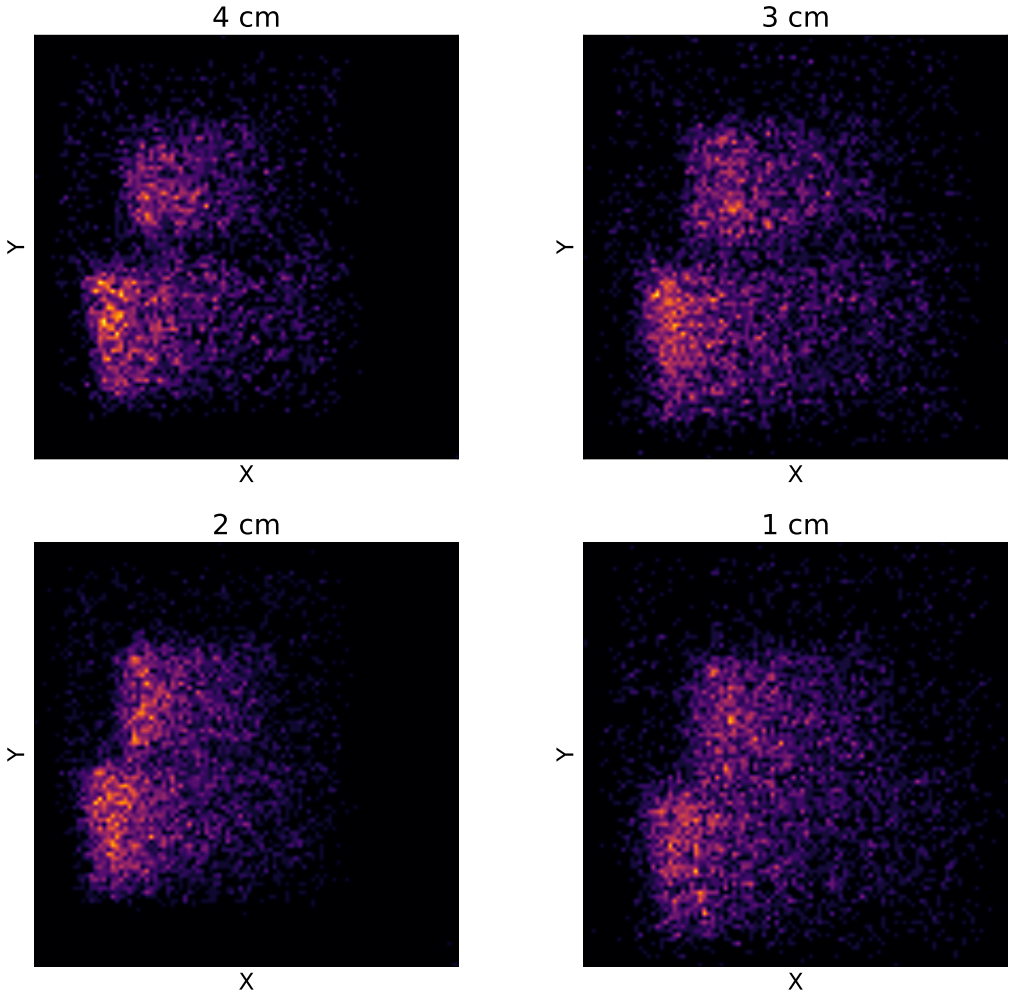

Figure 4.18: LaBr experimental results for the system X-Y resolution with graphite bricks. The achieved resolution is somewhere between 2-3 cm.

4.5 Conclusions and Outlook

In this chapter we presented the performance of the API system. Specifically, we showed that the instrument is capable of approximately 7 cm resolution along the Z-axis, which is determined by the overall time resolution, and the X-Y resolution is approximately 2-3 cm. It is important to note that this resolution is at one specific distance from the generator (60 cm) and it changes as a function of this parameter. The X-Y resolution can be further improved with a smaller neutron beam spot, but there is a trade-off between beam spot size and DT beam current, which is proportional to the neutron yield. Additionally, a focused DT beam would require a more involved cooling system in order to cope with the increased

heat flux on the target. Therefore, the beam spot size cannot vary too much from 1-2 mm. The X-Y resolution on the alpha detector also determines the overall position resolution. However, the performance of our alpha detector, as discussed in Chapter 2 is close to its optimum and would be difficult to improve on this. On the other hand, there can be a significant improvement in the Z direction with a more optimized timing algorithm or a faster combination of digitizer and FPGA. A time resolution of 1 ns with YAP and LaBr is within reach of current technology and therefore, the depth resolution can improve by at least 30%.

Chapter 5

Analysis of API Gamma Spectra and Initial Samples

Gamma-ray spectra contain information regarding the isotopic nature and absolute abundance of the interrogated sample, as explained in Chapter 1. However, even an API spectrum, which selects in a small volume only certain types of reactions that interact with nuclei in short time frames of a few nanoseconds such as inelastic scattering, can be complex to analyze because there are usually different isotopes of a single element, each with its unique gamma fingerprint. Additionally, each isotope has a nuclear structure that may result in the emission of several gamma rays with different energies. Therefore, it is important to understand the detector response for single elements before analyzing a more complex sample such as soil. Furthermore, in order to obtain the abundance of each isotope, it is necessary to perform an efficiency calibration for each voxel and a measurement of the total neutron flux integrated over the measurement time, i.e fluence. This chapter discusses some of these initial considerations in the context of carbon content determination in soil samples and other specific elements relevant to soil chemistry. A similar discussion and analysis as the one presented in this chapter has already been published in [49] where we present results from a different data set and provide more details regarding the sample preparation.

5.1 Single-Element API Gamma Spectra

Several elements were identified as the most abundant in forest and agricultural soils, as shown in Table 5.1. Notice some of the interfering lines in the carbon signal mostly due to ^{16}O and ^{28}Si, which are usually present in these types of soils in greater quantities than carbon. These gamma rays do not all originate from neutron inelastic scattering. In fact, some of the most important interfering lines are the result of other types of reactions or gamma transitions within certain nuclei. For instance, two significant interfering reactions are shown in Equations 5.1 and 5.2.

$$n + {}^{16}O \rightarrow n' + \alpha \; + {}^{12}C^{*} \qquad \gamma = 4.439\,\text{MeV} \tag{5.1}$$

$$n + {}^{28}Si \rightarrow n' + {}^{28}Si^{*} \qquad \gamma = 4.497\,\text{MeV} \tag{5.2}$$

The reaction shown in Equation 5.1 results in an excited state of ^{12}C, which relaxes by the emission of a 4.439 MeV gamma ray, and therefore it is indistinguishable from our signal of interest [34]. It will be shown below (Figure 5.3) that this reaction may be significant mainly because of the large relative abundance of oxygen in the soil. However, experimental data for the cross-section of this specific reaction at 14.1 MeV incident neutron energy could not be found by the author at the time of publication, which highlights the need to measure this cross-section for a more accurate determination of carbon abundance. Figure 5.1 shows the experimental cross-section for this particular reaction as measured by [35] (obtained from the database EXFOR [62]), and its corresponding evaluated cross-section from ENDF [4]. Note that there is no documented measurement in this database for 14.1 MeV incident neutron energy and the error bars in the vicinity have a magnitude of ±1 MeV. On the other hand, Yakubova et al. argue that this reaction may not impact soil carbon measurements significantly [26], but they also found large discrepancies in evaluated cross-section values from different data libraries. Specifically, in [59] and [58] they used the data library JENDL4.0 [44] to account for such reaction given that G4NDL4.5 (the default cross-section library from Geant4 [2] that draws their values mostly from ENDF) reported a value of 127 mb for this reaction compared to 36.6 mb in JENDL4.0. This discrepancy can be observed in Figure 5.1. The other reaction shown in Equation 5.2 is the result of a nuclear cascade transition between two energy levels in ^{28}Si, i.e. 6.276 MeV(+3) → 1.779 MeV(2+). The resulting gamma-ray energy is not resolvable in LaBr given that its energy resolution at that energy is approximately ±120 keV. Therefore, its contribution to the carbon peak needs to be accounted for during analysis.

Element	**Isotopic abundance (%)**	**Main gamma energies (MeV)**
Carbon	^{12}C: 98.9	4.439
Aluminum	^{27}Al: 100	0.844, 1.72, 2.21, 2.98
Oxygen	^{16}O: 99.76	2.74, 3.089, 3.68, 3.854, 4.439, 6.13
Iron	^{54}Fe: 5.85, ^{56}Fe: 91.75, ^{57}Fe: 2.12	0.847, 1.238, 1.81
Silicon	^{28}Si: 92.2, ^{29}Si: 4.7, ^{30}Si: 3.1	1.78, 2.838, 4.489

Table 5.1: Most common elements present in soil, their natural isotopic abundance (greater than 2%), and their main prompt non-elastic gamma-ray energies.

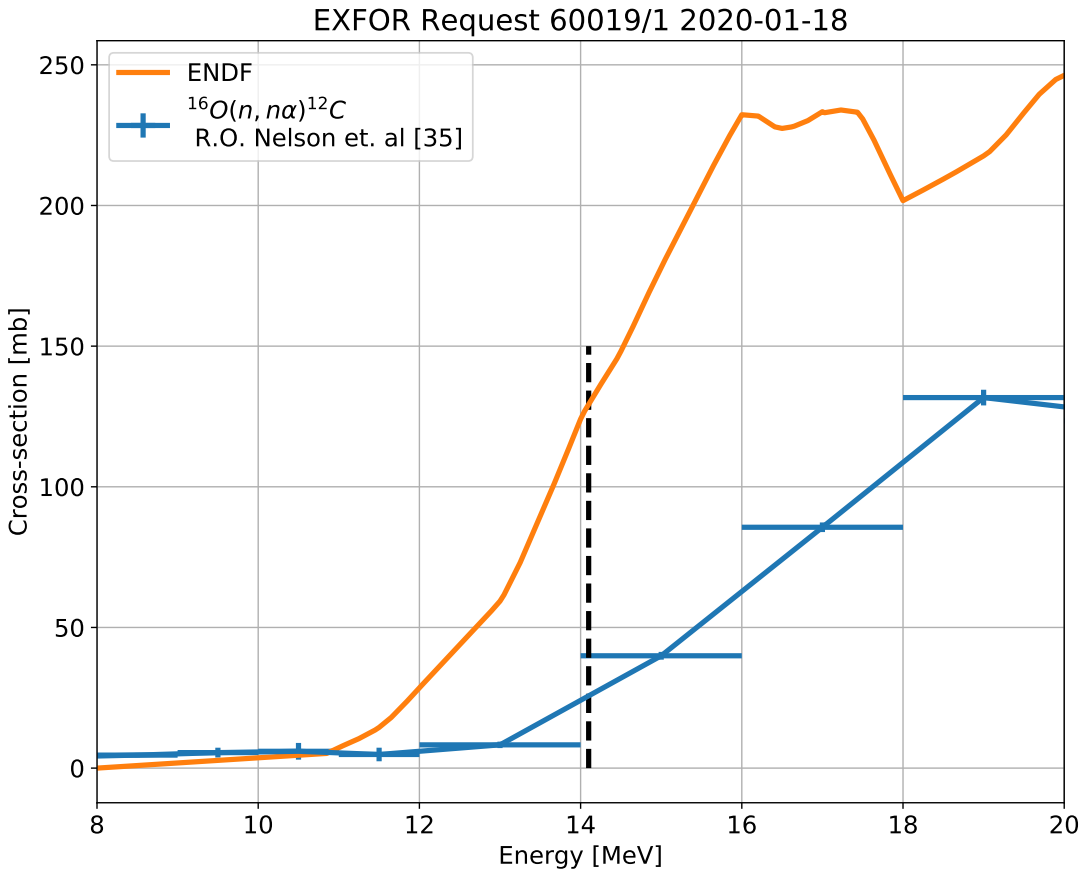

Figure 5.1: Comparison between experimental cross-section values available in EXFOR [62] and its corresponding evaluated cross-section from ENDF [4] for the reaction shown in Equation 5.1. The vertical dashed line indicates the 14.1 MeV line. Note that at this energy there is a large discrepancy between the two of approximately a factor of 5. Additionally, the error bars in the vicinity are ±1 MeV. This reaction can have an impact on the accuracy of carbon measurements in soil.

Given some of these uncertainties, we took a more practical approach by irradiating in coincidence some specific materials relevant to most common soil compositions in order to obtain element-specific spectra that can be used in the analysis of soil samples. The experimental procedure is exemplified in Figure 5.2, which shows an iron sample (SS1018) that was irradiated for 100 min at a neutron generator voltage of 50 kV. The sample was placed approximately 60 cm underneath the neutron generator. The corresponding time spectrum is obtained by constructing a histogram of the difference in recorded times between

the YAP and gamma detectors. The time is restricted to selectively capture the sample in question (Z-dimension) and likewise for the X and Y dimensions. The resulting gamma spectrum unique to natural iron is shown as the last step of this process in Figure 5.2. Important experimental parameters are shown in Table 5.2.

Material	**Distance** ± 2 **[cm]**	**Mass** ± 0.005 **[kg]**	**Density** $\pm 2\%$ **[g/cm^3]**	**Run time** **[s]**
Aluminum (6061)	$0, 0, 52$	4.210	2.63	4760
Graphite	$0, 0, 56$	3.100	1.93	7000
Water	$0, 0, 60$	2.470	1.00	7000
Silicon	$0, 0, 55$	3.164	2.4	7000
Iron (SS1018)	$0, 0, 56$	0.306	3.54	6000

Table 5.2: Experimental parameters used to obtain single-element gamma-ray spectra. The distance is shown as (X, Y, Z) measured from the neutron production surface to the center of the sample. Pure silicon was obtain from unused silicon wafers.

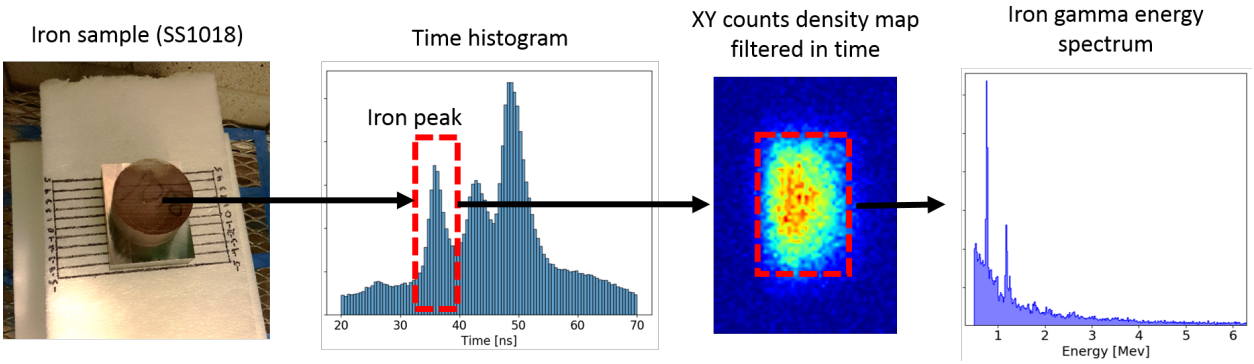

Figure 5.2: Example of the analysis procedure for obtaining elemental gamma spectra for specific elements. The photograph of the sample is a top view from the perspective of the neutron generator. The LaBr detector is located to the left of it.

The API method can be useful to not only identify the composition of a sample, but also to quantify its absolute isotopic abundance. Additionally, this technique can be employed to measure inelastic scattering cross-sections at 14.1 MeV. Figure 5.3 and 5.4 show the measured gamma spectra for different elements using the method outlined above for both LaBr and NaI, respectively. The main gamma lines shown in Table 5.1 can be observed

in the spectra. However, many lines are washed-out due to the finite energy resolution of the detectors, particularly in NaI. The following discussion focuses on LaBr only because of the better quality of the data in terms of energy and time (depth) resolution, but the same procedure and logic also applies to NaI.

An interesting side note to this API technique is the possibility of neutron scattering from one material to the other, which results in the incorrect calculated position and would show up in the data set even when time windows are restricted to the nanosecond level. For instance, an emitted neutron can scatter off an aluminum nucleus and still have enough energy to excite a ^{12}C nucleus located nearby. The resulting gamma ray could interact in the gamma detector and hence a 4.4 MeV line would show in the aluminum spectrum. In order to investigate the significance of this process, we carried out another experiment where two samples of aluminum and carbon where irradiated next to each other at the same time. The samples are separated in the X direction by 8 cm, as shown in Figure 5.5. The spectra shown correspond to only one region in the inset (top: graphite, bottom: aluminum). Notice the significant scattering happening from aluminum to carbon as evidenced from the 4.4 MeV peak present in the aluminum spectrum. On the other hand, scattering from carbon to aluminum does not seem to be as significant. Further analysis is required to fully understand this effect.

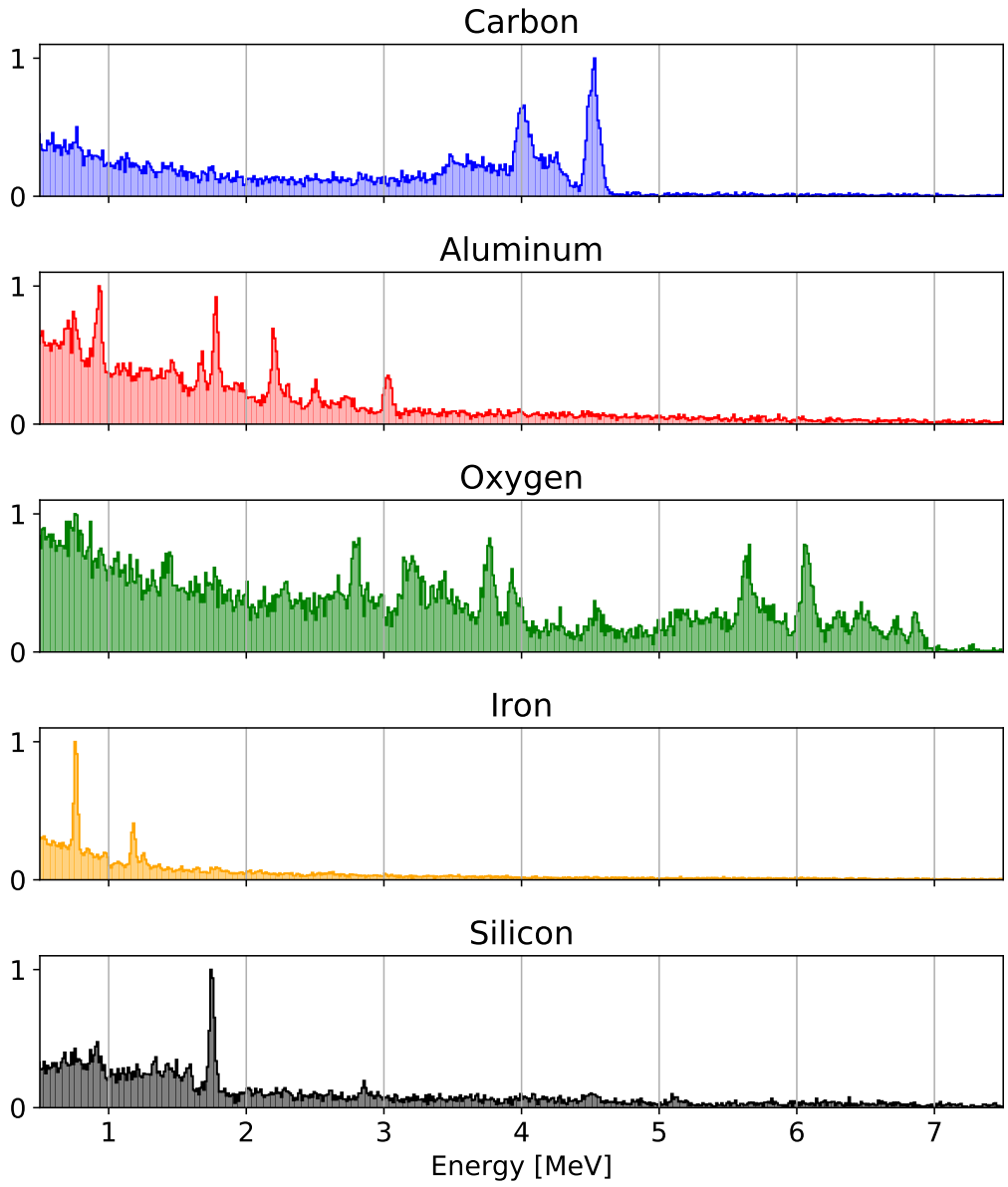

Figure 5.3: Measured API gamma spectra of relevant elements for soil chemistry using a LaBr detector. For irradiation details refer to Table 5.2.

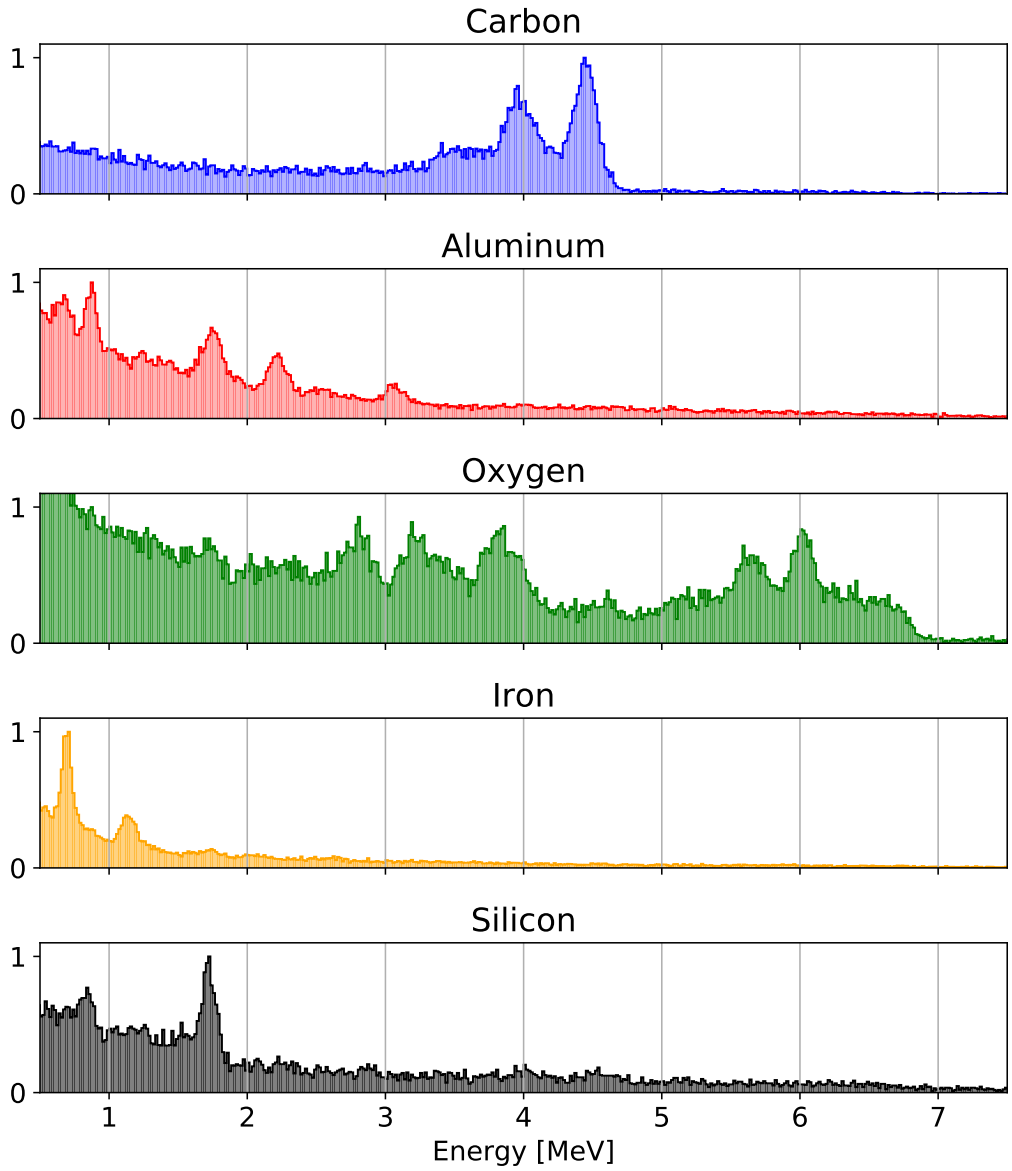

Figure 5.4: Measured API gamma spectra of relevant elements for soil chemistry using a NaI detector. For irradiation details refer to Table 5.2.

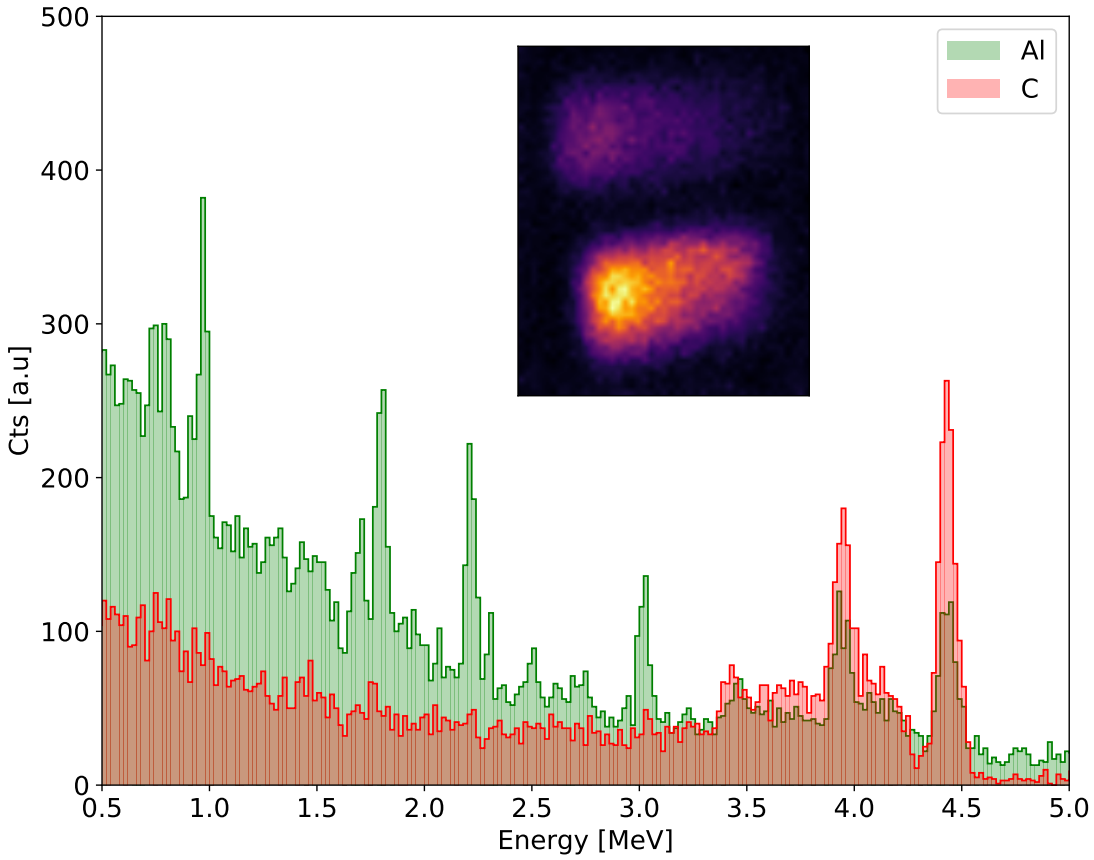

Figure 5.5: Neutron scattering effects resulting from two samples (graphite and aluminum) separated by 8 cm being irradiated at the same time. The spectra correspond to only one region in the inset, respectively (top: graphite, bottom: aluminum). Note that this effect is more pronounced in the aluminum spectrum where carbon peaks show up. The same aluminum sample was irradiated separately and its spectrum is shown in Figure 5.3.

5.2 Single-Element Response Comparison with MCNP6

The experimental data obtained for specific elements in the previous section were compared to MCNP6 with the simulation technique explained in more detail in the last section of Chapter 3. The gamma-ray response corresponding to LaBr is shown in Figure 5.6. Note that there is a relatively good overall agreement, specifically for the main prompt gamma rays. Nevertheless, there are significant discrepancies in regards to relative intensities for most elements. In particular, from this representative sample, ^{27}Al presents the largest divergence from MCNP6. Interestingly, notice that the 4.439 MeV peak in the ^{16}O spectrum due to the reaction shown in Equation 5.1 seems to agree with MCNP6, which draws its cross-section values from ENDF. This could indicate a large discrepancy from the experimental value shown in Figure 5.1. The carbon signal is not shown in Figure 5.6 because it was already presented in Chapter 3. MCNP6 simulations can be improved by using more optimized parameters for Equation 3.6. Similar spectra for some of the same elements were obtained by [25] and [15]. They found similar discrepancies with MCNP6, which highlight the need for more accurate nuclear data measurements. These types of simulations are important for data analysis and experiment planning. For instance, the overall elemental concentration in a soil sample could be calculated with a linear combination of these elemental spectra.

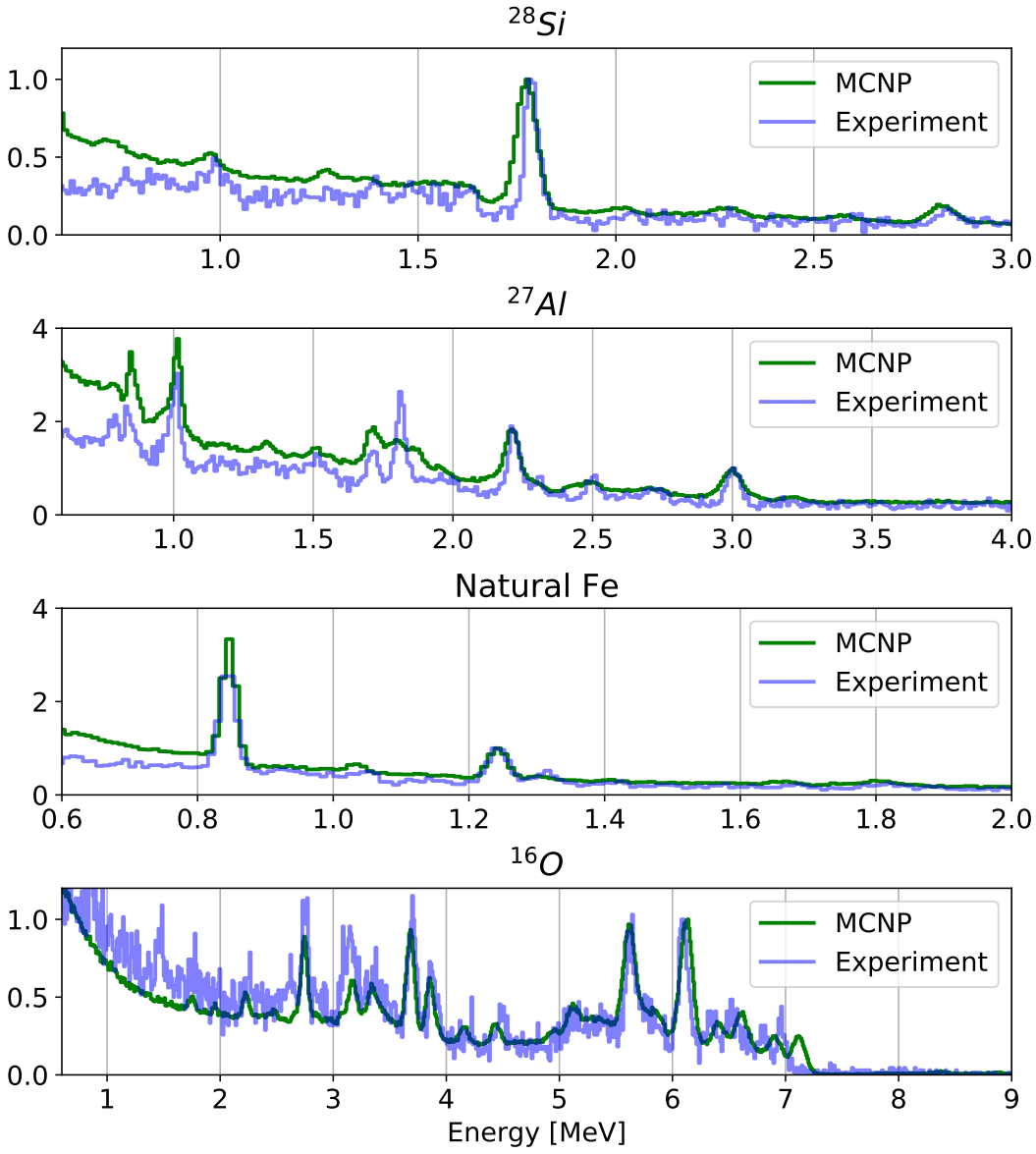

Figure 5.6: Comparison between measured gamma-ray spectra and MCNP6 simulations for elements relevant to soil composition. Note the overall agreement, but there are significant discrepancies for ^{27}Al, in particular. The spectra were normalized by the most significant highest-energy gamma.

5.3 Dry Soil Samples with Varying Carbon Content

Soil samples were prepared by mixing pure sand (SiO_2) with worm casting, which has a high carbon content (greater than 40%). Three samples were prepared with the following worm casting concentrations: 0%, 3%, and 10%. Note that this would be equivalent to approximately: 0%C, 1.2%C, and 4%C. The soil samples as seen from the top are shown in Figure 5.7. They were placed in two aluminum boxes, each with dimensions of 7.5 cm × 7.5 cm × 12.5 cm. The resulting gamma spectrum from the soil samples using the procedure explained above is shown in Figure 5.8.

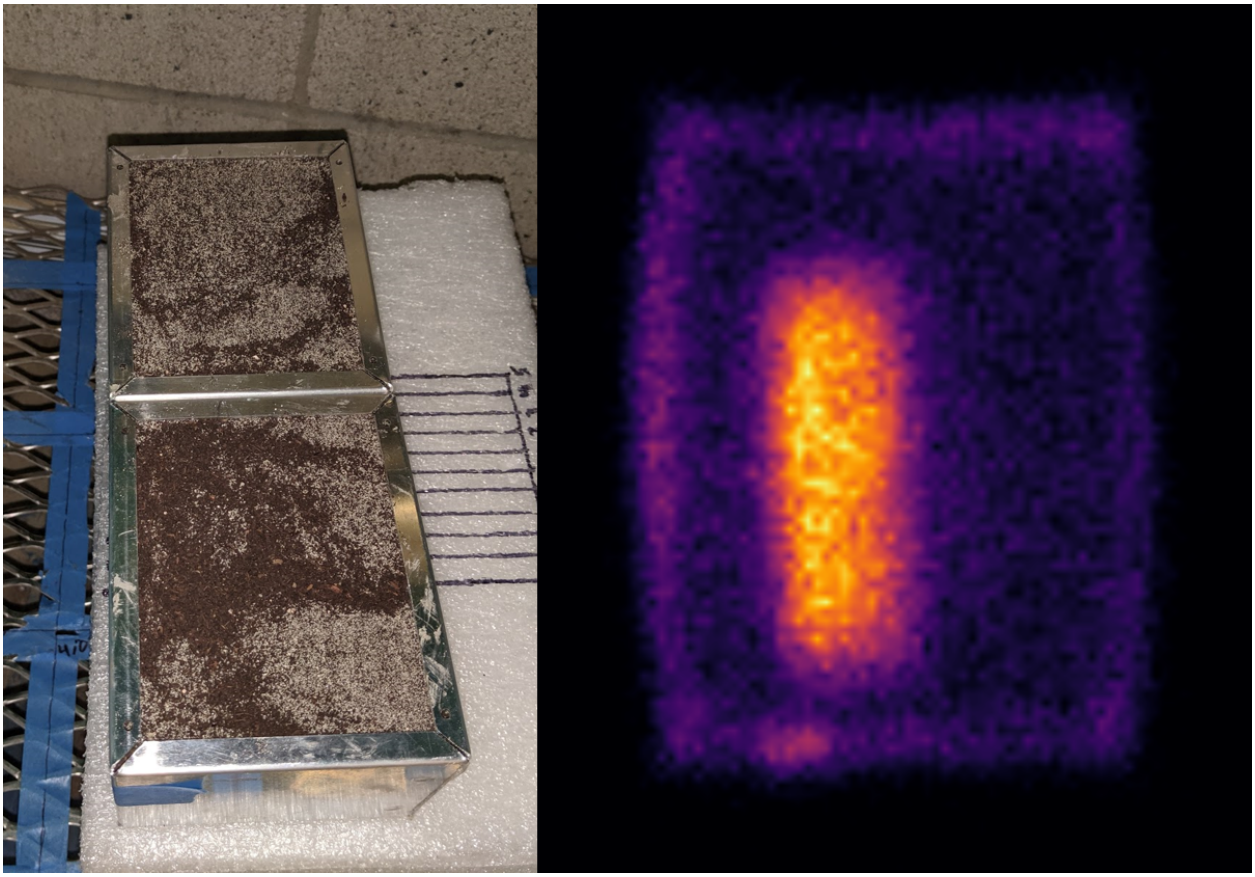

Figure 5.7: Soil sample containing a mixture of sand and worm casting, and its resulting 2D image using the API technique.

These spectra were normalized to the 1.78 MeV line from ^{28}Si in order to account for different irradiation times and amount of sand in the samples. Notice the interfering reactions discussed above resulting in some counts underneath the carbon peak. These preliminary data show that for carbon concentrations below 1%, better statistics is clearly needed together with further study on sources of error. Because there are more energy bins than

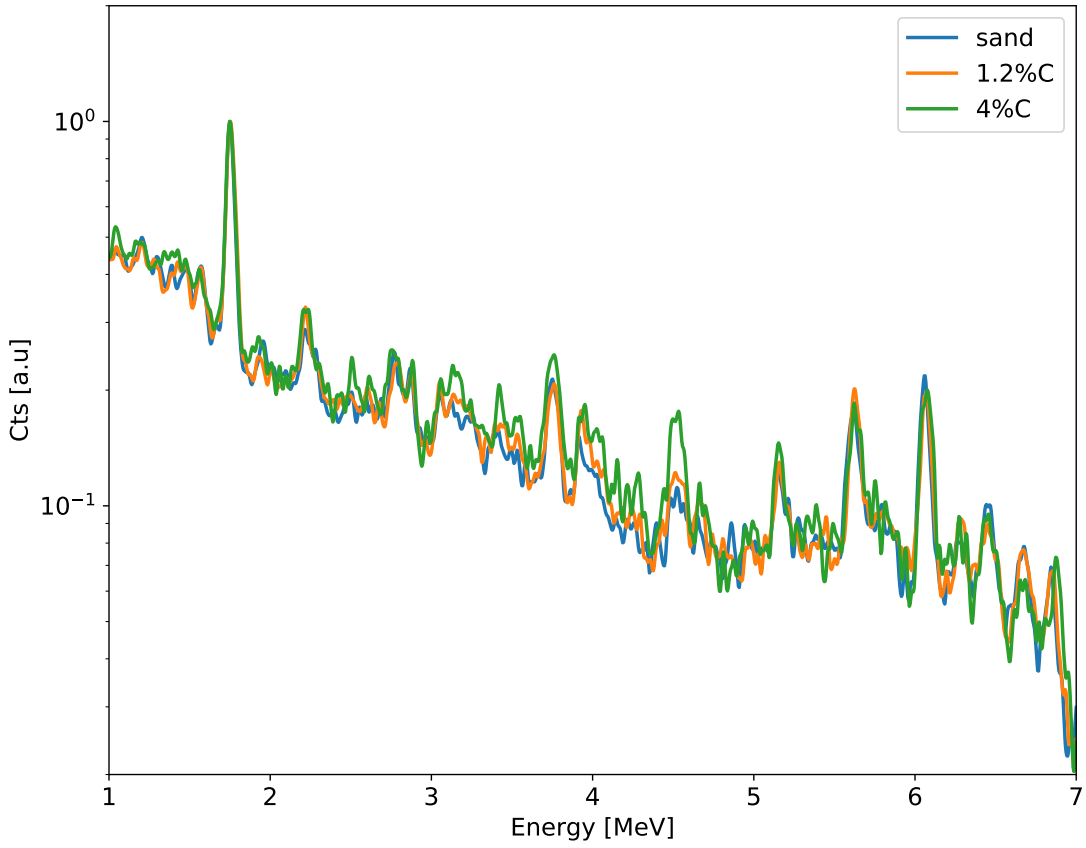

Figure 5.8: Resulting gamma spectra of soil samples with different carbon concentrations. The samples were prepared by mixing pure sand and worm casting. The spectrum is smoothed out with a Gaussian Kernel Estimation (KDE) algorithm implemented in Python. Note the carbon peak at 4.4 MeV showing the difference in relative carbon concentrations.

needed given the limited resolution of our detectors, it is possible to smooth out the data for more efficient analysis by either averaging over more bins or implementing different types of algorithms such as Gaussian Kernel Estimation (KDE) or moving average filter. Both of these techniques resulted in very similar smoothed spectra. Further work is required to optimize the parameters in these filters.

This spectrum is more complicated to analyze given the overlap of all the gamma lines from the individual elements. Therefore, we used the Python-based gamma spectrum analysis software becquerel [5], which allows for peak detection, FWHM calculation, and energy calibration among others. Figure 5.10 shows the non-calibrated gamma spectrum for the

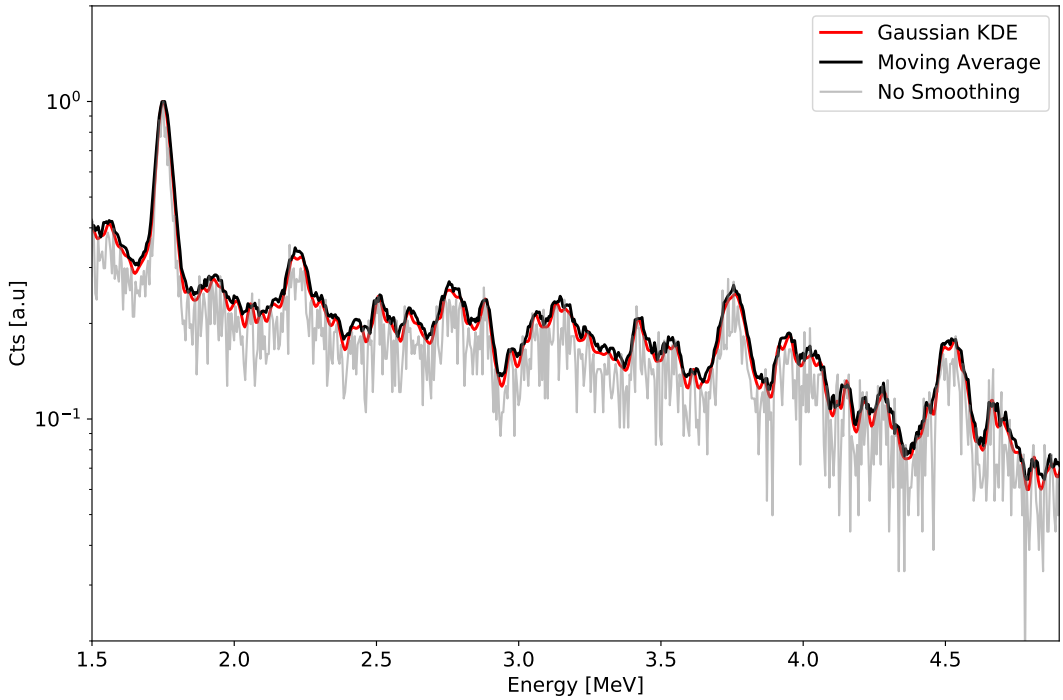

Figure 5.9: Comparison of different algorithms for data smoothing. Both the KDE method and the moving average filter yielded similar results. The data presented is for the case of 10% worm casting.

case of 4% carbon together with the results of becquerel's internal algorithm to detect peaks of interest and their respective FWHM.

The capabilities of becquerel are very useful specifically for energy calibration and FWHM calculation since the latter serves as input for MCNP6 simulations. Additionally, it can be used for peak integration accounting for proper background subtraction.

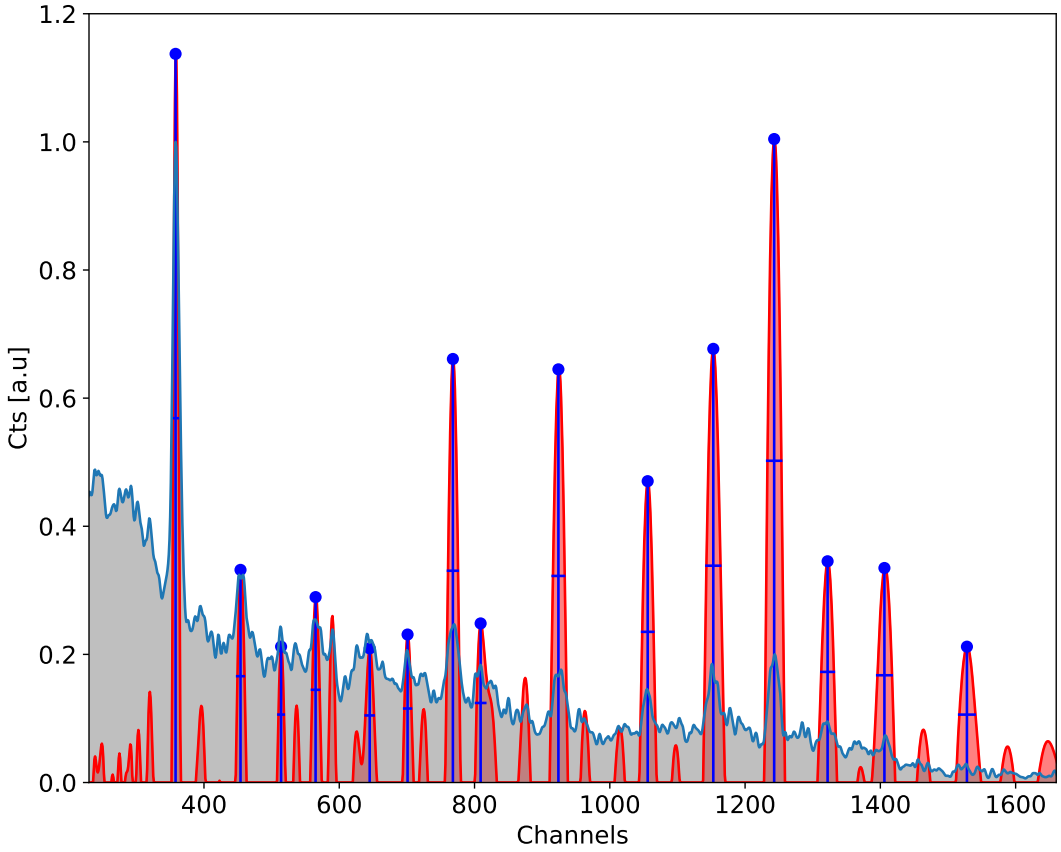

Figure 5.10: Peak finding and FWHM calculation using becquerel. It uses energy-dependent kernels that can be convolved with a spectrum to extract lines from the background continuum [5].

5.4 Soil Analysis Outlook

The soil samples analyzed in this chapter are the first step of the analysis pipeline which requires an end product of absolute carbon content. This would require an efficiency calibration based on the location of origin of the gamma ray together with corrections for neutron/gamma attenuation through soil. Preliminary experiments have already taken place and data analysis will be published in the future. Additionally, refinements regarding MCNP6 simulations are needed to predict measurement times, compare inelastic scattering cross-sections, and extract more information from actual measurements.

Chapter 6

Next Generation API Systems

As part of this project, a second neutron generator is being built by Adelphi Inc. [1] that takes into account important design changes which resulted from the experience obtained with the first one. These changes will improve the performance in terms of better position resolution, higher neutron yield, lower X-ray interference, more efficient cooling, and the ability to handle higher alpha rates. In this chapter we present simulations and experimental tests that led us to recommend certain design changes in the API system.

6.1 Improvements on the Alpha Detector

Lower X-ray and Gamma Sensitivity with a Thinner YAP

During operation of this type of neutron generators, X-rays are produced by different means including beam-gas interactions, electron acceleration in the ion source, and ions hitting the target (Bremsstrahlung radiation). The maximum energy of these X-rays is equal to the accelerating voltage, which is more than three orders of magnitude lower than that of the alpha particle. However, the rate can be several orders of magnitude higher depending on the geometry, efficiency of the secondary electron suppression system, operating gas pressure, etc. Therefore, they will have an impact on the alpha waveform in terms of increased "graininess" or noise, which results in a larger error determining the energy accurately, which in turn means that they have a negative impact on the position resolution. We identified beam-gas interactions as the process that mostly contributes to X-ray production directly affecting the YAP signal. The reason for this is that sealed-type neutron generators operate at a high pressure of a few mTorr, and this pressure is the same in the ion source and the accelerating drift region. This characteristic makes it even possible to see the beam with the naked eye (actually atomic recombination processes within the accelerating region). The beam path is around 6 cm from the YAP crystal and there is only a thin (1 µm) aluminum foil in between, which results in energetic X-rays making it to the YAP crystal where they can be absorbed and generate signals. Additionally, the neutrons produced can interact with the neutron

generator structural materials, particularly with the copper target backing. Two isotopes of copper, ^{63}Cu and ^{65}Cu, have a significant production of 511 keV gamma rays, as shown in Figure 6.8, which is the result of an MCNP6 simulation. These relatively low gamma ray energies will also have an impact on the YAP signal. This effect can be reduced by reducing the amount of copper, but making sure there is enough left for proper heat transfer. The reduction of copper will be discussed in greater detail in the next section. In order to reduce the amount of X-rays and gamma rays that interact with the YAP, we decided to use a different YAP crystal with a reduced thickness, which would stop all alpha particles and reduce the X-ray and gamma ray interactions in the crystal. The attenuation was calculated for two different YAP thicknesses: 1 mm and 100 µm. Note that the latter is sufficient to stop all alpha particles as SRIM [64] simulations indicated in Chapter 2, which shows that most 3.5 MeV alpha particles stop within the first 7-8 µm inside the YAP. The results are shown in Figure 6.1.

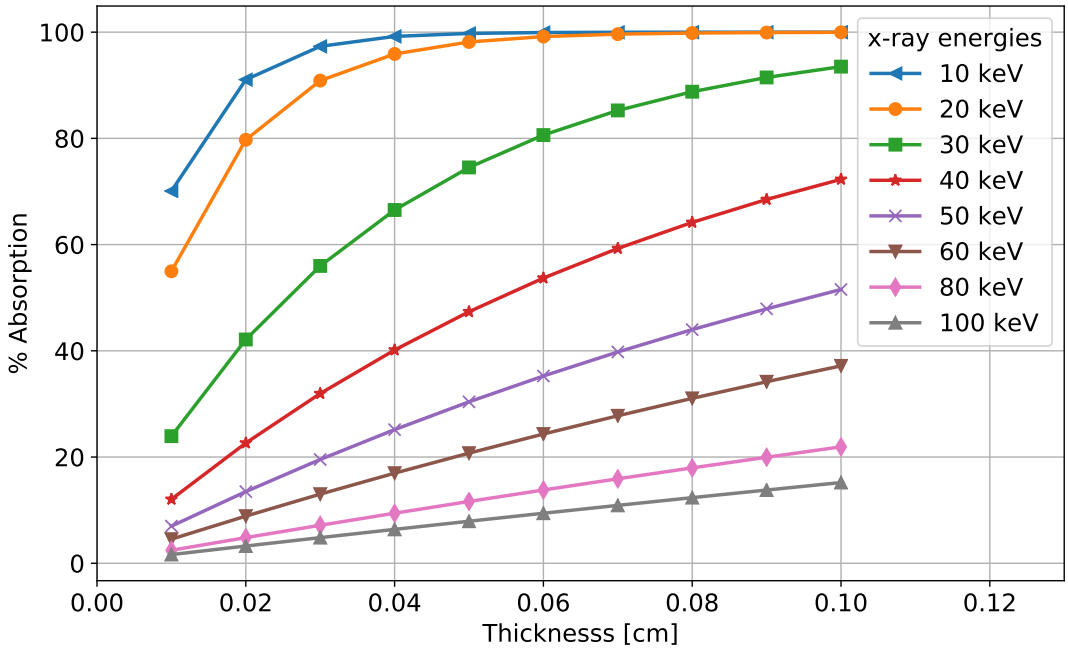

Figure 6.1: Percent X-ray absorption in YAP for different energies. Note the significant reduction for the thinner YAP (0.1 mm) compared to the current YAP crystal (1 mm).

In order to test the performance of different YAP thicknesses, i.e. 1 mm (currently in use) vs. 0.1 mm, we performed several experiments with an ^{241}Am source, which emits a 5.5 MeV alpha particle and a 59.6 keV gamma-ray, the latter used as a proxy for the X-rays emitted by the neutron generator. Figure 6.2 shows the different YAP responses to the

59.6 keV gamma ray emitted by ^{241}Am. The source was placed approximately 15 cm away from the YAP crystal in a small test vacuum chamber. However, for this test, the pressure inside the chamber was equal to the atmospheric pressure in order to stop alpha particles within its volume and allow only gamma rays to reach the YAP crystal. Note the tail of the distribution in the case of the thin YAP with an apparent shift to higher energies. This is due to the fact that the PMT mounted with the thin YAP was operated at a higher voltage. The reason for operating at this higher voltage was the experimentally observed higher light yield for the thick YAP.

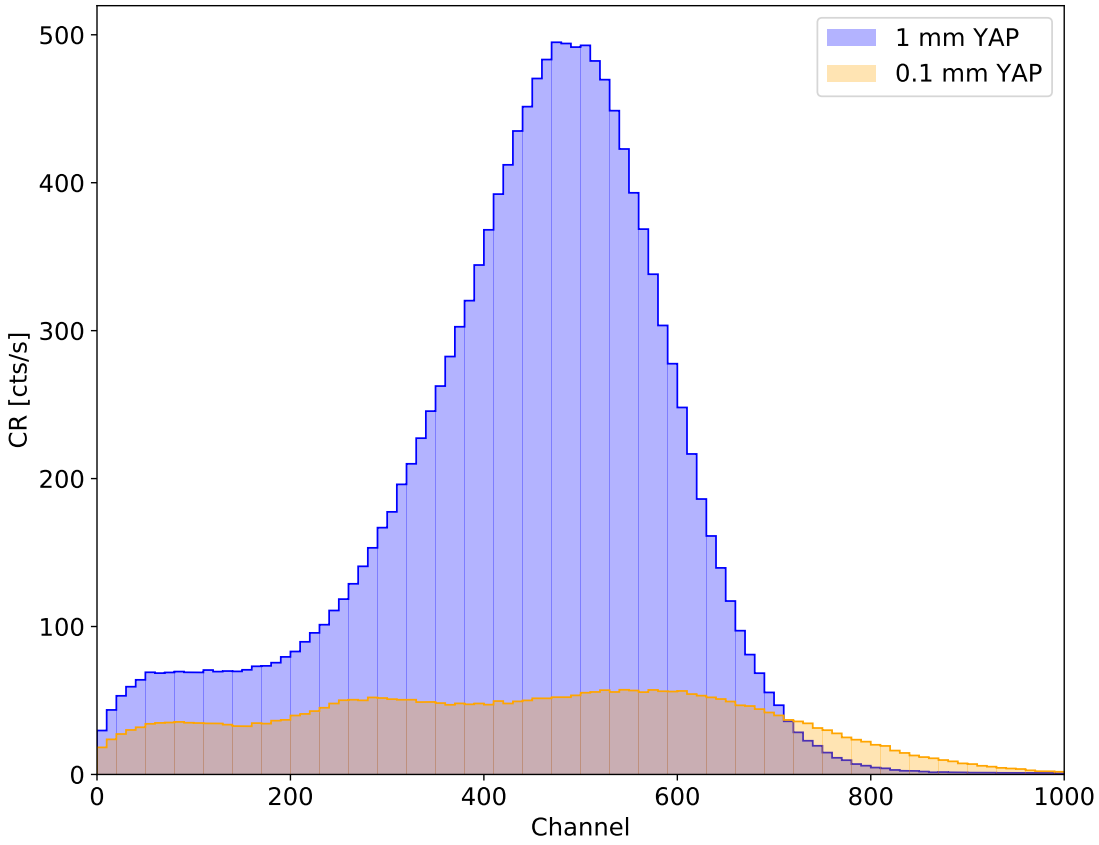

Figure 6.2: Comparison between two YAP crystals of different thicknesses with respect to low-energy gamma ray response. The sensitivity to 59.6 keV gamma rays is a factor of 10 higher in the case of the thick YAP.

Additionally, we recorded 100 traces using a digital oscilloscope [39] for each YAP crystal

and averaged over all of them in order to have a sense for the noise on top of the signal due to gamma rays from the ^{241}Am source. The results are shown in Figure 6.3.

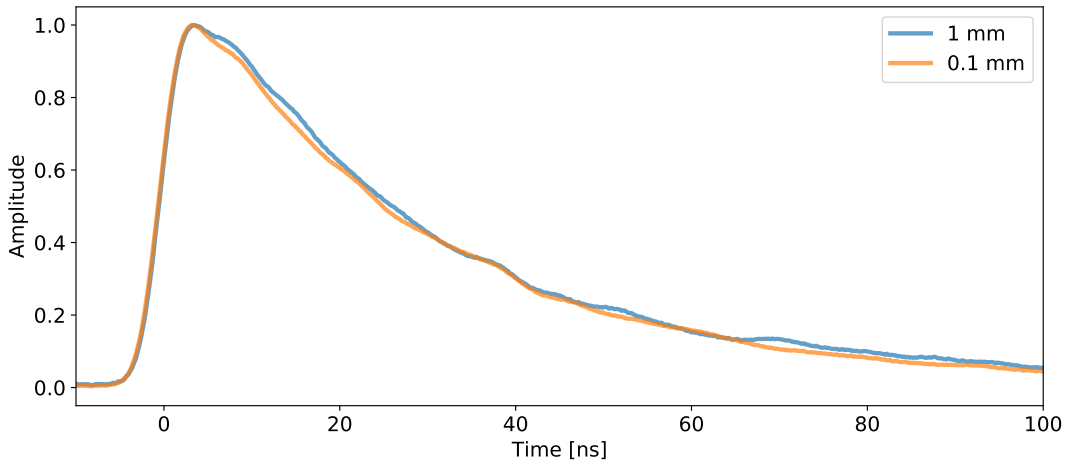

Figure 6.3: YAP response to alpha particles and gamma rays emitted from an ^{241}Am source in two different YAP crystals. The traces correspond to the average of 100 individual ones for each case. Note that the traces are very similar as expected. It may be that there are fewer fluctuations due to X-rays from the alpha source in the case of the thinner YAP, but further statistical analysis is required to confirm this.

The plot shows a more smooth curve for the thin YAP with fewer fluctuations. However, this treatment is not very rigorous and it only serves for a qualitative comparison. The final test consists of placing a flood-field mask (the same as the one shown in Chapter 2) and performing the reconstruction routine. The results are shown in Figure 6.4. Note the greater spread between interaction points, which would result in a better position resolution particularly near the edges. Therefore, we can conclude that the thin YAP is superior and will be mounted in our next API tube.

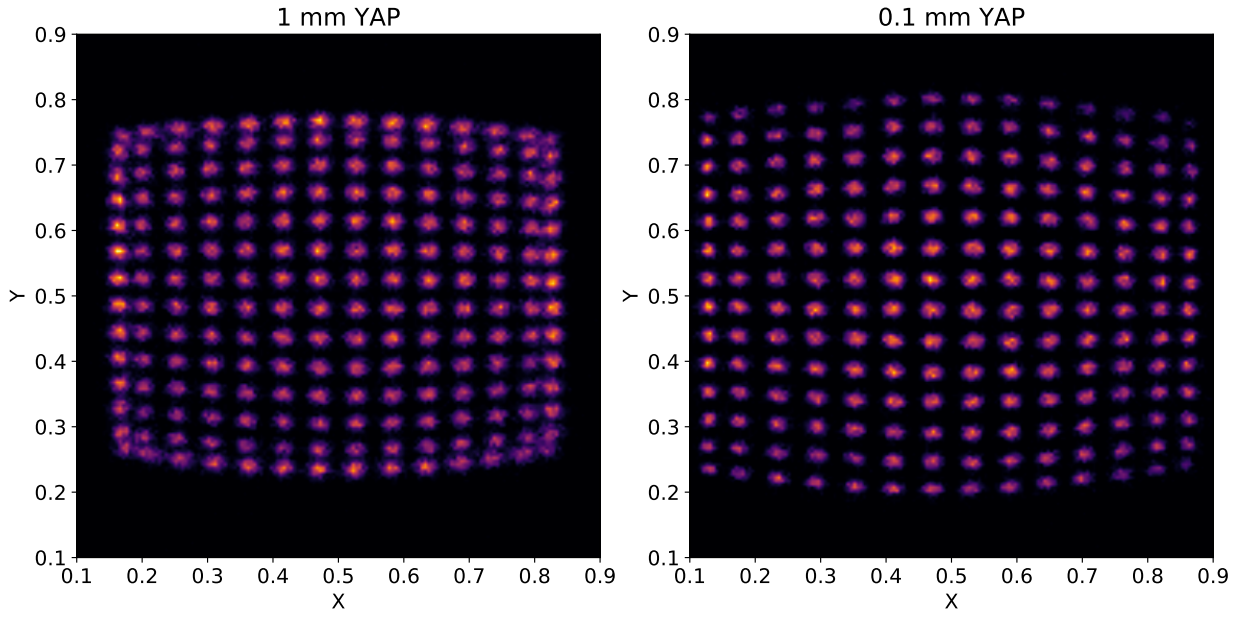

Figure 6.4: Position reconstruction for two YAP crystals with different thicknesses. The thinner YAP has a larger spread and hence better edge response.

Improvement on Alpha Rate Handling Capabilities with a 16×16 Readout Board

COMSOL [11] simulations of ray tracing through the alpha detector system shown in Chapter 2 indicate that after a single alpha event, the resulting scintillation light spreads over 3×3 pixels onto the photocathode, which is important in order to obtain a sub-pixel resolution. However, every alpha interaction creates a dead time in the detector when a 4-corner readout is used because every pixel is activated, as discussed in more detail in Chapter 2. If we decouple the readout of the pixels by rows and columns, one alpha interaction would activate at most 3 rows and 3 columns, allowing the other inactive pixels to read another incoming alpha particle. Therefore, the dead time would be reduced by a factor of 3. This is because an alpha particle interaction renders $3 \times 16 + 3 \times 16 - 9 = 87$ pixels inactive, leaving $256 - 87 = 169$ pixels ready to read another incoming signal. In light of this rationale, we designed a 16 × 16 readout board similar to the one shown in [54] and [40]. The board is shown in Figure 6.5 and it is constructed that way in order to avoid crossing connectors which

would increase noise from capacitive coupling. The readout logic is further complicated due to the fact that we are now required to read in coincidence 32 channels instead of only four in order to calculate the position of interaction. Performance results will be published in the future.

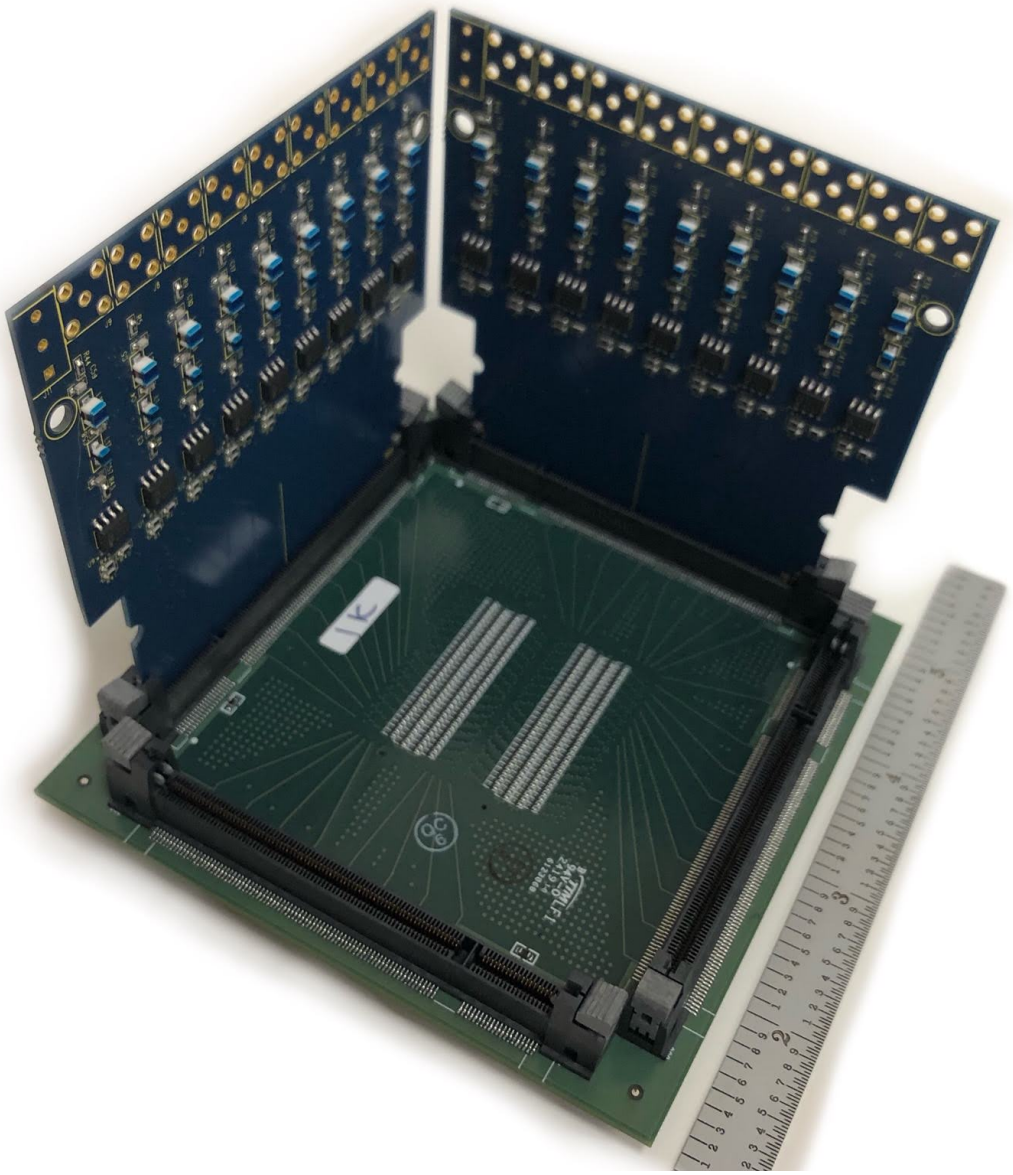

Figure 6.5: Row-column readout board designed by the Engineering Department at LBNL. This new board will allow for higher alpha rate handling capabilities.

6.2 Design Parameters for an Improved API Neutron Generator

API Target Considerations

Commercially available neutron generator targets are usually made of a thin layer of titanium with a thick copper substrate, which can act as a neutron scattering center, as shown schematically in Figure 6.6. The scattered tagged neutron will then have an incorrectly calculated trajectory but it can still be within the API cone and induce a reaction of interest within the API time window. Therefore, this event would appear in the reconstructed image and increase the rate of false coincidences.

In order to reduce this unwanted effect, we performed MCNP6 simulations to quantify the neutron scattering as a function of copper thickness. The simple MCNP6 model consists of a pencil beam of 14.1 MeV neutrons incident upon a copper target of various thicknesses. We tallied the position of scattered neutrons that cross an artificial "screen" located 5 cm from the target. This allows for the calculation of neutron scattering as a function of incident angle, as shown in Figure 6.7. Note that the FWHM is around 11°, which is inside the API cone, i.e. 45°. The current generator has a target thickness of 4 mm and the new one will have a thickness of 2 mm, hence reducing the scattering by approximately 50 % allowing for sharper images. These distributions present with non-Gaussian tails which suggest some preferential scattering. However, these are not significant to our application.

A similar argument can be made regarding the passage of alpha particles through the titanium layer. There can be changes in trajectory of alpha particles because of this effect. Therefore, the new generator will have the YAP tilted a few degrees with respect to the target in order to reduce alpha scattering. Additionally, the target region experiences the highest neutron flux and hence we need to consider induced nuclear reactions within its volume that lead to the emission of low to medium-energy gamma rays in order to minimize their flux onto the YAP crystal. These gamma rays can significantly contribute to unwanted background signal. Therefore, we performed another MCNP6 simulation to approximate the rate and energies of gamma rays detected by the 1 mm YAP crystal. Due to the proprietary information regarding the generator design, details of the simulation cannot be shown here, but the total copper volume is around 40 cm^3. The gamma spectrum resulting from the total energy deposition in the YAP crystal (F6 tally) is shown in Figure 6.8. The maximum gamma rate experienced at 2×10^8 n/s is 2000 γ/s.

Note that there is a sizable contribution from 511 keV gamma rays coming from the two most abundant copper isotopes ^{63}Cu and ^{65}Cu. There are a few ways to minimize this contribution besides making the YAP crystal thinner as detailed in the previous section. The amount of copper in the target can be reduced but care must be taken to keep the proper heat transfer capabilities. Therefore, we performed COMSOL simulations in order to understand the dependence of the maximum temperature experienced by the target as a function of its radius (thickness set to 2 mm). The results are shown in Figure 6.9. Figure 6.10 shows the

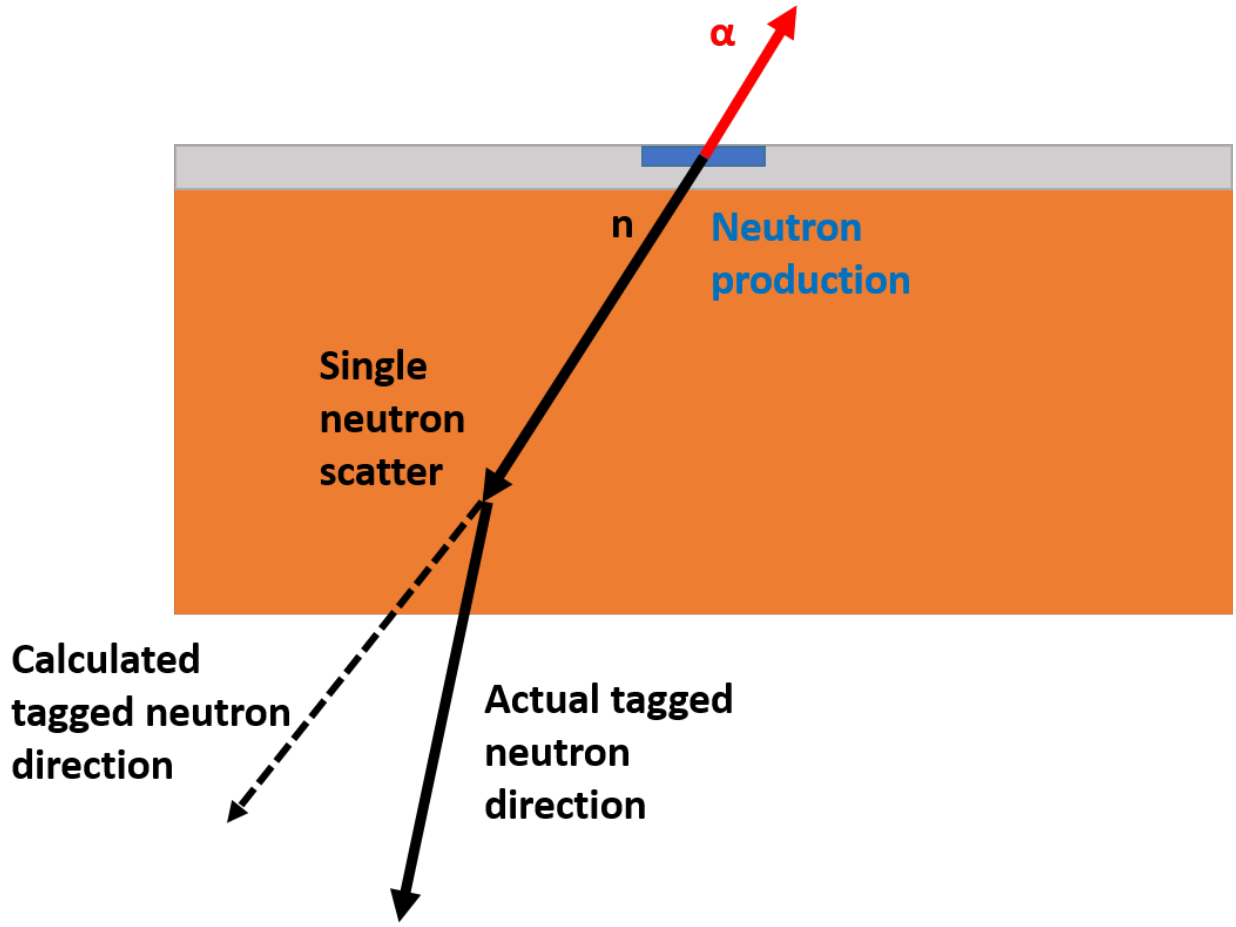

Figure 6.6: Schematic representation of a single neutron scattering in the target volume which leads to the incorrect calculated neutron trajectory and hence atom location. This effect can be reduced by decreasing the copper thickness.

geometry and results for the case of 3 mm radius.

These results are valid for a uniformly distributed beam profile with diameter equal to 1 mm, 50 µA of beam current, and 100 kV. The power density on the target surface is 40 W cm^{-2} with these assumed parameters. Note that the maximum allowed temperature is approximately 200 °C at which point there is significant hydrogen degassing from titanium, which drastically reduces the neutron output [13]. Simulations show that we need a target with a diameter of at least 1 cm to operate below this temperature limit with a safety factor greater than two. Additionally, this simplified simulation assumes perfect cooling in the back of the target. More detailed simulations show that the maximum temperature increases to approximately 85 °C with standard air cooling and to more than 200 °C if left to be cooled

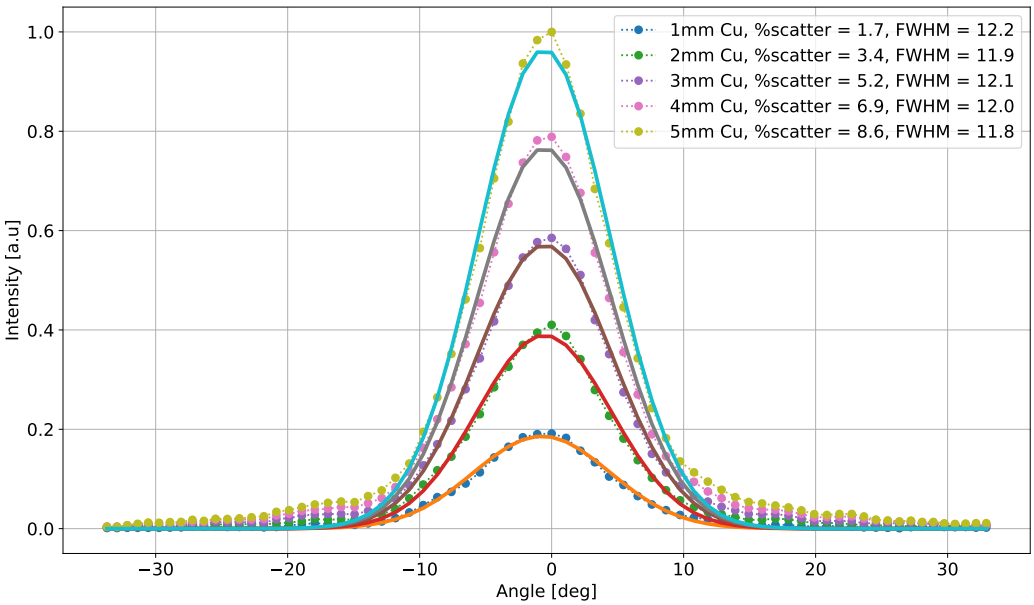

Figure 6.7: MCNP6 simulation results of 14.1 MeV neutron scattering on various thicknesses of copper. Note that this plot shows only the scattered neutrons. The plot of all events including the non-scattered neutrons would show as a large peak in the center.

by ambient temperature and air flow. Therefore, active cooling is required.

In conclusion, the improvements in the target and alpha detector will allow for a significant reduction (greater than a factor of 40) in X-rays and gamma rays incident on the YAP crystal, which would allow for improved position resolution as well as for higher rate handling capabilities. In addition to the improvements shown above, the new neutron generator will have an ion source with inner aluminum walls as opposed to stainless steel. Aluminum was shown to yield a higher monatomic D and T fraction [51], which has a direct impact on both the neutron yield and reaction kinematics as explained in the introductory chapter. The CAD drawing of this improved API neutron generator being built and tested by Adelphi Inc. [1] is shown in Figure 6.11.

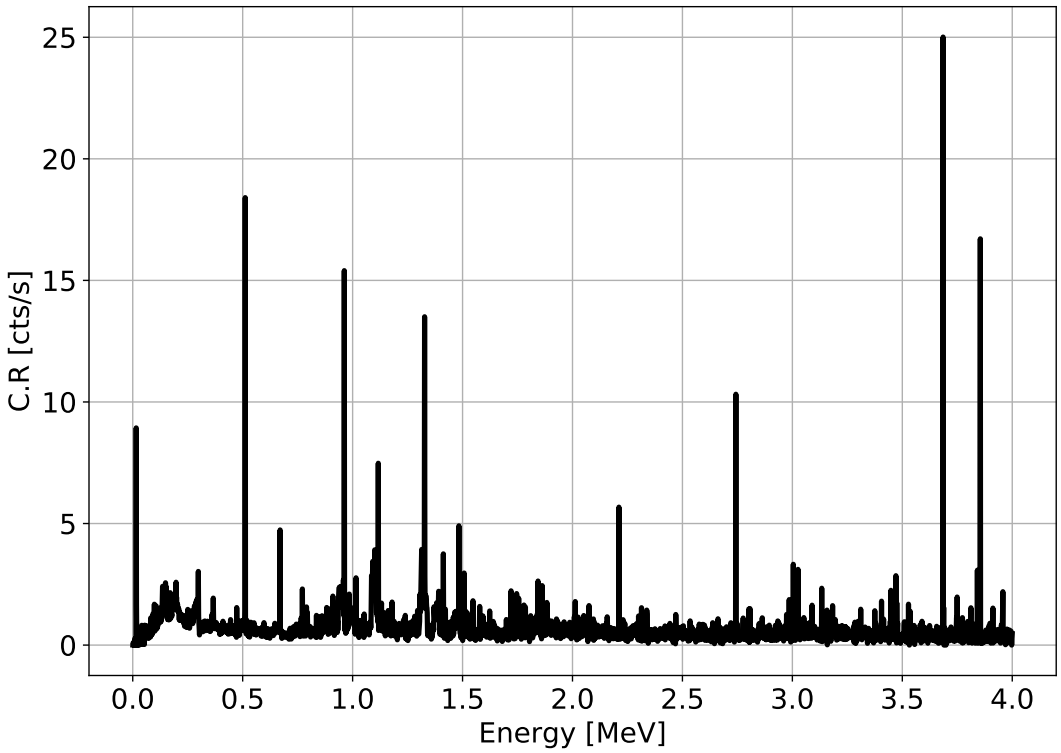

Figure 6.8: MCNP6 simulation (F6 tally) of energy deposition from gamma rays originating in the API target onto the 1 mm YAP crystal located 6 cm away. The total count rate at maximum neutron output (2×10^8 n/s) is 2000 γ/s. This is expected to be reduced by at least a factor of 40 in the new target design due to 4 times less copper and 10 times thinner YAP.

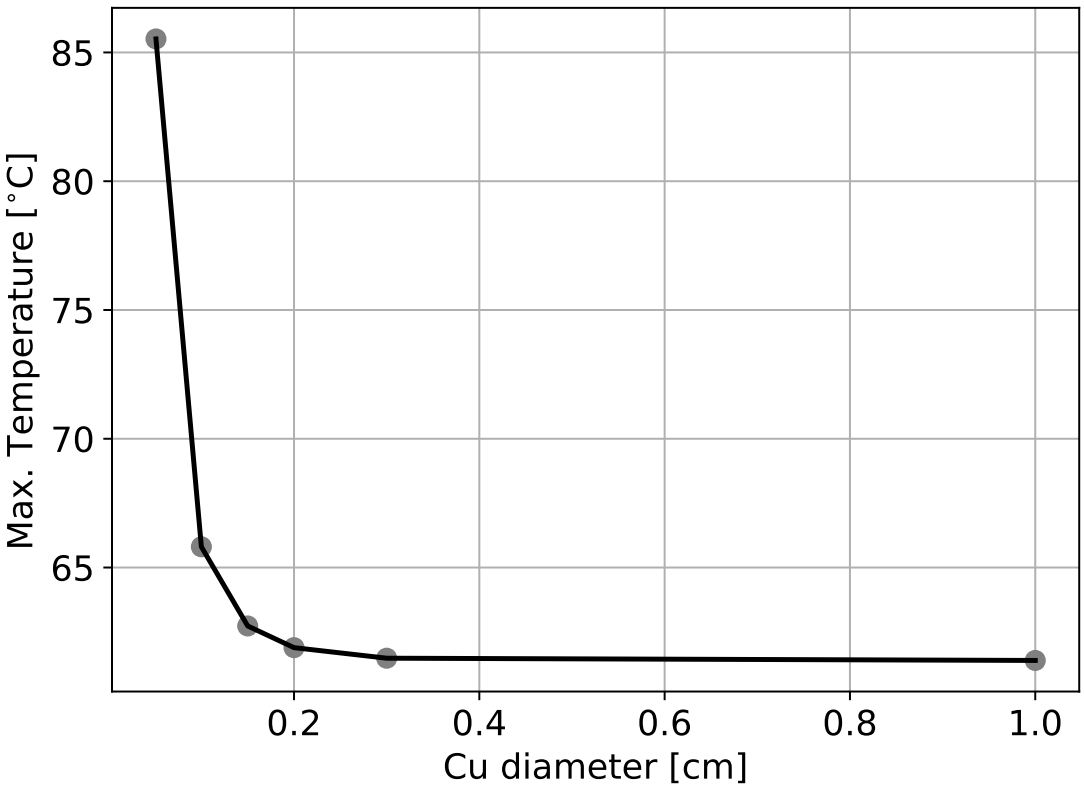

Figure 6.9: Simplified COMSOL heat transfer simulation results of a proposed API neutron target. Note that there is a minimum copper substrate diameter needed for optimum heat transfer.

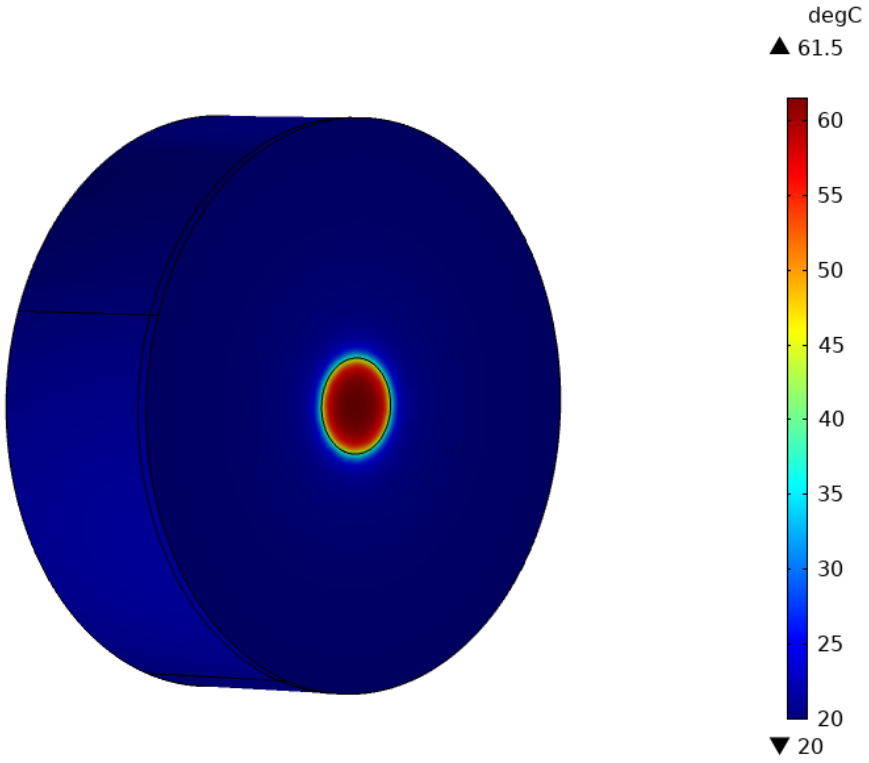

Figure 6.10: Example geometry and results for a COMSOL heat transfer simulation of a proposed API neutron target. The geometry consists of a 120 µm titanium layer bonded onto a 2 mm thick copper substrate. The beam profile on the target has a diameter of 1 mm and a power density of 40 W cm^{-2}. This example shows the maximum temperature on the surface for the case of a 3 mm diameter copper substrate.

Figure 6.11: New generation API neutron generator built and tested by Adelphi Inc. [1]. Several improvements were made to allow for a superior position resolution and the ability to handle higher alpha rates among others.

Chapter 7

Conclusions

We presented the design and performance of a high-resolution associated particle imaging system for the determination of 3D isotopic distributions in soils. Initial MCNP6 simulations and theoretical calculations showed that the system was, in principle, feasible when operating the neutron generator at 2×10^8 n/s (100 kV in our setup) and it could measure carbon down to the percent level. The alpha particle detector mounted on the neutron generator head was designed using the ray tracing (optical photon transport) package in COMSOL Multiphysics and its electronic response was modeled with LTspice and ngspice. Experimental tests were performed with the alpha detector in isolation and as part of the overall system in order to characterize certain properties including its position resolution, uniformity, and rate handling capabilities. For this purpose, we used a four-corner electronic readout board. Even though this readout board allows for a high degree of uniformity and a position resolution of 0.2 mm, we found that it is the limiting factor in terms of rate capabilities. In practice it can handle a neutron generator voltage of up to 65 kV ($\approx 1 \times 10^7$ n/s) with minimal position degradation.

The gamma detectors were also characterized and integrated with the Data Acquisition System; the PIXIE-16 from XIA. The energy and time algorithms used by the PIXIE-16 were reproduced in software and the parameters optimized. In particular, the time resolution was improved from 1.8 ns to 1.3 ns for LaBr and from 2.0 ns to 1.6 ns for NaI. Additionally, the response of gamma detectors was modeled in MCNP6 and some of the experimental data benchmarked against such simulations.

The complete system integration was described including the gamma detector shielding, timing performance, and the position reconstruction algorithm. Our tests show that the X-Y resolution is 3 ± 1 cm for both YAP-LaBr and YAP-NaI. The system depth resolution is 7 ± 1 cm for YAP-LaBr and 8 ± 1 cm for YAP-NaI. We also successfully reconstructed graphite samples in three dimensions as examples of applying the API technique. Overall, the X-Y resolution from the alpha detector performed better than the initial estimate by a factor of two. The Z-resolution, however, is currently slightly worse than the initial estimate of 5 cm due to a time resolution greater than 1 ns, but we outlined a few methods to improve it. For instance, a better time resolution can be achieved by further optimizing the parameters in the CFD algorithm used in the PIXIE-16.

Initial soil samples were irradiated and basic analysis performed to compare soils with different carbon concentrations. We also irradiated individual materials relevant to soil chemistry in order to create a library with element-specific information regarding gamma-ray response to 14.1 MeV neutrons. These elemental spectra were compared to MCNP6 simulations with an overall agreement, but with important discrepancies, some of which may be due to a lack of reliable cross-section data at this energy.

Finally, based on our initial experience developing the API system, we made important recommendations for an improved version of a neutron generator, which will be delivered by Adelphi Inc. to LBNL in 2020. This new system will be able to handle higher alpha rates and produce sharper images, hence reducing measurement times and improving the position resolution of the system.

In the future, MCNP6 models must be improved to accurately predict measurement times and isotopic concentrations. Additionally, more soil samples need to be irradiated and an analysis pipeline should be developed before field measurements can begin. The ultimate test of the device will be in the field, which is expected to happen in the spring of 2020.

In summary, we designed and built a non-destructive system to measure isotopic distributions in soil, particularly carbon. Experimental results show that the initial claims of 5 cm × 5 cm × 5 cm resolution is achievable, and there is no indication that the system cannot perform as planned. As expected, handling high alpha rates has proven to be the main challenge to be overcome. Nevertheless, operation at high rates is not necessary for a proof-of-concept of this technology. Furthermore, we identified a path forward for handling high alpha rates that include an improved neutron generator and readout electronics. Initial tests in this regard are currently being carried out at LBNL. The results presented in this thesis show that using API for carbon measurements should greatly improve on the more conventional methods currently employed.

Bibliography

[1] Adelphi Technology Inc. http://adelphitech.com/. 2018.

[2] S. Agostinelli et al. "GEANT4: A Simulation toolkit". In: *Nucl. Instrum. Meth.* A506 (2003), pp. 250–303. DOI: 10.1016/S0168-9002(03)01368-8.

[3] D.A. Brown et al. "ENDF/B-VIII.0: The 8th Major Release of the Nuclear Reaction Data Library with CIELO-project Cross Sections, New Standards and Thermal Scattering Data". In: *Nuclear Data Sheets* 148 (2018). Special Issue on Nuclear Reaction Data, pp. 1–142. ISSN: 0090-3752. DOI: https://doi.org/10.1016/j.nds.2018.02.001. URL: http://www.sciencedirect.com/science/article/pii/S0090375218300206.

[4] D.A. Brown et. al. "ENDF/B-VIII.0: The 8th Major Release of the Nuclear Reaction Data Library with CIELO-project Cross Sections, New Standards and Thermal Scattering Data". In: *Nuclear Data Sheets* 148 (2018). Special Issue on Nuclear Reaction Data, pp. 1–142. ISSN: 0090-3752. DOI: https://doi.org/10.1016/j.nds.2018.02.001. URL: http://www.sciencedirect.com/science/article/pii/S0090375218300206.

[5] Mark Bandstra and others. becquerel. 2019. URL: https://github.com/lbl-anp/becquerel.

[6] A. Barzilov and P. C. Womble. "Study of Doppler broadening of gamma-ray spectra in 14-MeV neutron activation analysis". In: *Journal of Radioanalytical and Nuclear Chemistry* 301.3 (Sept. 2014), pp. 811–819. ISSN: 1588-2780. DOI: 10.1007/s10967-014-3189-8. URL: https://doi.org/10.1007/s10967-014-3189-8.

[7] A. Beyerle et al. "Associated particle imaging". In: *Conference Record of the 1991 IEEE Nuclear Science Symposium and Medical Imaging Conference*. Nov. 1991, 1298–1304 vol.2. DOI: 10.1109/NSSMIC.1991.259135.

[8] C. Carasco et al. "In-field tests of the EURITRACK tagged neutron inspection system". In: *Nucl. Instrum. Methods Phys. Res. A* 588.3 (2008), pp. 397–405. ISSN: 0168-9002. DOI: https://doi.org/10.1016/j.nima.2008.01.097. URL: http://www.sciencedirect.com/science/article/pii/S0168900208001538.

[9] R. S. Caswell. "Fast Neutron Physics. Part 1. Techniques. J. B. Marion and J. L. Fowler, Eds. Interscience, New York, 1960. xiv + 983 pp. Illus. 29". In: *Science* 132.3427 (1960), pp. 613–614. ISSN: 0036-8075. DOI: 10.1126/science.132.3427.613. eprint: https://science.sciencemag.org/content/132/3427/613.full.pdf. URL: https://science.sciencemag.org/content/132/3427/613.

[10] J. W. Cates, J. P. Hayward, and X. Zhang. "Achievable position resolution of an alpha detector with continuous spatial response for use in associated particle imaging". In: *2013 IEEE Nuclear Science Symposium and Medical Imaging Conference (2013 NSS/MIC)*. Oct. 2013, pp. 1–3. DOI: 10.1109/NSSMIC.2013.6829782.

[11] COMSOL Multiphysics v. 5.2. https://www.comsol.com. 2018.

[12] CRYTUR, spol. s r.o. https://crytur.cz. 2018.

[13] Julius Csikai. *CRC Handbook of Fast Neutron Generators*. CRC, Boca Raton, FL, 1987.

[14] Dschwen. https://en.wikipedia.org/wiki/Constantfractiondiscriminator/. Under license CC BY-SA 2.5: https://creativecommons.org/licenses/by-sa/2.5/. 2019.

[15] C. Eleon et al. "Experimental and MCNP simulated gamma-ray spectra for the UNCOSS neutron-based explosive detector". In: *Nuclear Instruments and Methods in Physics Research Section A: Accelerators, Spectrometers, Detectors and Associated Equipment* 629.1 (2011), pp. 220–229. ISSN: 0168-9002. DOI: https://doi.org/10.1016/j.nima.2010.11.055. URL: http://www.sciencedirect.com/science/article/pii/S0168900210025180.

[16] V. Yu. Alexakhin et.al. "Detection of diamonds in kimberlite by the tagged neutron method". In: *Nuclear Instruments and Methods in Physics Research Section A: Accelerators, Spectrometers, Detectors and Associated Equipment* 785 (2015), pp. 9–13. ISSN: 0168-9002. DOI: https://doi.org/10.1016/j.nima.2015.02.049. URL: http://www.sciencedirect.com/science/article/pii/S0168900215002594.

[17] Cristiano Lino Fontana et al. "Detection System of the First Rapidly Relocatable Tagged Neutron Inspection System (RRTNIS), Developed in the Framework of the European H2020 C-BORD Project". In: *Physics Procedia* 90 (2017). Conference on the Application of Accelerators in Research and Industry, CAARI 2016, 30 October – 4 November 2016, Ft. Worth, TX, USA, pp. 279–284. ISSN: 1875-3892. DOI: https://doi.org/10.1016/j.phpro.2017.09.010. URL: http://www.sciencedirect.com/science/article/pii/S1875389217301694.

[18] T Goorley et al. "Initial MCNP6 release overview". In: *Nuclear Technology* 180.3 (2012), pp. 298–315. DOI: 10.13182/NT11-135.

[19] D Greene and R L Thomas. "The attenuation of 14 MeV neutrons in steel and polyethylene". In: *Physics in Medicine and Biology* 14.1 (Jan. 1969), pp. 45–54. DOI: 10.1088/0031-9155/14/1/003. URL: https://iopscience.iop.org/article/10.1088/0031-9155/14/1/003.

[20] Hamamatsu Photonics K.K. https://www.hamamatsu.com. 2018.

[21] Jingyi Huang et al. "The location- and scale- specific correlation between temperature and soil carbon sequestration across the globe". en. In: *Sci. Total Environ.* 615 (Feb. 2018), pp. 540–548. ISSN: 0048-9697, 1879-1026. DOI: 10.1016/j.scitotenv.2017.09.136. URL: http://dx.doi.org/10.1016/j.scitotenv.2017.09.136.

[22] Qing Ji et al. "Development of a Time-tagged Neutron Source for SNM Detection". In: *Physics Procedia* 66 (2015). The 23rd International Conference on the Application of Accelerators in Research and Industry - CAARI 2014, pp. 105–110. ISSN: 1875-3892. DOI: https://doi.org/10.1016/j.phpro.2015.05.015. URL: http://www.sciencedirect.com/science/article/pii/S1875389215001686.

[23] L. Jokhovets et al. "Improved Rise Approximation Method for Pulse Arrival Timing". In: *IEEE Transactions on Nuclear Science* 66.8 (Aug. 2019), pp. 1942–1951. ISSN: 1558-1578. DOI: 10.1109/TNS.2019.2923382.

[24] Valentin T. Jordanov and Glenn F. Knoll. "Digital synthesis of pulse shapes in real time for high resolution radiation spectroscopy". In: *Nuclear Instruments and Methods in Physics Research Section A: Accelerators, Spectrometers, Detectors and Associated Equipment* 345.2 (1994), pp. 337–345. ISSN: 0168-9002. DOI: https://doi.org/10.1016/0168-9002(94)91011-1. URL: http://www.sciencedirect.com/science/article/pii/0168900294910111.

[25] W. El Kanawati et al. "Acquisition of prompt gamma-ray spectra induced by 14MeV neutrons and comparison with Monte Carlo simulations". In: *Applied Radiation and Isotopes* 69.5 (2011), pp. 732–743. ISSN: 0969-8043. DOI: https://doi.org/10.1016/j.apradiso.2011.01.010. URL: http://www.sciencedirect.com/science/article/pii/S0969804311000121.

[26] A. Kavetskiy et al. "Continuous versus pulse neutron induced gamma spectroscopy for soil carbon analysis". In: *Applied Radiation and Isotopes* 96 (2015), pp. 139–147. ISSN: 0969-8043. DOI: https://doi.org/10.1016/j.apradiso.2014.10.024. URL: http://www.sciencedirect.com/science/article/pii/S0969804314003790.

[27] J.H. Kelley, J.E. Purcell, and C.G. Sheu. "Energy levels of light nuclei A=12". In: *Nuclear Physics A* 968 (2017), pp. 71–253. ISSN: 0375-9474. DOI: https://doi.org/10.1016/j.nuclphysa.2017.07.015. URL: http://www.sciencedirect.com/science/article/pii/S0375947417303330.

[28] Glenn F. Knoll. *Radiation Detection and Measurement*. Fourth edition. John Wiley & Sons, Inc., 2010. ISBN: 987-0-470-13148-0.

[29] John R. Lamarsh. *Introduction to Nuclear Reactor Theory*. First edition. Addison-Wesley Publishing Company, Inc., 1972.

[30] M.L. Litvak et al. "Associated particle imaging instrumentation for future planetary surface missions". In: *Nucl. Instrum. Methods Phys. Res. A* 922 (2019), pp. 19–27. ISSN: 0168-9002. DOI: https://doi.org/10.1016/j.nima.2018.11.050. URL: http://www.sciencedirect.com/science/article/pii/S0168900218316255.

[31] LTspice from Analog Devices. https://www.analog.com/LTspice. 2018.

[32] M. Moszyński et al. "Properties of the YAP : Ce scintillator". In: *Nuclear Instruments and Methods in Physics Research Section A: Accelerators, Spectrometers, Detectors and Associated Equipment* 404.1 (1998), pp. 157–165. ISSN: 0168-9002. DOI: https://doi.org/10.1016/S0168-9002(97)01115-7. URL: http://www.sciencedirect.com/science/article/pii/S0168900297011157.

[33] MPF Products. https://mpfpi.com/. 2017.

[34] R. J. Murphy, B. Kozlovsky, and G. H. Share. "Nuclear cross sections for gamma ray deexcitation line production by secondary neutrons in the Earth's atmosphere". In: *Journal of Geophysical Research: Space Physics* 116.A3 (2011). DOI: 10.1029/2010JA015820. eprint: https://agupubs.onlinelibrary.wiley.com/doi/pdf/10.1029/2010JA015820. URL: https://agupubs.onlinelibrary.wiley.com/doi/abs/10.1029/2010JA015820.

[35] R. O. Nelson et al. "High-Resolution Measurements and Calculations of Photon-Production Cross Sections for ^{16}O(n,xγ) Reactions Induced by Neutrons with Energies between 4 and 200 MeV". In: *Nuclear Science and Engineering* 138 (2001), p. 105. DOI: 10.13182/NSE01-A2205. URL: http://dx.doi.org/10.13182/NSE01-A2205.

[36] P. L. Okhuysen et al. "Detection of Fast Neutrons by the Associated Particle Method". In: *Review of Scientific Instruments* 29.11 (1958), pp. 982–985. DOI: 10.1063/1.1716073. eprint: https://doi.org/10.1063/1.1716073. URL: https://doi.org/10.1063/1.1716073.

[37] P. D. Olcott et al. "Compact readout electronics for position sensitive photomultiplier tubes". In: *2003 IEEE Nuclear Science Symposium. Conference Record (IEEE Cat. No.03CH37515)*. Vol. 3. Oct. 2003, 1962–1966 Vol.3. DOI: 10.1109/NSSMIC.2003.1352264.

[38] Open source spice simulator. http://ngspice.sourceforge.net. 2019.

[39] Pico Technology. https://www.picotech.com/. 2019.

[40] Vladimir Popov, Stan Majewski, and Benjamin L. Welch. "A novel readout concept for multianode photomultiplier tubes with pad matrix anode layout". In: *Nuclear Instruments and Methods in Physics Research Section A: Accelerators, Spectrometers, Detectors and Associated Equipment* 567.1 (2006). Proceedings of the 4th International Conference on New Developments in Photodetection, pp. 319–322. ISSN: 0168-9002. DOI: https://doi.org/10.1016/j.nima.2006.05.114. URL: http://www.sciencedirect.com/science/article/pii/S0168900206009478.

[41] P. Ramachandran and G. Varoquaux. "Mayavi: 3D Visualization of Scientific Data". In: *Computing in Science & Engineering* 13.2 (2011), pp. 40–51. ISSN: 1521-9615.

[42] Refractive Index Database. https://refractiveindex.info. 2019.

[43] Jonathan Sanderman, Tomislav Hengl, and Gregory J Fiske. "Soil carbon debt of 12,000 years of human land use". en. In: *Proc. Natl. Acad. Sci. U. S. A.* 114.36 (Sept. 2017), pp. 9575–9580. ISSN: 0027-8424, 1091-6490. DOI: 10.1073/pnas.1706103114. URL: http://dx.doi.org/10.1073/pnas.1706103114.

[44] Keiichi SHIBATA et al. "JENDL-4.0: A New Library for Nuclear Science and Engineering". In: *Journal of Nuclear Science and Technology* 48.1 (2011), pp. 1–30. DOI: 10.1080/18811248.2011.9711675. eprint: https://doi.org/10.1080/18811248.2011.9711675. URL: https://doi.org/10.1080/18811248.2011.9711675.

[45] S. Siegel et al. "Simple charge division readouts for imaging scintillator arrays using a multi-channel PMT". In: *IEEE Transactions on Nuclear Science* 43.3 (June 1996), pp. 1634–1641. ISSN: 0018-9499. DOI: 10.1109/23.507162.

[46] Stephen Derenzo and others. http://scintillator.lbl.gov. 2019.

[47] H. Tan et al. "High rate pulse processing algorithms for microcalorimeters". In: *2008 IEEE Nuclear Science Symposium Conference Record*. Oct. 2008, pp. 1130–1133. DOI: 10.1109/NSSMIC.2008.4774600.

[48] Tdudziak. https://en.wikipedia.org/wiki/Constantfractiondiscriminator/. Under license CC BY-SA 4.0: https://creativecommons.org/licenses/by-sa/4.0/. 2019.

[49] Mauricio Ayllon Unzueta et al. "An associated particle imaging system for soil-carbon measurements". In: *Hard X-Ray, Gamma-Ray, and Neutron Detector Physics XXI*. Ed. by Ralph B. James, Arnold Burger, and Stephen A. Payne. Vol. 11114. International Society for Optics and Photonics. SPIE, 2019, pp. 197–202. DOI: 10.1117/12.2530704. URL: https://doi.org/10.1117/12.2530704.

[50] Mauricio Ayllon Unzueta et al. "Position sensitive alpha detector for an associated particle imaging system". In: *AIP Conference Proceedings* 2160.1 (2019), p. 050005. DOI: 10.1063/1.5127697. eprint: https://aip.scitation.org/doi/pdf/10.1063/1.5127697. URL: https://aip.scitation.org/doi/abs/10.1063/1.5127697.

[51] J. H. Vainionpaa et al. "Experiments with planar inductive ion source meant for creation of H+ beams". In: *Review of Scientific Instruments* 78.6 (2007), p. 063503. DOI: 10.1063/1.2742624. eprint: https://doi.org/10.1063/1.2742624. URL: https://doi.org/10.1063/1.2742624.

[52] Vladivoj Valkovic. *14 MeV Neutrons: Physics and Applications*. First edition. CRC Press, 2016. ISBN: 978-1-4822-3801-3.

[53] Daniel-Stefan Veres. *A comparative study between loss on ignition and total carbon analysis on Late Glacial sediments from Atteköps mosse, southwestern Sweden, and their tentative correlation with the GRIP event stratigraphy*. eng. Student Paper. 2001.

[54] Zhonghai Wang et al. "Design, development and evaluation of a resistor-based multiplexing circuit for a 20 by 20 SiPM array". In: *Nuclear Instruments and Methods in Physics Research Section A: Accelerators, Spectrometers, Detectors and Associated Equipment* 816 (2016), pp. 40–46. ISSN: 0168-9002. DOI: https://doi.org/10.1016/j.nima.2016.01.081. URL: http://www.sciencedirect.com/science/article/pii/S0168900216001224.

[55] L. Wielopolski, S. Mitra, and O. Doron. "Non-carbon-based compact shadow shielding for 14 MeV neutrons". In: *Journal of Radioanalytical and Nuclear Chemistry* 276.1 (Apr. 2008), pp. 179–182. ISSN: 1588-2780. DOI: 10.1007/s10967-007-0429-1. URL: https://doi.org/10.1007/s10967-007-0429-1.

[56] L. Wielopolski et al. "Soil carbon measurements using inelastic neutron scattering". In: *IEEE Transactions on Nuclear Science* 47.3 (June 2000), pp. 914–917. ISSN: 1558-1578. DOI: 10.1109/23.856717.

[57] XIA LLC. https://xia.com. 2018.

[58] Galina Yakubova et al. "Application of Geant4 simulation for analysis of soil carbon inelastic neutron scattering measurements". In: *Applied Radiation and Isotopes* 113 (2016), pp. 33–39. ISSN: 0969-8043. DOI: https://doi.org/10.1016/j.apradiso.2016.04.013. URL: http://www.sciencedirect.com/science/article/pii/S0969804316301440.

[59] Galina Yakubova et al. "Applying Monte-Carlo simulations to optimize an inelastic neutron scattering system for soil carbon analysis". In: *Applied Radiation and Isotopes* 128 (2017), pp. 237–248. ISSN: 0969-8043. DOI: https://doi.org/10.1016/j.apradiso.2017.07.003. URL: http://www.sciencedirect.com/science/article/pii/S096980431631065X.

[60] Yan Yan et al. "Study on the method with associated particle for measuring the neutron yield of D–D neutron generator†". In: *Nuclear Instruments and Methods in Physics Research Section A: Accelerators, Spectrometers, Detectors and Associated Equipment* 773 (2015), pp. 52–55. ISSN: 0168-9002. DOI: https://doi.org/10.1016/j.nima.2014.11.023. URL: http://www.sciencedirect.com/science/article/pii/S0168900214012935.

[61] ZEMAX simulation. https://www.zemax.com. 2019.

[62] V.V. Zerkin and B. Pritychenko. "The experimental nuclear reaction data (EXFOR): Extended computer database and Web retrieval system". In: *Nuclear Instruments and Methods in Physics Research Section A: Accelerators, Spectrometers, Detectors and Associated Equipment* 888 (2018), pp. 31–43. ISSN: 0168-9002. DOI: https://doi.org/10.1016/j.nima.2018.01.045. URL: http://www.sciencedirect.com/science/article/pii/S0168900218300627.

[63] Xiaodong Zhang et al. "Benchmarking the Geant4 full system simulation of an associated alpha-particle detector for use in a D–T neutron generator". In: *Applied Radiation and Isotopes* 70.8 (2012), pp. 1485–1493. ISSN: 0969-8043. DOI: https://doi.org/10.1016/j.apradiso.2012.04.026. URL: http://www.sciencedirect.com/science/article/pii/S0969804312003041.

[64] J. F. Ziegler, M. D. Ziegler, and J. P. Biersack. "SRIM - The stopping and range of ions in matter (2010)". In: *Nuclear Instruments and Methods in Physics Research B* 268 (June 2010), pp. 1818–1823. DOI: 10.1016/j.nimb.2010.02.091.